

Electrocatalytic Nanoeffect at Gold Nanoparticles

A thesis submitted for the degree of Doctor of Philosophy
in Physical and Theoretical Chemistry

Ying Wang
St. Edmund Hall

August 2014

Abstract

Nanoelectrochemistry explores the differences in chemical behaviour at the nanoscale as compared to the macro-scale. This thesis is concerned with nanoelectrochemistry and aims to develop and apply novel experiments for the unambiguous identification of changed electrode kinetics at the nanoscale. This is challenging since electrochemical responses are controlled by diverse factors like enhanced mass transport and adsorption as well as electron transfer kinetics. A joint computational and experimental strategy is employed.

Chapter 1, 2 and 3 cover essential introductory material and basic experimental details relevant to all experiment. Fuller descriptions and details are given in the following chapters as and when needed.

Chapter 4 reports the development of an electrochemical characterization method, to achieve a fast and simple quantification of the average particle size and the number of nanoparticles deposited on a glassy carbon electrode. The method consists of surface area characterization by underpotential deposition of lead particles and the determination of the amount of gold from anodic stripping in HCl. This method is

also proven to be effective by comparing the results with SEM measurements.

Next, in chapter 5, a generic strategy combining computation and experimental approach is developed in order to study the electron transfer kinetics of gold nanoparticles. The modelling part considers the kinetics of the electrochemical process on the bulk materials for different regions in the electrode, that is, the substrate (glassy carbon) and the nanoparticles (gold). Comparison of experimental and theoretical results enables the detection of changes in the electrode kinetics at the nanoscale. This approach is applied into the electro-oxidations of nitrite and L-ascorbic acid for gold nanoparticles from 20 - 90 nm. In the former, analysing the system shows that no change in electron transfer kinetics is involved in the process, even though a decrease of the over-potential and an increase in the peak current are observed. But these changes reflect mass transport effects, not electrocatalysis. A case where an authentic enhanced electron transfer kinetic change occurs is shown for the ascorbic acid system.

Finally, in chapter 6 , the above strategy is exploited further to apply a quantitative study of electron transfer kinetics for various sizes of gold nanoparticles in the oxygen reduction reaction system in sulphuric acid at 298 K. The latter is at the heart of energy transformation techniques (fuel cells, battery and so on). Compared with the electron transfer kinetics on macro gold electrodes, there is no change at gold nanoparticles from size 5 nm to 40 nm. However, in the presence of Pb(II), a strong enhancement of electron transfer kinetics is observed on 5 nm citrate capped gold nanoparticles for ORR. On the other hand, a significant decrease of electron

transfer kinetics has been found for gold nanoparticles of size 2 nm for ORR. The latter observation of strong negative electrocatalysis is also observed for the hydrogen evolution reaction (HER). This represents the first report of such effects with the HER system.

Overall the thesis has established a rigurous, theoretical basis for evaluating electrocatalysis in nanoparticulate system.

Acknowledgements

First and foremost, I would like to thank my supervisor Prof. Richard G. Compton for him giving me this opportunity to step into this incredible field of electrochemistry with such an attractive project. This thesis would not have been possible without his help and guidance.

Secondly, special thanks to Dr. Eduardo Laborda who made huge contribution though out my whole D.Phil in Oxford. Thank you Eduardo for your generous help in the projects as well as being a best friend here. I would not forget those times when we had to survive on biscuits in order to solve out those gold nanoparticle problems. His character and working attitude has deeply influenced me. I would also like to thank my colleagues for their help and collaboration, Dr. Kristina Tschulik, Dr. Blake Plowman and Dr. Kristopher Ward. And of course, my dear "first year" mates, Eddy, Emma, Min and Lin. Thank you all for going through these three years with me and all the fun "first year" events we had. Elsewhere, thank you for everyone in Compton group for providing such a sociable and professional environment in the past three years. And the name that I certainly could not miss, Prof. Xiaobo Ji. Thank him for his recommendation to this wonderful group.

Last but not the least, I would like to thank my parents and Guangzhi for their love and support through out my D.Phil. Thanks to my dad for providing useful academic suggestions for my work.

These three years in Oxford has been a great journey both professionally and personally in my life. Thank you to all the amazing people in this lovely university.

Glossary and Abbreviations

Glossary

Character	Term	Unit
a_i	Activity of species i	$mol \cdot cm^{-3}$
A	Surface area of electrode	cm^2
c_i	Concentration of species i	$mol \cdot cm^{-3}$
c_i^*	Bulk concentration of species i	$mol \cdot cm^{-3}$
D	Diffusion coefficient	$cm^2 \cdot s^{-1}$
E	Electrode potential	V
E^0	Electrode potential under standard conditions	V
E_f^0	Formal potential	V
F	The faraday constant = 96485.3	$C \cdot mol^{-1}$
G	Gibbs free energy	$J \cdot mol^{-1}$
i (I)	Current	A
j	Flux	$mol \cdot cm^{-2} \cdot s^{-1}$
k	Rate constant	
k^0	Standard heterogeneous rate constant	$cm \cdot s^{-1}$
n	Number of electron transferred	
r	radius	cm
R	Universal gas constant = 8.31447	$J \cdot K^{-1} \cdot mol^{-1}$
R_S	Solution resistance	Ω
z	Charge on electroactive species	
α	Butler-Volmer transfer coefficient for reduction	
ν	Scan rate	$V \cdot s^{-1}$
Λ	the Matsuda and Ayabe parameter	
ϕ	Electrostatic potential	V
τ	dimensionless time	
Θ	Surface coverage	

Abbreviations

Abbreviation	Meaning
Au-NPs	Gold nanopartciles
C.E	Counter electrode
EDL	Electrical double layer
EPPG	Edge plane pyrolytic graphite
GCE	Glassy carbon electrode
HER	Hydrogen evolution reaction
IHP	Inner helmholtz plane
OHP	Outer helmholtz plane
ORR	Oxygen reduction reaction
R.E	Reference electrode
SWV	Square wave voltammetry
SEM	Scanning electron microscope
SCE	Saturated calomel electrode
TEM	Transmitting electron microscope
UPD	Underpotential deposition
W.E	Working electrode
XPS	X-ray photoelectron spectroscopy

Contents

1 Fundamentals of Electrochemistry **1**

1.1 The Electrochemical Cell 1

1.1.1 Experimental Set-up 1

1.1.2 Supporting Electrolyte 6

1.2 The Electrode-Solution Interface 8

1.2.1 Faradaic and Non-Faradaic Currents 8

1.2.2 Electrical Double Layer 9

1.3 Mass Transport 12

1.3.1 Diffusion 12

1.4 Butler-Volmer Electrode Kinetics 16

1.5 Electrochemical Techniques 19

1.5.1 Cyclic Voltammetry at Macroelectrode 19

1.5.2 Cyclic Voltammetry at Microelectrodes 23

1.5.3 Square Wave Voltammetry 25

1.5.4 Chronoamperometry 26

Bibliography 28

2 Electrochemistry at the Nanoscale - Simulation **32**

2.1 Numerical Simulation Strategy: The Diffusion Domain Approximation 35

Bibliography 39

3 Experimental Methods **42**

3.1 Chemical Reagents 43

3.2 Electrochemistry Experiments 44

3.3 Synthesis and Modification of Au-NPs/GCE 44

3.4 Characterization Methods 45

3.4.1 UV-Vis Spectroscopy 45

3.4.2 Transmission Electron Microscopy (TEM) 46

3.4.3 Scanning Electron Microscope (SEM) 47

3.4.4 Electrochemistry Characterization 47

3.4.5 X-ray Photoelectron Spectroscopy (XPS) 48

Bibliography 48

4 Electrochemical Characterization of Gold Nanoparticle Modified Glassy Carbon Electrodes **51**

4.1 The Surface Oxidation of Gold Nanoparticle Supported on a Glassy Carbon Electrode in Sulphuric Acid Medium: Contrasts With the Behaviour of 'Macro' Gold 52

4.1.1 Introduction 52

4.1.2 Results and Discussion 54

4.1.3 Conclusions 60

4.2 Facile in Situ Characterization of Gold Nanoparticle on Electrode Surfaces by Electrochemical Techniques: Average Size, Number Density and Morphology Determination 61
4.2.1 Introduction 61
4.2.2 Experimental 62
4.2.3 Results and Discussion 65
4.2.4 Conclusions 71
Bibliography 72

5 A Joint Experimental and Computational Search for Authentic Nano-electrocatalytic Effects: Electrooxidation of Nitrite and L-Ascorbate on Gold Nanoparticle-Modified Glassy Carbon Electrodes 78

5.1 Electrochemical Oxidation of Nitrite: Kinetic, Mechanistic and Analytical Study by Square Wave Voltammetry 81
5.1.1 Introduction 81
5.1.2 Experimental 83
5.1.3 Results and Discussion 85
5.1.4 Conclusions 96
5.2 Electro-oxidation of Nitrite and Ascorbic Acid on Gold Nanoparticles: a Joint Approach Using Computation and Experiment. 97
5.2.1 Introduction 97
5.2.2 Theory 101

5.2.3 Experimental 104
5.2.4 Electrochemical Characterization 105
5.2.5 Results and Discussion 106
5.2.6 Conclusions 119
Bibliography 120

6 Oxygen Reduction Reaction in Strong Acid Media on Different Sizes of Gold Nanoparticle 127

6.1 A Kinetic Study of the Oxygen Reduction Reaction at, and Characterization of Electrodeposited Gold Nanoparticles of Diameter Between 17 nm and 40 nm in 0.5 M Sulphuric Acid 130
6.1.1 Introduction 130
6.1.2 Experimental 134
6.1.3 Results and Discussion 135
6.1.4 Conclusions 153
6.2 The Strong Catalytic Effect of Pb(II) on the Oxygen Reduction Reaction on 5 nm Gold Nanoparticles 154
6.2.1 Introduction 154
6.2.2 Experimental 155
6.2.3 Results and Discussion 160
6.2.4 Conclusions 173

6.3 Strong Negative Nanocatalysis: Oxygen Reduction and Hydrogen Evolution at Very Small (2 nm) Gold Nanoparticles 174
6.3.1 Introduction 174
6.3.2 Experimental Section 177
6.3.3 Results and Discussion 177
6.3.4 Conclusions 189
Bibliography 190

Chapter 1

Fundamentals of Electrochemistry

This chapter gives an overview of the fundamental aspects of the electrochemical science as well as of the electrochemical techniques and theories employed in this thesis. Topics covered in this chapter include the description and modelling of the electrochemical cell, the electrode-solution interface, mass transport phenomena, electrode kinetics and voltammetric techniques.

1.1 The Electrochemical Cell

1.1.1 Experimental Set-up

Electrochemistry is the branch of chemistry that is concerned with charge transfer processes and the associated chemical transformations, taking place at the interface between an electronic conductor (an electrode) and an ionic conductor (an electrolyte solution) [1–3]. Thus, such systems enable us to produce electrical energy from spontaneous redox reactions (galvanic cells) or to make use of electricity to produce chemical changes in a controlled way (electrolytic cells). The latter case will be

developed further. It is the basis of modern electrochemical and electroanalytical techniques to gain physico-chemical information about the stability, reactivity and mass transport of chemical species.

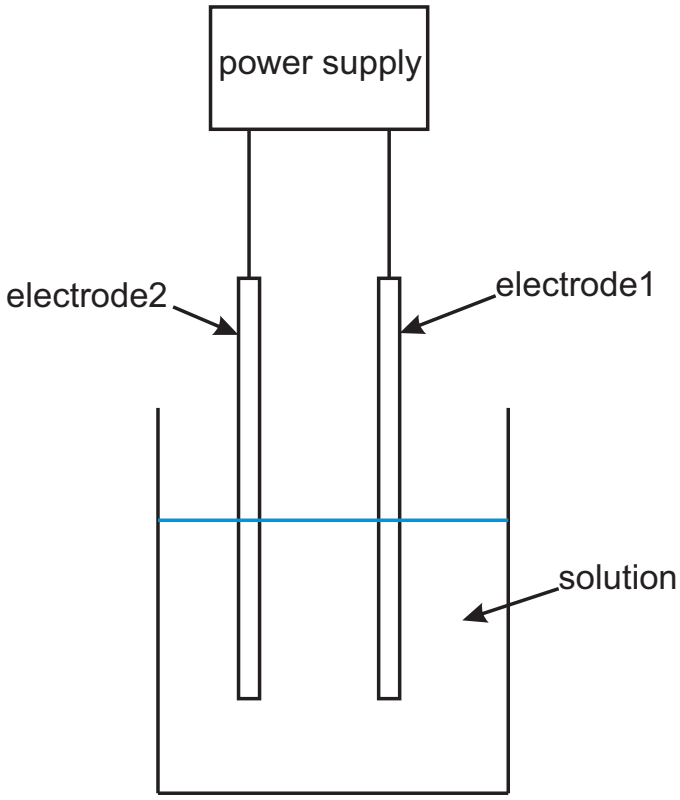


Figure 1.1: Schematic diagram of a two-electrode electrochemical set-up.

In order to perform electrochemical measurements with an electrolytic cell (that is, to apply an electrical perturbation) at least four elements are required as shown in Figure 1.1: the solution that contains the species under study as well as an electrolyte in high concentration to increase the solution conductivity; two electrodes immersed in the electrolytic solution; and a power supply that, in the most widely-used techniques, applies a potential difference between the electrodes and records the current response The potential difference between the two electrodes is given by

Eq. 1.1:

$$E_1 - E_2 = (\phi_M - \phi_S)_1 - (\phi_M - \phi_S)_2 = E_{app} - iR_S \tag{1.1}$$

where E_{app} is the potential difference applied by the power supply, ϕ_M the potential on metal electrode surface, ϕ_S the potential in the solution phase, i the current flow, R_S is the solution resistance, subscript 1 refers to the electrode 1 and subscript 2 to the electrode 2.

In order to monitor accurately the applied potential difference, it is necessary that the potential of one of the electrodes is known and that the iR_S term is minimized. The latter is known as the "ohmic drop" and it results from the solution resistance such that it increases with the distance between the two electrodes. Therefore, it is crucial to place the two electrodes as close as possible to reduce the ohmic drop. Added electrolyte (as discussed further in section 1.1.2) is also helpful since it decreases the solution resistivity [2].

As discussed previously, it is necessary that one of the electrodes (the reference electrode) provides a potential that is stable with time and temperature, E_1. Thus, the potential of the second electrode (the working electrode) can be mentioned in terms of the applied potential difference. The reference electrode is composed of an ideal nonpolarizable interface such that the electrode potential does not change with the current passing through it. The saturated calomel electrode (SCE) is employed in this thesis for this purpose. The electrochemical equilibrium that is established

in an SCE:

$$\frac{1}{2}\mathrm{Hg_2Cl_2}(s) + \mathrm{e^-} \rightleftarrows \mathrm{Hg}(l) + \mathrm{Cl^-}(aq) \tag{1.2}$$

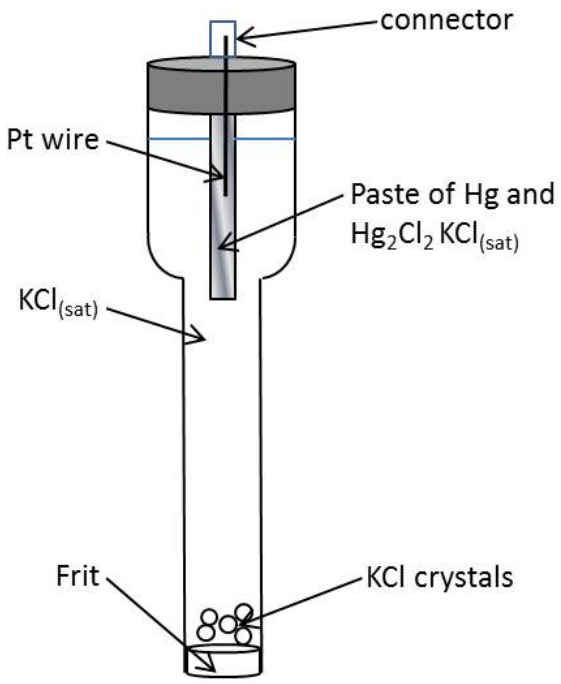


Figure 1.2: Schematic diagram of composition of saturated calomel electrode (SCE).

A schematic diagram of the SCE is shown in Figure 1.2. As can be seen, the SCE is filled with a saturated KCl solution with a porous frit as a salt bridge at the bottom to link the electrode with the solution where the other electrodes are immersed in. The potential of SCE is directly related to the activity of the chloride ion in the electrode solution as displayed in Eq.1.3. Hence, in order to maintain the stability of the SCE, it is essential to keep constant the concentration of chloride. Accordingly, the SCE employed in this thesis are all kept in saturated potassium chloride solution with excess of potassium chloride ions crystals at the bottom as

shown in Figure 1.2.

$$E = E^0_{Hg_2Cl_2/Hg/Cl^-/Hg} - \frac{RT}{F} ln(a_{Cl^-}) \tag{1.3}$$

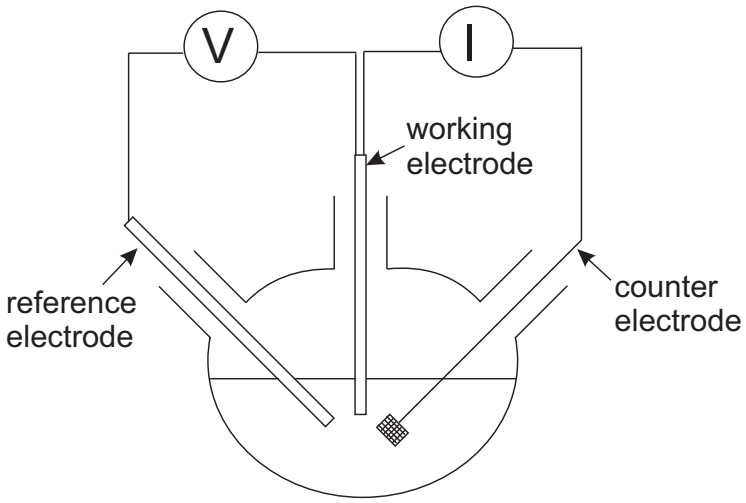


Figure 1.3: A typical three-electrode electrochemical set-up.

Unfortunately when a large current flows through the two-electrode circuit depicted in Figure 1.1, the ohmic drop term is very large and the ideal nonpolarizability and the essentially constant composition of the reference electrode are compromised. In response to these problems, the three-electrode set up was introduced into electrochemical studies aiming at an application with a higher current limit. Figure 1.3 shows a typical three-electrode system. As shown, the current is only allowed to pass between the working electrode, where the target reaction occurs, and the counter electrode, which completes the electrical circuit. There are some key requirements for a counter electrode. First, it needs to be very conductive and with a larger surface area compared to the working electrode such that the former does

not limit the current flow. Second, it is important that the counter electrode is inert in the electrolyte solution such that the substances produced on its surface do not interfere with the target species [2].

1.1.2 Supporting Electrolyte

Electrochemical measurements are usually performed in a solution containing the chemical species of interest together with a large excess of an inert supporting electrolyte, for instance, potassium chloride in water solutions and tetra-n-butylammonium perchlorate in acetonitrile solutions. The electrolyte ions are the charge carriers in the working solution such that the movement of anions and cations is responsible for the charge transport. Note that one of the most crucial criteria when choosing the supporting electrolyte is that it *should* not have reactions with the analyte or the electrode surface.

The most important purpose of adding the excess of supporting electrolyte is to maintain a homogeneous electric potential in the solution such that electro-migration of the target species is avoided [4]. As an example, Figure 1.4 shows the negative charge excess (black charges) generated upon the electro-reduction of a neutral electroactive species at the working electrode and the corresponding positive charge excess that arises around the counter electrode where a neutral species is electro-oxidised. As a result, an electric potential gradient appears that leads to the electro-migration of the generated species away from the electrode surfaces under the influence of the electric field (as shown in Figure 1.4.a). This significantly com-

plicates the modelling of the electrochemical system. When a large concentration of supporting electrolyte is added (red charges) as displayed in Figure 1.4.b, this balances any charge excess and keeps a near-zero electric field [3]. Hence, the transport of electroactive species by migration is minimised. Transport to the electrode occurs via diffusion.

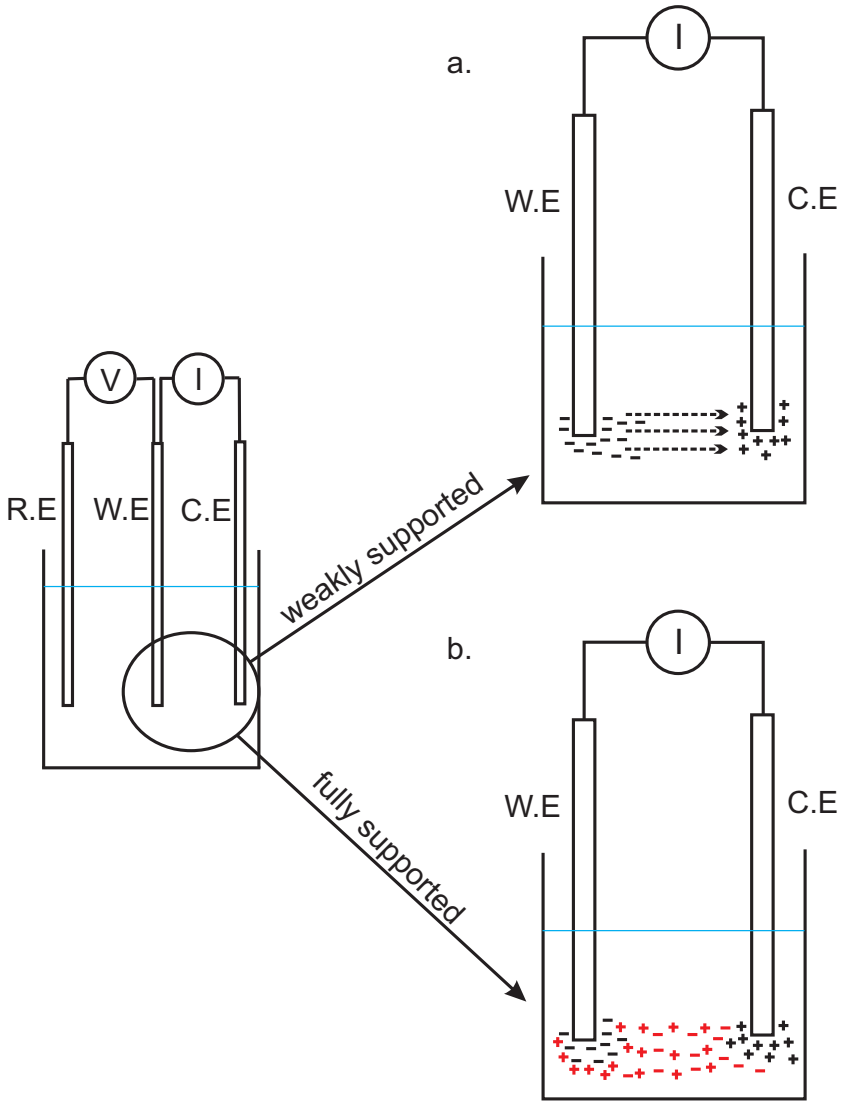


Figure 1.4: Suppression of the electromigration of the charged electrogenerated species (black charges) at the electrode surfaces upon the addition of supporting electrolyte (red charges) in the electrolytic solution: a. weakly supported system; b. fully supported system

The addition of the supporting electrolyte has further benefits for electrochemical studies. The high concentration of charge carriers increases the solution conductivity and hence reduces the ohmic drop effects. The charged species of the supporting electrolyte can individually move near the electrode surface to cancel any electric field generated in the electrical double layer (section 1.2.2) [5]. Thus, the electrical double layer thickness is kept very small compared to the diffusion layer such that its influence can be neglected for conventional electrode sizes [3, 5]. Finally, the excess of supporting electrolyte provides a controlled and uniform ionic strength throughout the solution [2].

1.2 The Electrode-Solution Interface

1.2.1 Faradaic and Non-Faradaic Currents

There are two different types of current that may flow at the working electrode during an electrochemical experiment, depending on whether electrons are transferred across the electrode—solution interface (Faradaic currents) or not (non-Faradaic currents).

When Faradaic processes take place, electrons are transferred across the interface upon the electro-oxidation or electro-reduction of the electroactive species. This kind of processes follows Faraday's law, that is, the amount of chemical reaction caused by the flow of current is proportional to the amount of electricity passed.

Non-Faradaic processes are due to the existence of the electrical double layer

(detailed in section 1.2.2). When a potential applied on a electrode, there will be a excess of charges accumulated on the electrode surface (q^M) and the solution phase near the electrode (q^S), where q^M = - q^S [2]. Thus, experimentally, the electrode-solution interface behaves like a capacitor in the system [2]. Thus, any change of potential will lead to a current flow which is due to the redistribution of dipoles and/or ion movement between the solution phase and the electrode. This capacitive current is known as a non-Faradaic current or charging current and it is not governed by Farady's law.

1.2.2 Electrical Double Layer

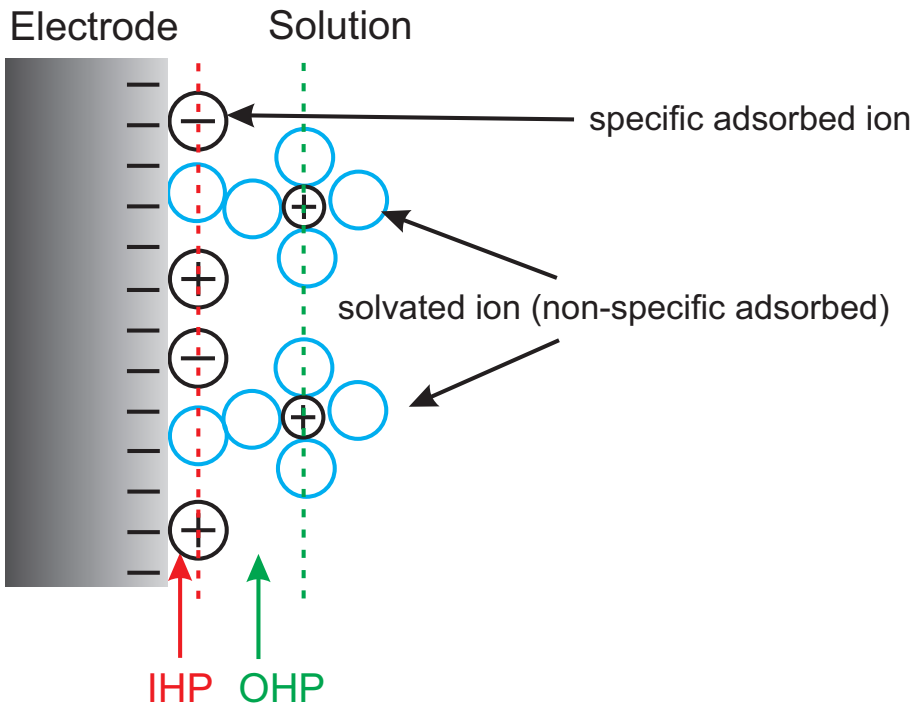


Figure 1.5: Structure of the electrical double layer. Blue circles represent the solvent molecules. IHP and OHP are the Inner Helmholtz Plane and Outer Helmholtz Plane, respectively.

The electrical double layer (EDL) refers to the parallel charge layers that develop at the electrode-solution interface such that, at equilibrium, the charge excess at the polarized electrode surface is balanced by a charge excess of opposite sign in the adjacent solution region. Figure 1.5 illustrates the EDL structure at the interface of a negatively-charged electrode. Some ions are specifically adsorbed on the electrode surface as well as solvent molecules [2, 6]. This is normally arisen from chemical interaction between the adsorbate and the electrode [1]. Such ions are typically desolvated but the bonding is much stronger than solvated ions [2, 6]. The distance from the center of the specifically adsorbed ions to the electrode surface is called the inner Helmholtz plane (IHP) [2, 6]. In an outer diffuse region, solvated cations will be predominant and the position of the centers of the nearest solvated ions defines the outer Helmholtz Plane (OHP).

Helmholtz [7] proposed the first double layer model. In this model (shown in Figure 1.6.a), the double layer is described as two layers of opposite charges formed at the each side of the electrode-solution interface. The variation of the electrostatic potential, ϕ, drops linearly from ϕ_M to ϕ_S within the double layer thickness. However, from a practical perspective, the Helmholtz model neglects two crucial factors: the dependence on the supporting electrolyte concentration and the structure of the interface in the solution side beyond the first layer next to the electrode surface.

Later, Gouy [8] and Chapman [9] suggested a new model for the double layer structure (Figure 1.6.b) taking into account a continuous distribution of electrolyte ions in the electrolyte solution (the diffuse layer), which are simultaneously subject

to random thermal motion and electrostatic interaction with the electrode surface charge [10].

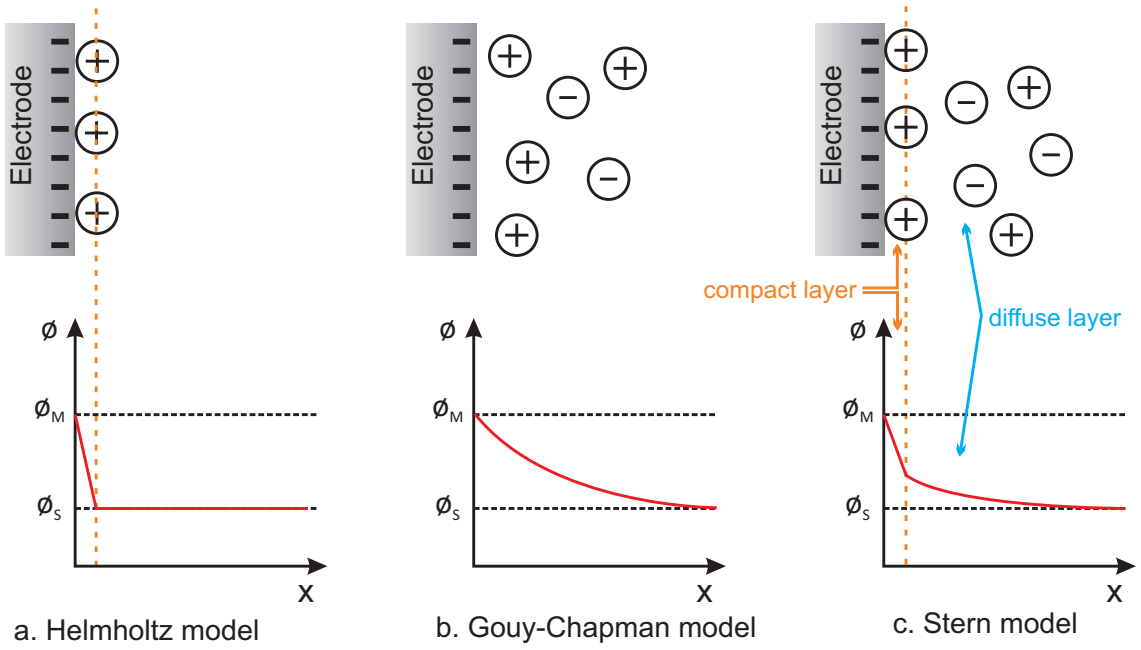


Figure 1.6: The Helmholtz (a), Gouy-Chapman (b) and Stern (c) models of the electrical double layer. ϕ is the electrostatic potential, "M" and "S" refers to the metal electrode and the electrolytic solution, respectively, and x is the distance from the electrode surface.

On the basis of the Helmholtz and Gouy and Chapman models, Stern [11] developed a double layer structure model with both a compact layer and a diffuse layer where the former includes solvent molecules and strongly adsorbed ions. The boundary between the compact and diffuse layer corresponds to the OHP [2, 6]. The decay of the electrostatic potential predicted by this model is shown schematically in Figure 1.6.c.

1.3 Mass Transport

Given that the charge transfer in electrochemical measurements is a heterogeneous process, the composition of the solution near the electrode surface will be different from that in the bulk solution. As a consequence, mass transfer will occur spontaneously in order to homogenise the solution and to re-establish equilibrium conditions [2, 3, 12]. Diffusion, convection and migration are the three major modes of mass transport and they will be detailed in the following sections.

1.3.1 Diffusion

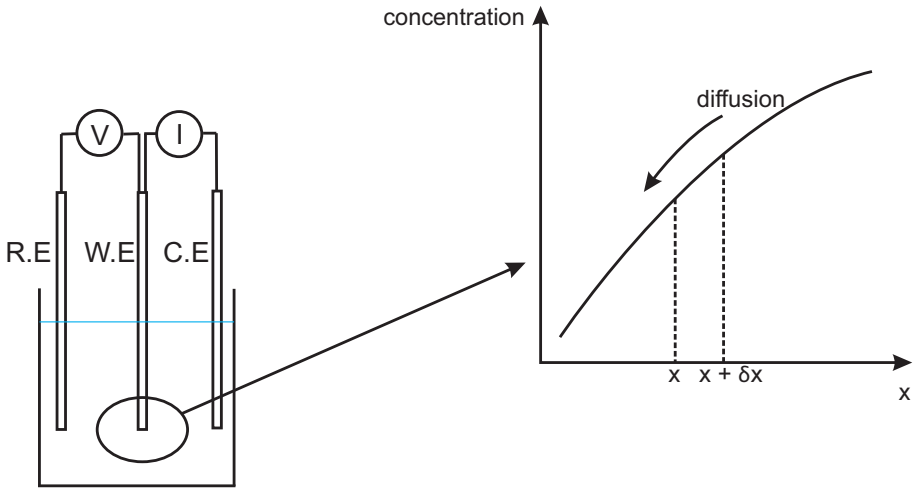


Figure 1.7: Schematic profile of concentration against the distance away from the electrode surface (x), the arrow shows the direction of diffusion.

Diffusion is the movement of species under the influence of a concentration gradient. Thus, the electroactive species that is consumed in the electron transfer reaction will move to the electrode surface from the bulk solution due to the concentration gradient in the depletion layer formed around the electrode. This mass transfer by

diffusion is described by Fick's laws [3]. Fick's first law relates the diffusive flux, j ($\mathrm{mol{\cdot}s^{-1}{\cdot}cm^{-2}}$), to the concentration gradient such that when this develops in only one direction (x) j is given by Eq. 1.4:

$$j = -D\frac{\partial c}{\partial x} \tag{1.4}$$

where D is the diffusion coefficient of the diffusing species and $\frac{\partial c}{\partial x}$ the concentration gradient. The negative sign indicates that the electroactive species moves *down* the direction of the concentration gradient.

Fick's second law predicts the evolution of the species concentration with time by relating the time-variation of the concentration at a given location with the net flux of species. When diffusion takes place only in one dimension (linear diffusion), the mathematical form of the second law is given by:

$$\frac{\partial c}{\partial t} = D(\frac{\partial^2 c}{\partial x^2}) \tag{1.5}$$

Under the experimental conditions of the electrochemical measurements carried out in this thesis, diffusion is the only active mass transport mode.

1.3.1.1 Convection

There are two different types of convection, which are natural convection and forced convection [2]. These are generated due to different reasons. Chemical transformation near the electrode area can lead to local density differences. This density

gradient leads to a flow in solution such that species move from denser to less dense regions. This phenomenon is defined as natural convection [2, 3]. It is almost impossible to avoid but it is not desirable in experiments because of its unpredictable, unquantitable and irreproducible nature [2, 3]. In order to minimise the influence of natural convection, the electrolysis time scale *should not* exceed 10 - 20 such that the amount of species consumed and generated near the electrode surface, that is, composition changes, are not very significant.

Another form of convection, forced convection, is induced by mechanic forces deliberately introduced into the system, often the electrode moves with respect to the solution or the solution is induced to flow. This flow is generally of a magnitude much larger than natural convection. The convective flux cause by forced convection is shown below in Eq.1.6 [12].

$$j = c\mathbf{v} \tag{1.6}$$

where, j is the flux, $\mathbf{v}$ is the solution velocity vector and c is the species concentration.

In the experiments carried out in this thesis, long electrolysis times have been avoided as well as forced convection such that this mass transport mechanism can be assumed as negligible when modeling the electrochemical response.

1.3.1.2 Migration

The third mode of mass transport is electromigration which results from the motion of charged species in the presence of an electric field. According to the nature of the charged species, this experiences different forces, for instance, an attractive force when a positively charged species is present around a positively charged electrode or anions around a negatively charged electrode[2].

The flux resulted from migration is described by Eq. 1.7 for a one-dimensional problem [2, 12]:

$$j = -\frac{zF}{RT} Dc \frac{\partial \phi}{\partial x} \tag{1.7}$$

where z is the charge on the electroactive species, R is the gas constant, T the absolute temperature, F the Faraday constant and c the species concentration.

As discussed above, in order to simplify the description of electrochemical systems, migration of the target species is effectively eliminated on experimental practice by adding an excess of supporting electrolyte in the working solution. Thus, most of the current will be carried in the solution by the charged species from the supporting electrolyte because of their much higher concentration and the contribution to the mass transport of the target ions by migration is significantly reduced [2]. Diffusion is therefore overwhelmingly the dominant mode of mass transport.

1.4 Butler-Volmer Electrode Kinetics

The kinetics of the electron transfer at the electrode/solution interface within the Butler-Volmer model [13] is presented in detail in this section. Most of the simulations carried out in this thesis are based on this model.

We consider a simple one electron transfer process:

$$A + e^- \underset{k_a}{\overset{k_c}{\rightleftarrows}} B \tag{1.8}$$

where, k_c is the rate constant of the reduction process and k_a the rate constant of electro-oxidation.

According to the Arrhenius equation, electron transfer rate constant k_a and k_c can be correlated with the Gibbs energies of activation ($\Delta G^{(\dagger)}$) as shown in Eq. 1.9 and Eq. 1.10 where A_c and A_a are the Arrhenius factors:

$$k_c = A_c exp \frac{-\Delta G_c^{(\dagger)}}{RT} \tag{1.9}$$

$$k_a = A_a exp \frac{-\Delta G_a^{(\dagger)}}{RT} \tag{1.10}$$

and considering the expressions for the activation energies the following equations are obtained:

$$k_c = k_c^0 exp \frac{-\alpha F(E - E_f^0)}{RT} \tag{1.11}$$

$$k_a = k_a^0 exp \frac{(1-\alpha) F(E - E_f^0)}{RT} \tag{1.12}$$

where, E_f^0 is the formal potential of redox couple, E the applied potential at the working electrode and α the transfer coefficient. The α value is always between 0 - 1. Within the transition state approach, the closer the α value to zero is, the more the transition state is reactant like in the case of a reduction [3].

The surface flux at the working electrode j_{net} relates to the rates of the reduction and oxidation processes (j) defined by the corresponding rate constant (k) and surface concentration of the reactant species (c_0) [2, 3]:

$$j = kc_0 \tag{1.13}$$

such that by combining Eq.1.13, Eq. 1.11 and Eq. 1.12, the following mathematical expression for the net flux j_{net} is obtained:

$$j_{net} = c_{A,0} \cdot k_c^0 exp\frac{-\alpha F(E - E_f^0)}{RT} - c_{B,0} \cdot k_a^0 exp\frac{(1-\alpha)F(E - E_f^0)}{RT} \tag{1.14}$$

When the system reaches the equilibrium, the net flux is zero and the Nernst relation applies:

$$E = E_f^0 + \frac{RT}{F} ln\frac{c_{A,0}}{c_{B,0}} \tag{1.15}$$

Considering both Eq.1.14 at the equilibrium ($j_{net} = 0$) and Eq.1.15, we obtain:

$$k_a^0 = k_c^0 = k^0 \tag{1.16}$$

where k^0 is the standard electron transfer rate constant.

Finally, k_c^0 and k_a^0 can be written in Eq. 1.17 and Eq. 1.18.

$$k_c = k^0 exp\frac{-\alpha F(E - E_f^0)}{RT} \tag{1.17}$$

$$k_a = k^0 exp\frac{(1-\alpha) F(E - E_f^0)}{RT} \tag{1.18}$$

Thus, the values of the standard electrochemical rate constant (k^0), the transfer coefficient (α) and the formal potential of the redox couple (E_f^0) are the parameters that define the electron transfer kinetics within the Butler-Volmer model.

Taking into account that the current (I / A) that flows upon the electron transfer process is directly related to the net flux at the electrode surface (j / (mol $\cdot$ cm$^{-2}\cdot$ s^{-1})) and the electrode area (A / cm^2):

$$I = FAj_{net} \tag{1.19}$$

the current-potential relationship predicted by the Butler-Volmer model is finally obtained:

$$I = FA \cdot (c_{A,0} \cdot k^0 exp\frac{-\alpha F(E - E_f^0)}{RT} - c_{B,0} \cdot k^0 exp\frac{(1-\alpha) F(E - E_f^0)}{RT}) \tag{1.20}$$

where a positive sign has been assigned to electro-reduction currents.

1.5 Electrochemical Techniques

In this section, the electrochemical techniques employed in this thesis for qualitative and quantitative analysis of the different systems will be introduced.

1.5.1 Cyclic Voltammetry at Macroelectrode

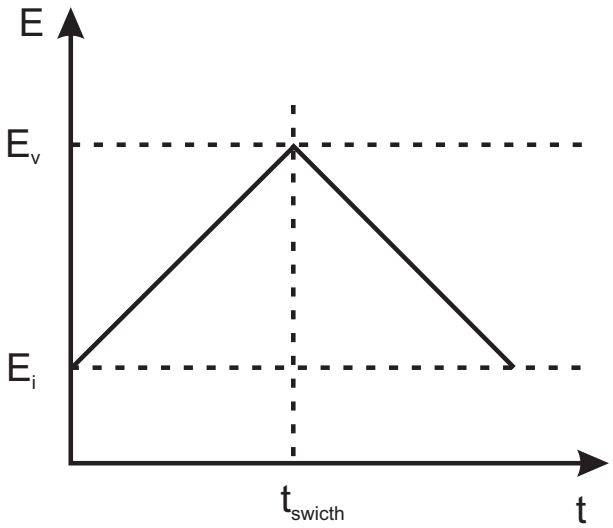


Figure 1.8: Schematic diagram of the potential-time perturbation applied during a cyclic voltammetry experiment.

Cyclic voltammetry (CV) is one of the most popular electrochemical methods [6, 14]. In CV measurements, an initial potential (E_i) is applied on the working electrode. The E_i value is usually selected (not necessarily) such that the target reactant is not initially oxidized or reduced and so a null current is recorded [3]. As shown in Figure 1.8, the potential is swept linearly from E_i to the vertex potential, E_v, at a certain scan rate ($V \cdot s^{-1}$). The scan direction depends on whether the process under study is an electroreduction process (scan towards negative potentials)

or an electro-oxidation (towards positive potentials). After reaching E_v, the scan direction is reversed towards the original value E_i [3].

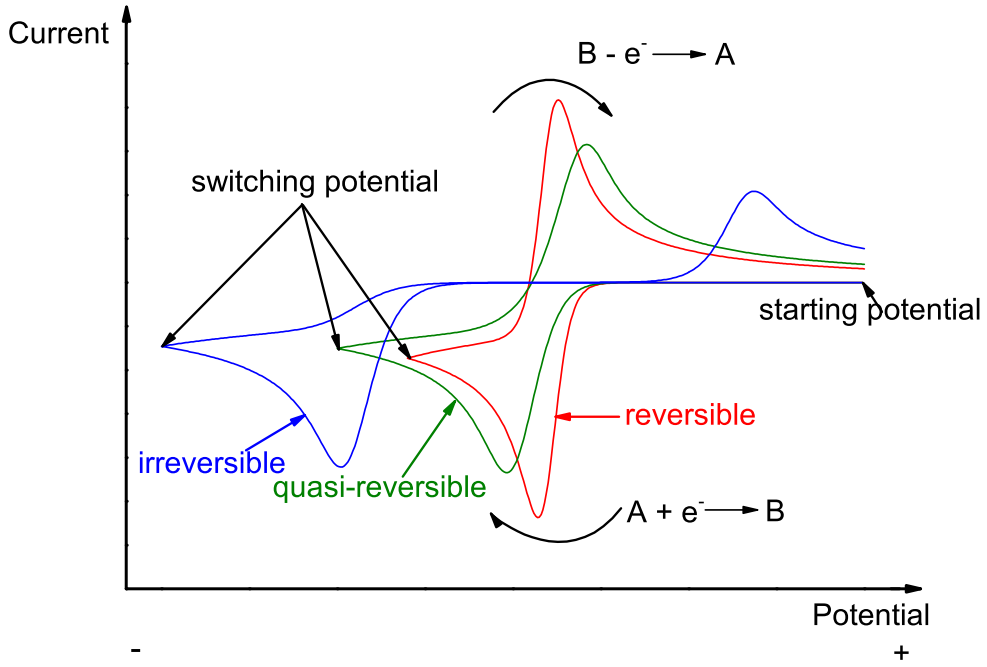


Figure 1.9: Cyclic voltammograms corresponding to reversible (red solid line), quasi-reversible (green solid line) and irreversible (blue solid line) electro-reduction processes.

Considering the electron transfer kinetics, three different situations can be found in cyclic voltammetry as shown in Figure 1.9. When the rate of electron transfer kinetics is much faster than the rate of mass transport (m_T shown in Eq. 1.21) the process is defined as electrochemically reversible [3]. Under these conditions, the peak current of the forward scan follows the Randles - Ševčík equation [3, 15, 16] (Eq. 1.22 at 298 K) such that the peak current (i_p) is proportional to the square

root of the scan rate ($\nu^{\frac{1}{2}}$) and $n^{\frac{3}{2}}$.

$$J = m_T c \tag{1.21}$$

where, J is the flux due to mass transport

$$i_p = 2.69 \times 10^5 n^{\frac{3}{2}} A c D^{\frac{1}{2}} \nu^{\frac{1}{2}} \tag{1.22}$$

where, A is the surface area of working electrode (cm^2), n is the number of electron transferred in the process, A + $ne^- \rightleftarrows$ B, c is the bulk concentration ($mol \cdot cm^{-3}$), D is the diffusion coefficient ($cm^2 \cdot s^{-1}$) and ν ($V \cdot s^{-1}$)is the scan rate.

The peak potentials (E_p) and peak-to-peak separation (ΔE_{app}, which is the difference between the forward and reverse peak potentials) of a reversible process are independent of the scan rate((shown in Eq. 1.23 and Eq. 1.24) [2].

$$|E_p - E_{\frac{p}{2}}| = 2.20 \frac{RT}{nF} \tag{1.23}$$

$$\Delta E_{app} = 2.3 \times \frac{RT}{nF} = \frac{59mV}{n}(298K) \tag{1.24}$$

where n is the number of electrons transferred, $E_{\frac{p}{2}}$ is the half-peak potential.

In the other extreme case where the electron transfer rate constant is much slower than the mass transport the system is referred as electrochemically irreversible (blue solid curve in Figure 1.9). In comparison with the reversible case, the peak potential

(E_p, shown in Eq. 1.25 for a simple one electron transfer process) depends on the scan rate and the peak-to-peak separation will increase with it [2, 3].

$$E_p = E_f^0 - \frac{RT}{\alpha F}[0.780 + ln(\frac{D^{\frac{1}{2}}}{k^0}) + ln(\frac{\alpha F \nu}{RT})^{\frac{1}{2}}] \tag{1.25}$$

The Randles - Ševčík equation for the forward peak current of totally irreversible process (Eq. 1.26) defines the peak current (i_p / A) as a function of the number of electrons transferred (n), the transfer coefficient (α), the geometric surface area of the working electrode (A / cm^2), the reactant diffusion coefficient (D / $cm^2 \cdot s^{-1}$)and its bulk concentration (c / $mol \cdot cm^{-3}$) and the scan rate (ν / ($V \cdot s^{-1}$)). As with the reversible case, the peak current scales with $\nu^{\frac{1}{2}}$.

$$i_p = 2.99 \times 10^5 n(\alpha n_a)^{\frac{1}{2}} D^{\frac{1}{2}} c A \nu^{\frac{1}{2}} \tag{1.26}$$

The intermediate case between totally irreversible and fully reversible processes corresponds to the so-called quasi-reversible systems, which is found in a large number of practical cases. The characterization of such systems is more complicated given that explicit expressions (such as those for fully reversible and fully irreversible processes) are not available and it is necessary the fitting of experimental and theoretical curves obtained with appropriate simulation programs. Matsuda and Ayabe [17] gave analytical criteria to classify reversible (Eq 1.27), quasi-reversible (Eq 1.28)

and irreversible (Eq 1.29) processes at stationary macro electrodes [18]:

$$\Lambda \geqslant 15; \Lambda \geqslant 0.3\nu^{\frac{1}{2}} cm \cdot s^{-1} \tag{1.27}$$

$$15 > \Lambda > 10^{-3}; 0.3\nu^{\frac{1}{2}} > k^0 > 2 \times 10^{-5}\nu^{\frac{1}{2}} cm \cdot s^{-1} \tag{1.28}$$

$$\Lambda \leq 10^{-3}; k^0 \leq 2 \times 10^{-5}\nu^{\frac{1}{2}} \tag{1.29}$$

where, $\Lambda = \dfrac{k^0}{(\dfrac{FD\nu}{RT})^{\frac{1}{2}}}$, the numerical values relate to 298 K and $\alpha = 0.5$.

1.5.2 Cyclic Voltammetry at Microelectrodes

A microelectrode refers to an electrode with a critical dimension from 0.1 μm to 50 μm [19]. They are widely applied in electrochemical studies for a number of reasons. Their small area improves the signal ratio of faradaic to capacitive currents and the small current that flows reduces the ohmic drop effects. It also enables us to simplify and use a two-electrode set-up instead of a three-electrode one [19]. Also, faster (electro)chemical kinetics can be studied and steady-state responses can be attained due to the more efficient diffusive mass transport of the electroactive species.

As shown in Figure 1.10, when the thickness of the diffusion layer is much smaller than the electrode radius r_e, the diffusion to the electrode surface is predominantly linear. As discussed above for macroelectrodes, this situation leads to peak-shaped voltammograms where the current decreases continuously after the peak potential

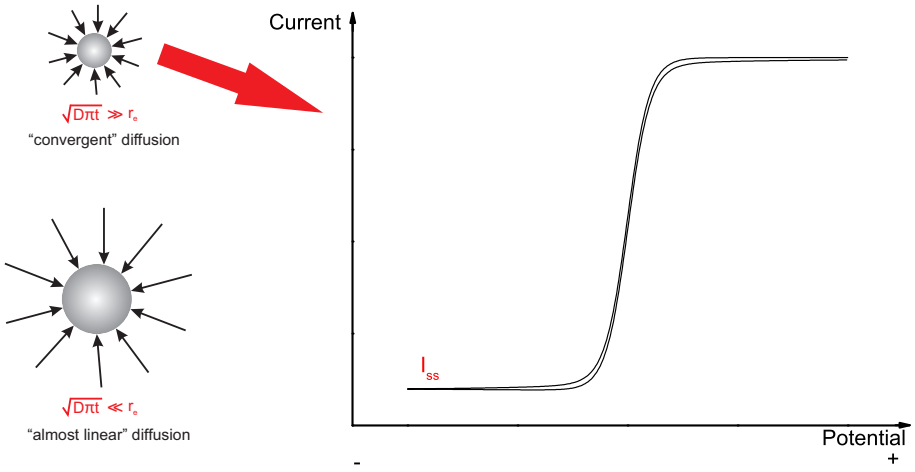


Figure 1.10: Steady-state cyclic voltammogram obtained at a microelectrode as a result of the efficient convergent diffusion.

due to the depletion of the electroactive species around the electrode surface. When the thickness of the diffusion layer is comparable to the electrode size, radial ("convergent") diffusion becomes more significant leading to a more efficient mass transport. As a result, the peaks of the voltammograms gradually disappear and finally, when the electrode size is small enough and/or the scan rate is slow enough, a steady-state response is reached and a sigmoidal voltammogram is obtained [2, 3]. This can be characterized by the half-wave potential and the limiting current. The value of the latter depends on the shape and size of the microdisc employed such that for the widely-used microdisc electrodes it is given by:

$$I = 4r_e DFc(disc) \tag{1.30}$$

whereas for spherical and hemispherical microelectrodes it is given by:

$$I = 4\pi r_e DFc(sphere) \tag{1.31}$$

$$I = 2\pi r_e DFc(hemisphere) \tag{1.32}$$

1.5.3 Square Wave Voltammetry

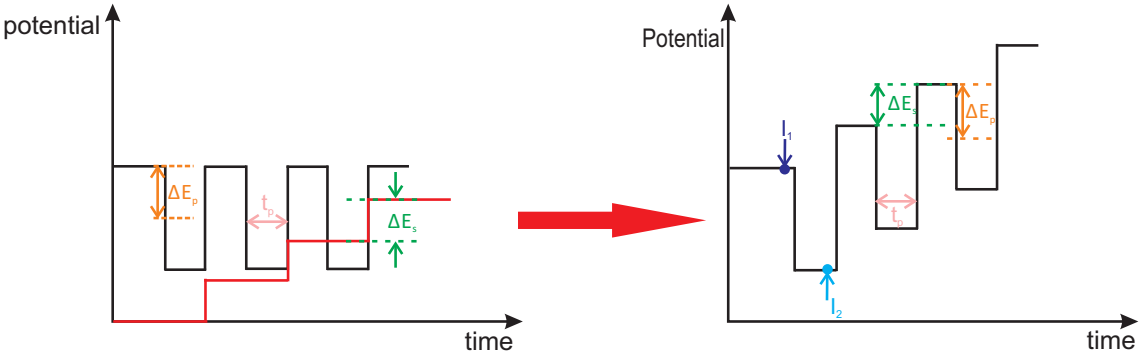


Figure 1.11: Waveform and signal in SWV indicating the square wave amplitude (ΔE_p), the staircase height (ΔE_s) and the pulse time (t_p). I_1 and I_2 are the points where the current is sampled in each cycle.

Square wave voltammetry (SWV) is a commonly-used pulse technique with well-known advantages in electroanalysis, such as well-defined peak-shaped voltammograms, reduced capacitative effects and high sensitivity [3, 20–25]. As shown in Figure 1.11, the potential-time program in square wave voltammetry results from the combination of a square wave and a potential staircase with the same potential cycle period. The square wave amplitude (ΔE_p), the staircase height (ΔE_s) and the pulse time (t_p) defines the characteristics of the applied perturbation.

In SWV the current is recorded twice in each cycle (I_1 and I_2 in Figure 1.11) and

the net signal is given by the difference between the currents measured at points 1 and 2 (in Eq. 1.33). This is plotted against the staircase potential as shown in Figure 1.12 such that a peak is obtained and the interference of background currents (including the charging current) are greatly reduced.

$$I_{sig} = I_1 - I_2 \tag{1.33}$$

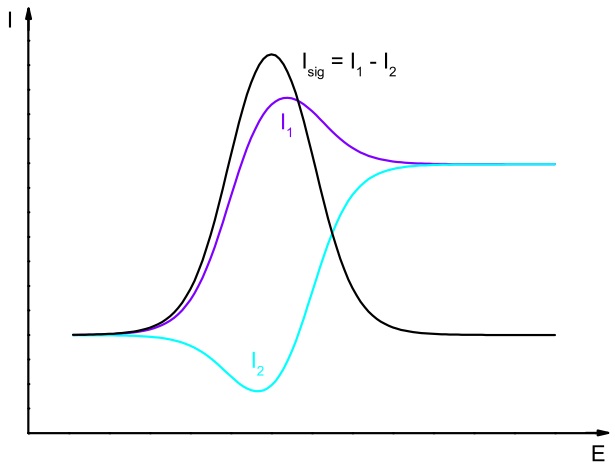


Figure 1.12: Net signal (black solid line) in a typical square wave voltammetry experiments. The purple solid line corresponds to the current measured at point 1 (in Figure 1.11) and the blue solid line to the current at point 2 (in Figure 1.11).

1.5.4 Chronoamperometry

Potential step chronoamperometry is an electrochemical technique where a constant potential step is applied for a certain time as shown in Figure 1.13 and the variation

of the current response with time is studied. This technique is widely used to obtain information about diffusion coefficients [2, 3, 26–29], analyte concentration [2, 3, 26–29], number of electrons transferred [2, 3, 30, 31] and electrode surface area.

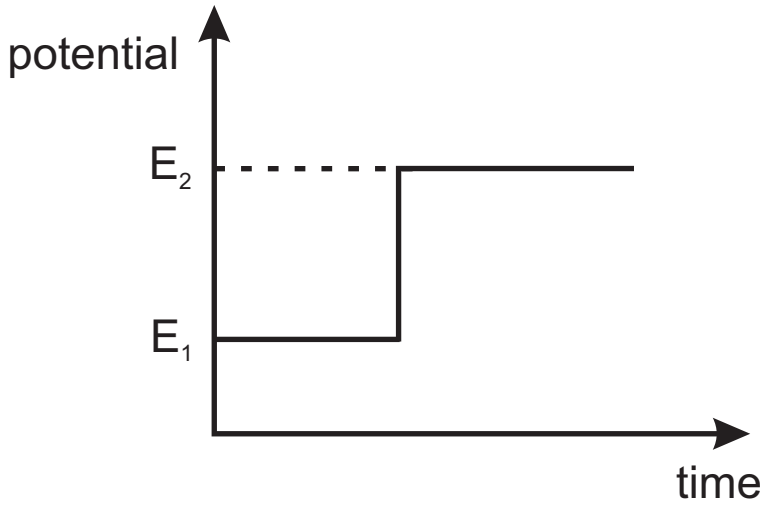


Figure 1.13: Potential-time perturbation applied in chronoamperometry.

At the initial potential (E_1) of a chronoamperometry experiment no faradaic current flows in the system and subsequently the potential is set at a value (E_2) where the electrolysis process takes place at its maximum rate, governed by the mass transport of the reactant species [3, 32]. The recorded current is larger at the beginning of the experiment due to the steeper concentration gradients of the electroactive species that is consumed rapidly at the electrode surface.

The current-time dependence recorded in a chronoamperometry experiments depends on the electrode size and shape. This relationship can be described by Cottrell equation in Eq. 1.34:

$$I = \frac{nFA\sqrt{D}c^*}{\sqrt{\pi t}} \tag{1.34}$$

On a disc microelectrode as those employed in this thesis, it can be calculated accurately from the Shoup and Szabo equation [2, 3, 32, 33]:

$$i = 4nFrDcf(\tau) \tag{1.35}$$

$$f(\tau) = 0.7854 + 0.8863\tau^{-\frac{1}{2}} + 0.2146exp(-0.7823\tau^{-\frac{1}{2}}) \tag{1.36}$$

where, τ is the dimensionless time.

Eq. 1.35 predicts the current-time response with a maximum error of 0.6 % [3, 32].

Bibliography

[1] W. Schmickler and E. Santos, *Interfacial electrochemistry*, volume 134 (Springer, 1996).

[2] A. J. Bard and L. R. Faulkner, *Electrochemical methods: fundamentals and applications*, volume 2 (Wiley New York, 1980).

[3] R. G. Compton and C. E. Banks, *Understanding voltammetry (2^{nd} Edition)* (Imperial College Press, 2007).

[4] E. J. Dickinson, J. G. Limon-Petersen, N. V. Rees and R. G. Compton, *Journal of Physical Chemistry C* **113** (2009) 11157–11171.

[5] I. Streeter and R. G. Compton, *Journal of Physical Chemistry C* **112** (2008) 13716–13728.

[6] C. M. Brett and A. M. O. Brett, *Electrochemistry: principles, methods, and applications*, volume 4 (Oxford university press Oxford, 1993).

[7] H. L. Helmholtz, *Annalen der Physik und Chemie* **7** (1879) 337–387.

[8] G. Gouy, *Journal de Physique* **9** (1910) 457–468.

[9] D. L. Chapman, *Philosophical Magazine* **25** (1913) 475–481.

[10] H. Wang and L. Pilon, *Journal of Physical Chemistry C* **115** (2011) 16711–16719.

[11] O. Stern, *Elektrochemistry* **7** (1879) 337–387.

[12] A. M. Bond, *Broadening electrochemical horizons: principles and illustration of voltammetric and related techniques* (Oxford University Press, 2002).

[13] J. A. V. Butler, *Transactions of the Faraday Society* **19** (1924) 734–739.

[14] G. A. Mabbott, *Journal of Chemical Education* **60** (1983) 697.

[15] J. Randles, *Transactions of the Faraday Society* **44** (1948) 322–327.

[16] Ševčík A, *Collection of Czechoslovak Chemical Communications* **13** (1948) 349–377.

[17] H. Matsuda and Y. Ayabe, *Zeitschrift für Elektrochemie, Berichte der Bunsengesellschaft für physikalische Chemie* **59** (1955) 494–503.

[18] R. S. Nicholson, *Analytical Chemistry* **37** (1965) 1351–1355.

[19] M. I. Montenegro, I. Montenegro, M. A. Queirós and J. L. Daschbach, *Microelectrodes: Theory and Applications: Theory and Applications*, volume 197 (Springer, 1991).

[20] E. Laborda, A. Molina, F. Martínez-Ortiz and R. G. Compton, *Electrochimica Acta* **73** (2012) 3–9.

[21] A. Molina, E. Laborda, F. Martínez-Ortiz, D. F. Bradley, D. J. Schiffrin and R. G. Compton, *Journal of Electroanalytical Chemistry* **659** (2011) 12–24.

[22] J. G. Osteryoung and R. A. Osteryoung, *Analytical Chemistry* **57** (1985) 101A–110A.

[23] Y. Wang, E. Laborda and R. G. Compton, *Journal of Electroanalytical Chemistry* **670** (2012) 56–61.

[24] P. Lee, D. Lowinsohn and R. Compton, *Analyst* **139** (2014) 3755–3762.

[25] M. Lovrić and Š. Komorsky-Lovric, *Journal of Eectroanalytical Chemistry and Interfacial Electrochemistry* **248** (1988) 239–253.

[26] Y. Wang, E. Laborda, K. R. Ward, K. Tschulik and R. G. Compton, *Nanoscale* **5** (2013) 9699–9708.

[27] L. Xiong, E. O. Barnes and R. G. Compton, *Sensors and Actuators B: Chemical* **200** (2014) 157–166.

[28] L. Xiong, A. M. Fletcher, S. Ernst, S. G. Davies and R. G. Compton, *Analyst* **137** (2012) 2567–2573.

[29] L. Xiong, D. Lowinsohn, K. R. Ward and R. G. Compton, *Analyst* **138** (2013) 5444–5452.

[30] A. Baranski, W. Fawcett and C. Gilbert, *Analytical Chemistry* **57** (1985) 166–170.

[31] T. Nishiumi, M. M. Abdul and K. Aoki, *Electrochemistry Communications* **7** (2005) 1213–1217.

[32] L. Xiong, L. Aldous, M. C. Henstridge and R. G. Compton, *Analytical Methods* **4** (2012) 371–376.

[33] D. Shoup and A. Szabo, *Journal of Electroanalytical Chemistry and Interfacial Electrochemistry* **140** (1982) 237–245.

Chapter 2

Electrochemistry at the Nanoscale - Simulation

This chapter reports an overview of the basis of the home-written simulation programs employed in this thesis to model the electrochemical response of nanoparticle-modified electrode and to characterise the electron transfer kinetics of the nanoparticles by fitting of experimental voltammetry. These programs were written and debugged by Dr. Kristopher R. Ward and Dr. Eduardo Laborda with all simulation of experimental data carried out by the author of this thesis.

Compared to bulk materials, nanoparticulate materials offer a much larger area-to-volume ratio and also properties such as the surface structure and the electronic properties [1–3] may change at the nanoscale [1, 2]. These changes can lead to different electrochemical behaviour, so-called "nano-effects", such that the electron transfer kinetics is changed with respect to the macroscale. Electrocatalytic nanoeffects are of major interest, for example, for the development of electrochemical sensors of higher sensitivity and selectivity [4–7] and of energy transformation devices of higher efficiency [8–12].

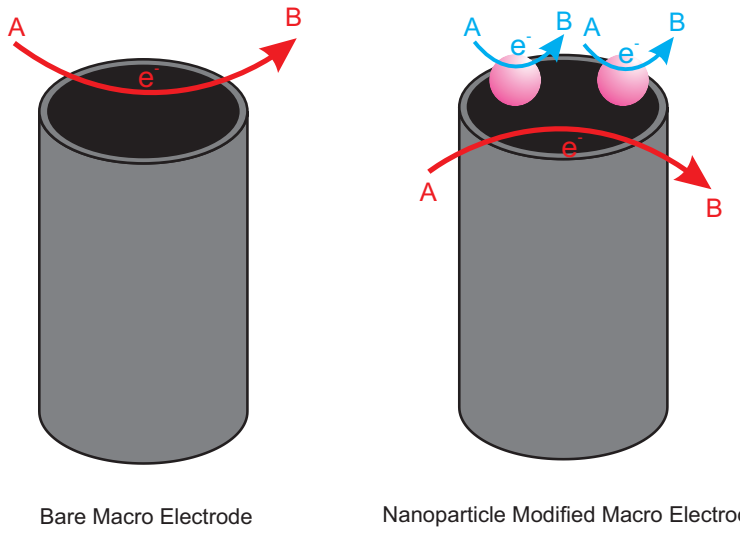


Figure 2.1: Schematic diagram of an electrochemical reaction taking place on bare and nanoparticle-modified macroelectrodes. The two processes may occur at different rates.

As shown schematically in Figure 2.1, electrochemical kinetics can be different on the nanoparticle and substrate surfaces. However, the mass transport conditions differ between a bare electrode and a nanoparticle-modified one. Understanding the latter is key to unravelling changed electron transfer kinetics at the nanoscale. Thus, mass transport at a nanoparticle-modified macroelectrode can be divided into four categories depending on the experimental time scale, the nanoparticle size and the particle density as shown in Figure 2.2. When the nanoparticle density is small (large inter-particle distance) and the diffusion layer is small compared to the particle size (short experimental time scale), diffusion towards the nanoparticle surface is linear as corresponds to case 1 in Figure 2.2. As the experimental time scale is longer, convergent diffusion will be more significant and the peak-shaped voltammogram will evolve towards a sigmoidal one (case 2). When the nanoparticle coverage is

increased and so the inter-particle distance is smaller, the diffusion zones of adjacent nanoparticles starts to overlap and the nanoparticles are no longer diffusionally-independent (cases 3 and 4). When the diffusion layers are strongly overlapped, the diffusion is linear towards the entire array and the electrochemical response is analogous to that of a macroelectrode [13–18].

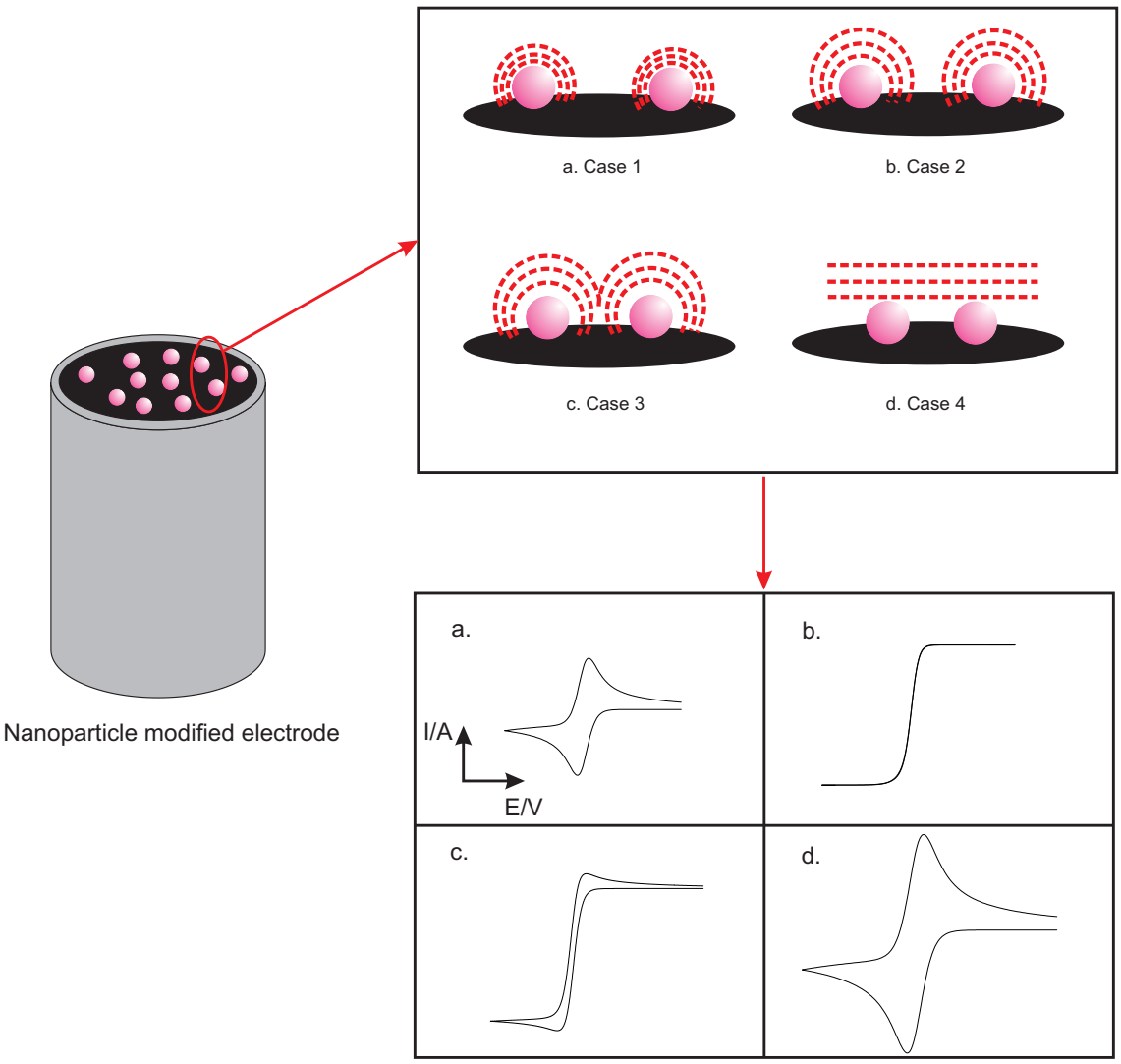


Figure 2.2: Schematic diagram of the possible diffusion domains at a nanoparticle-modified macroelectrode.

Changed mass transport can affect the electrochemical response in a way that

the experimental data can be misinterpreted in terms of electrocatalysis [13, 19]. However, "authentic" *electrocatalytic* effects refer to the enhancement of the electron transfer kinetics. Accordingly, simulation programs were developed for the author's use in our group by Dr. Kristopher R. Ward and Dr. Eduardo Laborda in order to predict accurately the voltammetric response on nanoparticle-modified macroelectrodes taking into account both kinetic and mass transport effects. This enables the rigorous identification and quantification of electrocatalytic nanoeffects.

2.1 Numerical Simulation Strategy: The Diffusion Domain Approximation

The simulation of the surface of an electrode modified by nanoparticles randomly distributed is a very computationally-expensive, 3-dimensional problem [13–18, 20, 21]. Nevertheless, some assumptions can be made in order to obtain accurate results with acceptable runtimes. First, given that the substrate is large and there is a large number of particles, the different local environment at the edge of the macrodisc can be neglected. Also, the nanoparticles can be considered as evenly distributed since it has been theoretically demonstrated that the difference between the voltammograms of nanoelectrode arrays regularly and randomly distributed is not significant under typical experimental conditions [16]. Therefore, as shown in Figure 2.3.b, the electrode surface can be supposed as composed of an array of *identical* unit cells, each centered around a single nanoparticle, such that only one cell needs to

be simulated. Finally, and most importantly, by making use of the "diffusion domain approximation" the unit square cell is approximated as a cylindrical cell of the same area (Figure 2.3.b) such that the three-dimensional problem is simplified to a tractable two-dimensional one [13–15, 20, 21].

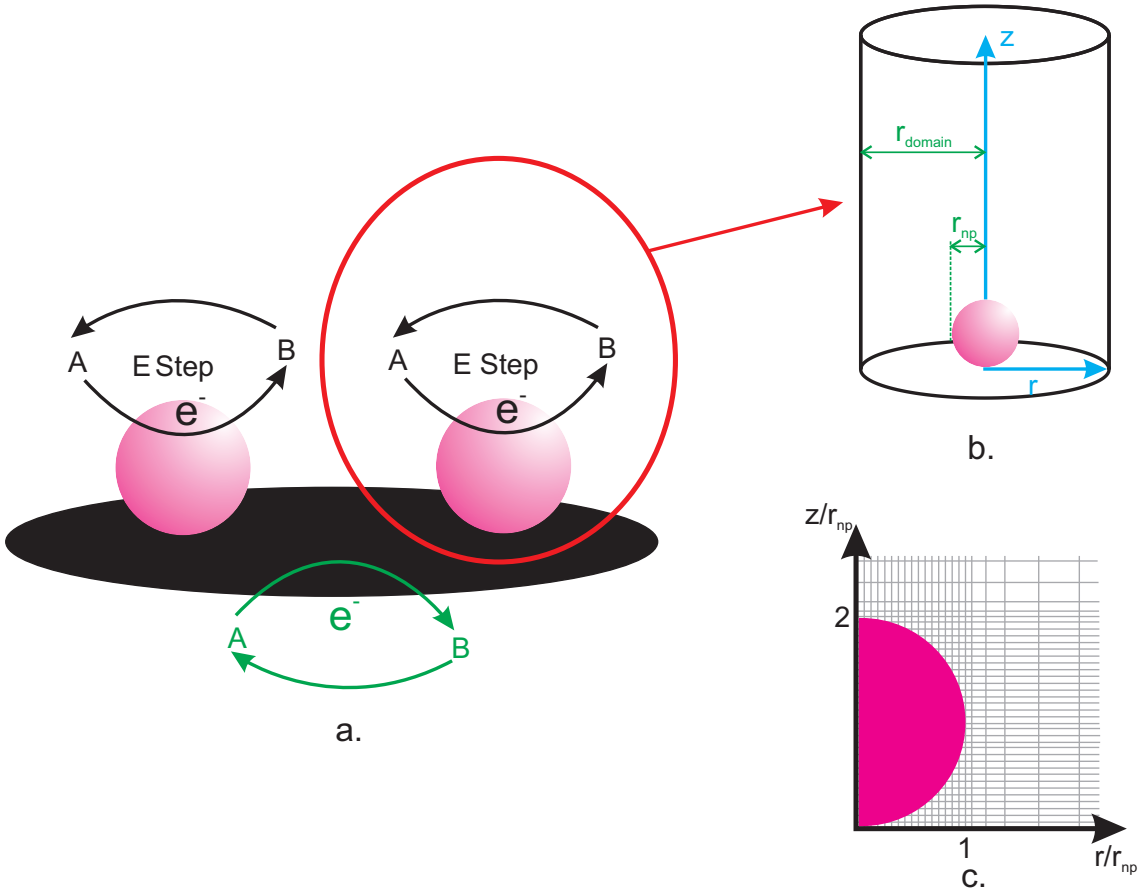


Figure 2.3: a. Schematic diagram of an electron transfer process taking place on a nanoparticle-modified electrode where the supporting substrate is inert; b. Coordinate system and diffusion domain assigned to each spherical nanoparticle where r_{domain} and r_{np} are the radius of the cylindrical cell and the nanoparticle, respectively; c. Schematic diagram of the typical discretisation for the simulation space.

Under fully-supported conditions and in the absence of convection, the mass transport of electroactive species in the unit cell is described by Fick's second law

in cylindrical coordinates:

$$\frac{\partial c}{\partial t} = D(\frac{\partial^2 c}{\partial r^2} + \frac{1}{r}\frac{\partial c}{\partial r} + \frac{\partial^2 c}{\partial z^2}) \tag{2.1}$$

where r and z are defined in Figure 2.3.b.

The corresponding boundary conditions are summarised in Table 2.1. With respect to the surface conditions, the process, A + e^- → B, is modelled by Butler-Volmer kinetics:

$$D_A \frac{\partial [A]_0}{\partial x} = k^0 [exp((-\alpha)\frac{F}{RT}(E - E_f^0))[A]_0 - exp((1-\alpha)\frac{F}{RT}(E - E_f^0))[B]_0] \tag{2.2}$$

Table 2.1: Boundary conditions

	Boundary	Terms
Initial conditions	$\tau \leqslant 0$	$c_x = c_x^*$
Axial symmetry	r = 0	$\frac{\partial c}{\partial r} = 0$
Bulk solution	r $\longrightarrow \infty$, z $\longrightarrow \infty$	$c_x = c_x^*$
Array	$r = r_{domain}$	$\frac{\partial c}{\partial r} = 0$
Particle surface	$(\frac{r}{r_{np}})^2 + (\frac{z}{r_{np}} - 1)^2 = 1$	Butler-Volmer
Substrate surface	z = 0, $\frac{r}{r_{np}} > 1$	Butler-Volmer

Given that each unit cell is surrounded by identical cells, the boundary between

them must have zero flux at r = r_{domain}. Also, noting the symmetry about the z-axis, there is no material flux through r=0. Finally, at the beginning of the experiment (initial conditions) and in the bulk solution the initial concentrations of the electroactive species are not disturbed by the application of the electrical perturbation.

Simulation programs have been developed in our group by Dr. Kristopher R. Ward and Dr. Eduardo Laborda in order to solve the above problem for nanoparticles of different geometries by finite-difference methods [19, 23]. Thus, time and spatial coordinates are adequately discretised (to ensure convergent results) such that a higher density of nodes are situated where the species concentrations show sharp changes, that is, next to the substrate and particle surfaces. The space derivatives are approximated by 2- and 3-point finite differences and the time integration is performed following the Alternating Direction Implicit (ADI) method that is widely employed for efficient simulations of two-dimensional systems [23].

By making use of the home-written simulation software, the voltammetric response of a nanoparticle-modified macroelectrode can be predicted by providing the program with the kinetic and thermodynamic parameters of the (electro)chemical reactions of the system (in solution and at the substrate and nanoparticle surfaces), the concentration and diffusion coefficients of the participating species and the characteristics of the electrode modification, that is, the nanoparticle size, shape and coverage Θ:

$$\Theta = \frac{\pi r_{np}^2 N}{A} \tag{2.3}$$

where N is the total number and A is the substrate area of the supporting substrate.

Bibliography

[1] R. J. White, R. Luque, V. L. Budarin, J. H. Clark and D. J. Macquarrie, *Chemical Society Reviews* **38** (2009) 481 – 494.

[2] R. A. Van Santen, *Accounts of Chemical Research* **42** (2009) 57–66.

[3] D. Uzio and G. Berhault, *Catalysis Reviews* **52** (2010) 106 – 131.

[4] G. Hu, Y. Ma, Y. Guo and S. Shao, *Electrochimica Acta* **53** (2008) 6610 – 6615.

[5] L. Zhang and X. Jiang, *Journal of Electroanalytical Chemistry* **583** (2005) 292 – 299.

[6] P. Kannan, S. Sampath and S. A. John, *Journal of Physical Chemistry C* **114** (2010) 21114–21122.

[7] Y. Cui, C. Yang, W. Zeng, M. Oyama and W. Pu, *Analytical Sciences* **23** (2007) 1421–1425.

[8] D. Astruc, *Nanoparticles and catalysis* (Wiley Online Library, 2008).

[9] S. Park, Y. Xie and M. J. Weaver, *Langmuir* **18** (2002) 5792 – 5798.

[10] M. Hepel, *Journal of the Electrochemical Society* **145** (1998) 124 – 134.

[11] M. S. El-Deab and T. Ohsaka, *Electrochemistry Communications* **4** (2002) 288 – 292.

[12] S. Yan, S. Zhang, Y. Lin and G. Liu, *Journal of Physical Chemistry C* **115** (2011) 6986 – 6993.

[13] R. G. Compton and C. E. Banks, *Understanding voltammetry,2nd Edition* (Imperial College Press, 2007).

[14] Y. Wang, K. R. Ward, E. Laborda, C. Salter, A. Crossley, R. M. Jacobs and R. G. Compton, *Small* **9** (2013) 478–486.

[15] K. R. Ward, N. S. Lawrence, R. S. Hartshorne and R. G. Compton, *Journal of Physical Chemistry C* **115** (2011) 11204–11215.

[16] S. R. Belding and R. G. Compton, *Journal of Physical Chemistry C* **114** (2010) 8309–8319.

[17] Y.-G. Zhou, F. W. Campbell, S. R. Belding and R. G. Compton, *Chemical Physics Letters* **497** (2010) 200–204.

[18] S. R. Belding, F. W. Campbell, E. J. Dickinson and R. G. Compton, *Physical Chemistry Chemical Physics* **12** (2010) 11208–11221.

[19] K. R. Ward, M. Gara, N. S. Lawrence, R. S. Hartshorne and R. G. Compton, *Journal of Electroanalytical Chemistry* **695** (2013) 1–9.

[20] I. Streeter, R. Baron and R. G. Compton, *Journal of Physical Chemistry C* **111** (2007) 17008–17014.

[21] I. Streeter and R. G. Compton, *Journal of Physical Chemistry C* **111** (2007) 18049–18054.

[22] T. J. Davies and R. G. Compton, *Journal of Electroanalytical Chemistry* **585** (2005) 63–82.

[23] R. G. Compton, E. Laborda and K. R. Ward, *Understanding voltammetry: simulation of electrode process* (Imperial College Press, 2014).

Chapter 3

Experimental Methods

In this chapter, general experimental approaches applied in this thesis are introduced including chemical reagents, instrumentation details, electrode modification and characterization methods. Full experimental information for each particular project is described in the individual chapters.

3.1 Chemical Reagents

Table 3.1 summarizes all the chemicals used in this thesis. They were used as received, without further purification. All solutions were prepared using deionised water with resistivity of 18.2 MΩ cm (25 °C).

Table 3.1: General chemical reagents used in this thesis

Chemicals	Chemical Formula	Purity	Supplier
Sodium phosphate monobasic dihydrate	$NaH_2PO_4 \cdot 2H_2O$	> 99 %	Sigma-Aldrich
Potassium sulphate	K_2SO_4	> 99 %	Sigma-Aldrich
Sodium sulphate	Na_2SO_4	> 99 %	Sigma-Aldrich
Sodium perchlorate monohydrate	$NaClO_4 \cdot H_2O$	> 98 %	Sigma-Aldrich
Potassium chloride	KCl	99.0-100.0 %	Sigma-Aldrich
Sodium chloride	NaCl	> 99 %	Sigma-Aldrich
Hydrochloric acid	HCl	> 37 %	Fisher
Acetic acid	CH_3COOH	> 99 %	Sigma-Aldrich
Sodium acetate trihydrate	CH_3OONa	> 99 %	Sigma-Aldrich
Sodium hydroxide	NaOH	> 97 %	Sigma-Aldrich
Sodium phosphate dibasic	Na_2HPO_4	> 99 %	Sigma-Aldrich
Sodium nitrite	$NaNO_2$	> 99 %	Sigma-Aldrich
Sodium borohydride	$NaBH_4$	98 %	Lancaster
Lead(II) nitrate	$Pb(NO_3)_2$	> 99.5 %	BDH
Hexadecyltrimethylammonium bromide (CTAB)	$CH_3(CH_2)_{15}N^+(CH_3)_3$ Br^-	> 99 %	Sigma-Aldrich
Gold(III) chloride trihydrate	$HAuCl_4 3H_2O$	> 99 %	Sigma-Aldrich
Citrate-capped gold nanoparticles	Au-NPs	-	Mintek
Sulphuric acid	H_2SO_4	> 95 %	Fisher Chemicals
Trisodium citrate	$C_6H_5Na_3O_7$	> 99 %	Sigma-Aldrich
Citrate-gold nanoparticles (1.8 nm)	Au-NPs	-	Nanopartz

3.2 Electrochemistry Experiments

All electrochemical experiments were performed using a three-electrode set-up with an Autolab PGStat 20 computer-controlled potentiostat (Eco-Chemie, Utrecht, Netherlands). A platinum wire was employed as a counter electrode and a saturated calomel electrode (SCE, Radiometer, Copenhagen) as a reference electrode. A bare, modified glassy carbon electrode (GCE, 3.0 mm diameter, BAS, Technical, UK) acted as working electrode. Prior to electrochemical measurements, the GC electrode was polished before use with diamond pastes (Kent, UK) of decreasing sizes (3.0, 1.0 and 0.1 mm) and sonicated in an ultrasound bath. All the electrochemistry experiments were carried out at 298 K.

3.3 Synthesis and Modification of Au-NPs/GCE

Wet chemistry [1–5] and direct electrodeposition [1, 6–9] are the two most widely used approaches to synthesize nanoparticles. There are advantages and disadvantages for both methods. For direct electrochemical deposition, it is feasible to obtain higher coverages with surfactant free nanoparticles on a short time scale. On the other hand, a much higher heterogeneity of size distributions for nanoparticles may be introduced by electrodeposition in comparison with wet chemistry synthesis [1]. In this thesis, different experimental conditions for electrodeposition are discussed and optimized. Experimental details are given in section 6.1.

For the wet chemistry method, there is a better control of particle size and dis-

tributions, however, it is quite unlikely to avoid the use of surfactants and the whole process is time consuming [1, 3]. Once the solution is prepared, gold nanoparticles can be modified onto glassy carbon electrode surface either by physical adsorption [3] or electrophoresis. Specific experimental details are explained in each particular chapter.

3.4 Characterization Methods

3.4.1 UV-Vis Spectroscopy

Electrons in molecules can be excited by adsorbing ultraviolet or visible light. The ratio of intensity of light before (I_0) and after (I) passing though a sample, which is known as transmittance, is measured in UV-Vis measurements. A typical UV-Vis spectrum is displayed as absorbance, A. This is directly related to the path length of the beam (b), the solution concentration(c) and the extinction coefficient of the species (ε) as stated in Beer's Law (Eq. 3.1) [10]. UV-Vis spectra are always used as an initial means to determine concentration of nanoparticles by applying Eq. 3.1.

$$log_{10}\frac{I_0}{I} = A = \varepsilon \cdot b \cdot c \tag{3.1}$$

where, A represents adsorbance, b is the path length of the beam, c is the solution concentration.

Gold nanoparticles exhibit some unique optical properties. These optical prop-

erties are governed by plasmons which arises from the collective oscillation of free electrons in the metal [11]. The surface plasmon peak shifts to lower wavelengths with a decrease of nanoparticle size [12]. Therefore, an estimation of gold nanoparticle size can be achieved by examining the wavelength of adsorbed light [12, 13]. However, media and capping agent strongly influence surface plasmon resonance of nanoparticles such that other methods are needed in order to obtain precise information of nanoparticle size.

All the UV-Vis experiments in this thesis were performed with an ultravioletvisible U-2001 spectrophotometer (HITACHI, UK).

3.4.2 Transmission Electron Microscopy (TEM)

The acquisition of accurate information of nanoparticle size is essential in this thesis. As mentioned in section 3.4.1 there are limitations to the ability of UV-Vis spectra to provide such precise information of particle size [12], hence, transmission electron microscopy (TEM) is employed for this purpose. Unlike conventional optical microscopes, electrons are used to generate images down to the nanometer range in TEM [14]. An electron gun located at the top of a TEM microscope generates electron beams to interact with the sample in a vacuum. An image can be obtained by the interaction of electrons transmitted through ultra-thin samples. TEM results presented in this thesis were carried out with a FEI TECNAI T20 (200 kV/LaB6-filament/EDX-Oxford-detector).

3.4.3 Scanning Electron Microscope (SEM)

Besides TEM, scanning electron microscope (SEM) is also a popular technique to characterize nanoparticles. Compared to TEM, SEM can not only provide information about particle size but also give details of surface morphology for a nanoparticle modified electrode. This results from the different principles of image formation for these two techniques. In TEM, images are obtained by electrons *"transmited"* through samples. In SEM however, the image is formed by scanning (or rastering) an electron beam (known as the primary electrons) across the sample surface [15, 16]. In a typical SEM system, an electron beam is generated from an electron gun by heating a tungsten filament. This electron beams interact with surface atoms after passing through a series of lenses. Detectors will collect high energy electron beams reflected from interaction between the initial electron beam and the sample by elastic scattering or secondary emission [15]. Images are finally formed after current amplification.

3.4.4 Electrochemistry Characterization

Both TEM and SEM can provide detailed information about nanoparticle size. However, these techniques are expensive and time consuming so that it is quite impossible to check every individual sample after each electrochemical measurement. Therefore, a fast *in-situ* electrochemical characterization method was developed in our group which allows characterization of nanoparticle modified electrodes after ev-

ery measurement. This method consists of a surface area characterization by the underpotential deposition (UPD) of lead and quantification of the amount of gold deposited on the electrode surface estimated from the anodic stripping of gold in hydrochloric acid. Details of this approach are given in chapter 4.

3.4.5 X-ray Photoelectron Spectroscopy (XPS)

TEM and SEM can only provide the physical structure and surface morphology of nanoparticles or a nanoparticle modified electrode surface. However, in order to reveal chemical information about a solid surface, X-ray photoelectron spectroscopy (XPS) is one of the most popular techniques. XPS can provide the elemental composition of the outer surface of a solid [17]. XPS measurements must be carried out under ultra-vacuum conditions. Firstly, electrons on the outer surface of solid within a depth of 10 nm are excited after the surface is irradiated by a beam of X-rays. Secondly, photoelectrons will then be collected by an electron collection lens and then be analysed by an electron energy analyser and an electron detector. Finally, XPS spectra can be obtained by plotting the number of electrons detected (counts) versus the binding energy of the electrons detected. Each element shows its own characteristic binding energy position and peak based on its physical properties and its surrounding chemical environment [18]. Therefore, composition and determination of elements can be achieved.

Bibliography

[1] R. M. Penner, *Journal of Physical Chemistry B* **106** (2002) 3339–3353.

[2] N. R. Jana, L. Gearheart and C. J. Murphy, *Journal of Physical Chemistry B* **105** (2001) 4065–4067.

[3] Y. Cui, C. Yang, W. Zeng, M. Oyama and W. Pu, *Analytical Sciences* **23** (2007) 1421–1425.

[4] C. J. Murphy and N. R. Jana, *Advanced Materials* **14** (2002) 80–82.

[5] M. Oyama, *Analytical Sciences* **26** (2010) 1–12.

[6] E. Sheridan, J. Hjelm and R. J. Forster, *Journal of Electroanalytical Chemistry* **608** (2007) 1–7.

[7] W. Plieth, H. Dietz, A. Anders, G. Sandmann, A. Meixner, M. Weber and H. Kneppe, *Surface Science* **597** (2005) 119–126.

[8] T. Hezard, K. Fajerwerg, D. Evrard, V. Collière, P. Behra and P. Gros, *Journal of Electroanalytical Chemistry* **664** (2012) 46–52.

[9] D. Xuan and G. Richard, *Analytical Sciences* **22** (2006) 567–570.

[10] B. Clark, T. Frost and M. Russell, *UV Spectroscopy: techniques, instrumentation and data handling*, volume 4 (Springer, 1993).

[11] C. S. Kumar, *UV-VIS and photoluminescence spectroscopy for nanomaterials characterization* (Springer, 2013).

[12] W. Haiss, N. T. Thanh, J. Aveyard and D. G. Fernig, *Analytical Chemistry* **79** (2007) 4215–4221.

[13] X. Liu, M. Atwater, J. Wang and Q. Huo, *Colloids and Surfaces B: Biointerfaces* **58** (2007) 3–7.

[14] D. B. Williams and C. B. Carter, *The transmission electron microscope* (Springer, 1996).

[15] J. I. Goldstein, D. E. Newbury, P. Echlin, D. C. Joy, C. Fiori, E. Lifshin *et al.*, *Scanning electron microscopy and X-ray microanalysis. A text for biologists, materials scientists, and geologists.* (Plenum Publishing Corporation, 1981).

[16] D. McMullan, *Scanning* **17** (1995) 175–185.

[17] P. Van der Heide, *X-ray photoelectron spectroscopy: an introduction to principles and practices* (John Wiley & Sons, 2011).

[18] S. Hüfner, *Photoelectron spectroscopy: principles and applications* (Springer, 2003).

Chapter 4

Electrochemical Characterization of Gold Nanoparticle Modified Glassy Carbon Electrodes

In this chapter, a fast and simple *in situ* approach is presented for the characterization of gold nanoparticles using electrochemical experiments. The average size and number of nanoparticles deposited on a glassy carbon electrode can be determined from the value of the total surface area and the amount of gold obtained in hydrochloric acid, respectively. Oxidation/reduction of gold in sulphuric acid is the commonly used method to characterize surface area of gold but it shows some drawbacks for gold nanoparticles (as discussed in sections 4.1). The morphology of the nanoparticle surface can also be analysed from the "fingerprint" in lead deposition/stripping experiments. The method is tested through the study of gold nanoparticles deposited on a glassy carbon substrate by the seed-mediated growth method which enables an easy control of the nanoparticle size. The results are in

satisfactory agreement with those obtained *via* scanning electron microscopy (SEM). This is detailed in section 4.2.

SEM images in section 4.1 and section 4.2 were obtained by Mr. Chris Salter and Prof. Alison Crossley. Dr. Eduardo Laborda helped with the data interpretation.

4.1 The Surface Oxidation of Gold Nanoparticle Supported on a Glassy Carbon Electrode in Sulphuric Acid Medium: Contrasts With the Behaviour of 'Macro' Gold

4.1.1 Introduction

The surface structure of noble metals, such as gold and platinum, plays a fundamental role in electrocatalytic reactions with applications in (bio)sensors and energy storage and generation. Consequently, extensive efforts have been devoted to investigate and understand the effect of the surface morphology and composition of noble metals on the kinetics and mechanism of electron transfer reactions, with particular attention to the oxidation of the surface [1–14]. In the case of gold, the details of electro-oxidation in acid media have been investigated in depth [11, 12, 15, 16]. The

following three-step mechanism is widely accepted in the literature:

$$\mathrm{Au(H_2O)}_{ads} \rightarrow \mathrm{AuOH} + \mathrm{H^+} + e^- \tag{4.1}$$

$$\mathrm{AuOH} \rightarrow \mathrm{AuO} + \mathrm{H^+} + e^- \tag{4.2}$$

$$\mathrm{AuO} + \mathrm{H_2O} \rightarrow \mathrm{OAu(H_2O)}_{ads} \tag{4.3}$$

Through studies using the quartz crystal microbalance (QCMB) technique it has been confirmed that the first step of gold surface oxidation in the presence of oxygen-species in solution yields a Au-OH monolayer [9, 10] as a result of OH deposition with desorption of the chemisorbed anions present. Conway [12, 16] suggested that the oxidation product in the second electron transfer process is written in terms of AuO, which represent states of chemical occupancy of the lattice rather than stoichiometric phase compounds. DFT calculations [17] suggest the formation of a linear O-Au-O structure. Steps 4.1 and 4.2 are followed by the place exchange (or turnover) of surface atoms (accompanied by water adsorption) due to repulsive interactions of the metal-oxygen dipoles: step (4.3) [9, 12, 16].

On the basis that in the reductive scan the oxide species are reduced back to gold, repetitive cycling enables the gold surface to be refreshed and indeed this procedure is extensively used to clean gold surfaces in nitrogen-saturated sulphuric solution with cycling in the potential range between 0 and 1.5 V (vs. SCE) [18–20]. With the purpose of cleaning the surface, higher potentials should be avoided

since surface reconstruction and roughness are promoted [10, 21]. This method has also been used to clean the surface of gold nanoparticles under the assumption that their behaviour is the same as the bulk material [22, 23]. However, this procedure is open to question due to the changed electronic and morphological properties of metal clusters. Thus, this section aims to investigate the behaviour of the electro-oxidation of gold nanoparticles in sulphuric acid medium compared to bulk gold.

4.1.2 Results and Discussion

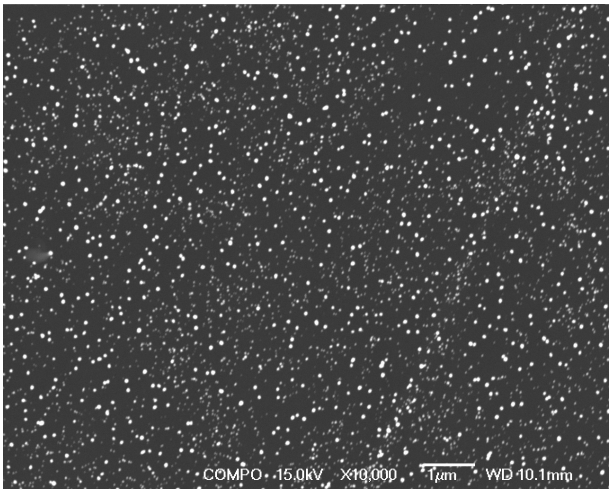


Figure 4.1: SEM images of Au-NPs/GCE. Electro-deposition conditions: 0.5 mM Au^{3+}; seeding step: E_1 = - 1.40 V, 0.1 s; growing step: E_2 = 0.68 V, 30s

Double-pulse chronoamperometry was applied in this work to electrodeposit gold nanoparticles on a glassy carbon macroelectrode (Au-NPs/GCE)[24–26]. The modification was carried out in N_2-saturated 0.50 M sulphuric acid containing 0.5 mM Au^{3+} solution and a first 'seeding' potential of -1.40 V (vs. SCE) was applied followed by a 'growing' potential pulse at 0.68 V under a positive nitrogen pressure.

Scanning electron microscopy (SEM) images (Figure 4.1) of the modified electrodes were analyzed with Image J software (public software, NIH), which show that the nanoparticles are evenly distributed on the glassy carbon surface, with an average size of 40 ± 10 nm and the coverage of 10 %. A gold macroelectrode of radius 1 mm was polished prior to experiments on alumina lapping compounds (Buehler, USA) of decreasing size (1.0, 0.3, 0.05 m) and sonicated in an ultrasound bath prior to use.

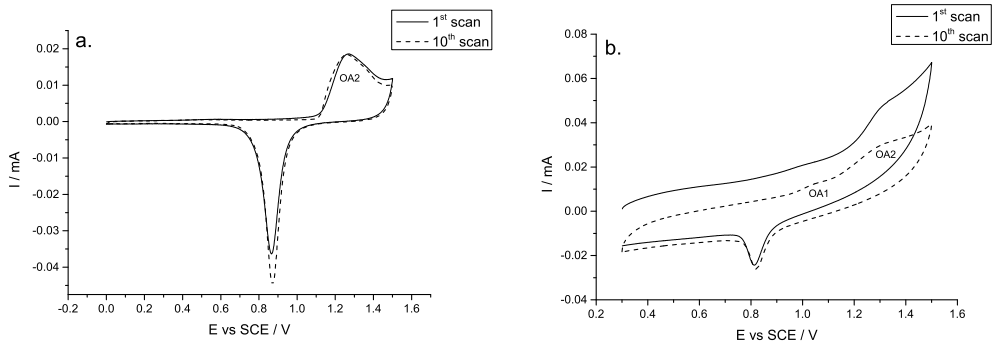


Figure 4.2: 1st (solid line) and 10th (dashed line) scans corresponding to the electro-oxidation and reduction of the gold surface in nitrogen saturated 0.50 M sulphuric acid on the gold macroelectrode (a) and the gold nanoparticle-modified glassy carbon electrode (Au-NPs/GCE) (b). The potential was scanned between 0.0 V and 1.50 (vs. SCE) at a scan rate of 100 mVs^1.

Figure 4.2 shows the electro-oxidation 'fingerprints' of the polycrystalline gold macroelectrode and Au-NPs/GCE in N_2-saturated 0.50 M sulphuric acid solution corresponding to the 1st and 10th scans between 0.0 V and 1.50 V (vs. SCE). With the polycrystalline macrogold electrode (Figure 4.2.a) the main oxidation peak OA2 (following the nomenclature proposed by Angerstein-Kozlowska and Conway) [16] is situated at ca. 1.3 V and it relates to the formation of $OAu(H_2O)_{ads}$ and AuO according to steps 4.1 - 4.3 [9]. A peak at similar potentials is observed

with the Au-NPs/GCE electrode along with a second peak (OA1) that arises at ca. 1.05 V and which is not observed on the macroelectrode either in the 1st or 10th scans. Moreover, OA1 increases while OA2 decreases with successive scans on nanoparticles. The increase of OA1 may be due to the reconstruction process accompanying the electrooxidation process [12, 16] In the literature, OA1 has been associated with the electrodeposition of OH and O species on anion-free areas of the gold surface [13, 16] and later works have pointed out that the magnitude of this peak is directly related to the density of surface defects [2, 27].

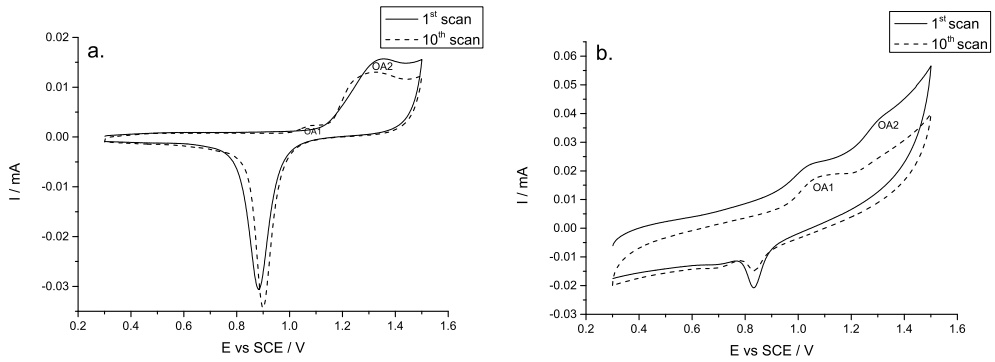


Figure 4.3: 1st (solid line) and 10th (dashed line) scans corresponding to the electrooxidation and reduction of the gold surface in oxygen saturated 0.50 M sulphuric acid on the gold macroelectrode (a) and the gold nanoparticle-modified glassy carbon electrode (Au-NPs/GCE) (b). The potential was scanned between 0.30 V and 1.50 V (vs. SCE) at a scan rate of 100 mVs^{-1}.

HSO_4^- and SO_4^{2-} species adsorb strongly on the gold surface, which affects significantly the OH/O deposition. Thus, competitive adsorption between sulphate ions and OH/O species in the solution blocks the early stage of surface oxidation that is displaced positively [28, 29]. Adsorbed HSO_4^- and SO_4^{2-} also have repulsive interactions with the metal-oxygen dipoles, which destabilize electrodeposited

OH/O species and lead to surface reconstruction [30]. Therefore, under conditions where the deposition of oxygen species is promoted versus the adsorption of anions, peak OA1 is expected to be more apparent, as reported by Angerstein-Kozlowska and Conway when studying the process in the presence of less adsorbing perchlorate anions [16]. Thus, control experiments were carried out where the surface of the gold macroelectrode and nanoparticles was electro-oxidized in O_2-saturated H_2SO_4 solution. Figure 4.3 shows the results obtained for the 1st and 10th scans between 0.3 and 1.5 V (vs. SCE). Note that less positive potentials have been avoided since oxygen electroreduction gives rise to intermediates that accumulate on the gold surface and introduces new variables in the study. As can be seen in Figure 4.3.b, as a result of the saturation of the solution with oxygen, the OA1 peak increases significantly in the case of nanoparticles whereas it is still missing in the first scan of the macroelectrode (see Figure 4.3.a). Only after ten scans is the peak OA1 visible at the macroscale.

Kolb et al. [2, 27] found a correlation between the magnitude of the OA1 peak and the density of surface defects, where gold oxidation takes place at less positive potentials. Indeed, this peak is more apparent as the density of defects increases. According to Angerstein-Kozlowska and Conway's results [16], the availability of these sites seems to be influenced by the absorptivity of other species in the solution, and particularly by the electrolyte anions. Accordingly, the peak is more apparent when the adsorption of oxygen species is enhanced as shown above. Bearing in mind these conclusions, the magnitude of the peak OA1 can be considered as an indicator

of the density of defects on gold surfaces and, consequently, the results obtained in this study indicate that this is higher on the electrodeposited nanoparticles than on the gold macroelectrode.

The oxidative-reductive potential cycling of the gold electrode in acid media is also a widely-used method for cleaning the electrode surface. Given that the results presented above suggest a different behaviour of gold electro-oxidation at the nanoscale, the efficiency of this cleaning procedure in the case of gold nanoparticles has also been examined in this work. For the detection of possible surface changes, the oxygen reduction reaction (ORR) has been considered given that it is a well-known surface-sensitive process.

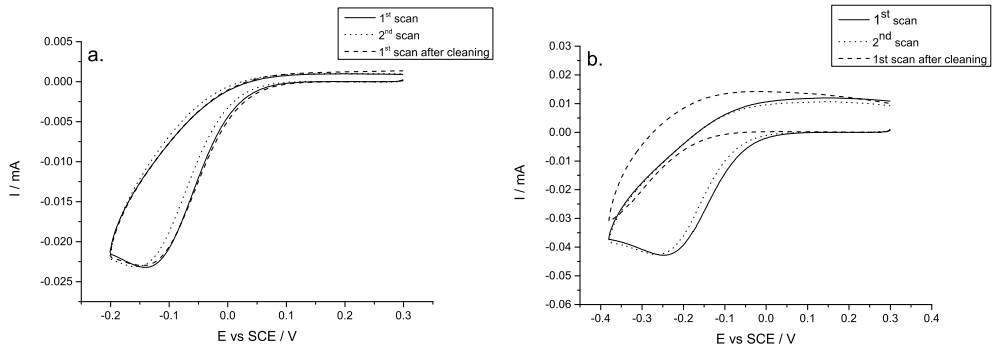


Figure 4.4: Cyclic voltammograms corresponding to oxygen electroreduction on the gold macroelectrode (a) and Au-NPs/GCE (b) in oxygen saturated 0.50 M sulphuric acid solution before (solid and dotted lines) and after (dashed line) cleaning by cycling in N_2-saturated solution, 0.50 M sulphuric acid. v = 100 mVs^{-1}.

Both on gold macroelectrodes and gold nanoparticles there is a shift of the ORR voltammograms towards more negative potentials in successive scans in oxygen saturated 0.50 M sulphuric acid solution as can be observed in Figure 4.4 when comparing the first and second scans for ORR. This can be explained by surface poisoning

due to species generated during the oxygen electroreduction. For the efficient application of gold as a catalyst for the ORR, especially for mechanistic studies of this reaction, it is essential to find a procedure for the regeneration of the electrode surface, the electrochemical cleaning in N_2-saturated sulphuric acid medium being one of the possibilities. As can be observed in Figure 4.4.a, the signal on the macroelectrode is recovered after 10 cycles in 0.5 M N_2-saturated sulphuric acid solution which confirms the efficiency of the cleaning process. However, when applying the same procedure to the AuNPs/GCE (Figure 4.4.b) the ORR signal is not recovered after the cycling treatment. In contrast, this 'cleaning' procedure has a negative effect and the ORR voltammogram shifts towards more negative potentials (higher overpotential).

Several reasons can be considered to explain the failure of the cleaning procedure. Differences can exist between the macro- and nano-scales in the nature of the poisoning of the gold surface as a consequence of different interactions between the accumulating species and surface atoms. However, taking into account the behaviour observed in Figure 4.4.b, 'damaging' effects of cycling in sulphuric acid on the gold NP-modified electrode can take place as a consequence of the rearrangement of surface atoms upon gold electro-oxidation (step 4.3) and/or the possible dissolution of gold from the glassy carbon surface. Indeed, under low pH conditions gold dissolution during the cycling electro-oxidation reduction treatment has been detected [7, 31]. However, in our experiments the charge of the peak corresponding to the reduction of the gold oxide species is approximately constant over the cleaning

procedure, such that one can conclude that the loss of gold is not significant under these conditions. Accordingly, the behaviour of the ORR signal may be assigned to changes in the surface morphology and/or composition of the nanoparticles during the cycling treatment.

In this section, the electro-oxidation behaviour of gold nanoparticles has been investigated showing the contrast in 'macro' and 'nano' scales. The major difference between the 'fingerprints' of bulk gold and gold nanoparticles is the magnitude of the electro-oxidation peak OA1 that has previously been related to the density of surface defects and competitive adsorption between anions and oxygen species in solution. The results obtained here show that the OA1 peak is more apparent in the case of 40 nm electrodeposited nanoparticles. On the other hand this peak is not significant at the gold macroelectrode even in O_2-saturated medium. This is connected with the higher density of surface defects of nanoparticles compared to bulk gold.

4.1.3 Conclusions

Unlike with gold macroelectrodes, the electrooxidation-reduction cycling of nanoparticles in N_2-saturated 0.5 M sulphuric acid is found to have a negative effect on the surface of gold nanoparticles. This can be related to a different nature of the surface poisoning and also to the reconstruction of the nanoparticle surface that accompanies the gold electro-oxidation. Consequently, determination of surface area for Au-NPs/GCE using electro-oxidation in H_2SO_4 is not employed in this thesis.

4.2 Facile in Situ Characterization of Gold Nanoparticle on Electrode Surfaces by Electrochemical Techniques: Average Size, Number Density and Morphology Determination

4.2.1 Introduction

The particular surface and electronic features of nanosized materials are very advantageous in many scientific fields such as electroanalysis [32, 33], catalysis [34, 35], medicine[36], and material science [37]. The synthesis and characterization of nanoparticles are two essential aspects in any study given that their reactivity and properties are defined by their composition, size and morphology. Scanning electron microscopy (SEM) [38–41], transmission electron microscopy (TEM) [28, 42], atomic force microscopy (AFM) [43], scanning tunnelling microscopy (STM) and X-ray diffraction(XRD) [44] are usually employed for the characterization of nanoparticles. However, these techniques have some limitations which are particularly unfavourable when examining nanoparticle-modified electrodes. Thus, the inefficiency in cost and time and the sample preparation restrictions prevent the analysis of modified electrodes immediately before or after each experiment. Moreover, the results obtained may not be representative of the whole sample.

The aim of this section is to find a simple and time-efficient *in situ* character-

ization method for nanoparticles on electrode surfaces. The approach proposed is based on routine electrochemical experiments that can be carried out in any electrochemistry laboratory. This enables the estimation of average values of the size and number of gold nanoparticles together with the different surface sites [45]. The particles are deposited on a glassy carbon electrode and a value for the total gold surface area is extracted from the charge associated with lead underpotential deposition on gold [46]. The voltammograms corresponding to lead deposition and stripping also informs about the surface sites on the nanoparticle. Next, the total amount of gold is obtained from its anodic stripping in hydrochloric acid medium [47]. From the values of the total surface area and amount of gold, the average size of the gold particles can be easily calculated.

The suitability of the electrochemical characterization procedure is tested by comparison with the results obtained in SEM for a glassy carbon electrode modified with gold nanoparticles of different size via seed-mediated growth method [28, 42, 44, 48–50]. The methodology is also applied to the study of supplied gold nanoparticles with satisfactory results.

4.2.2 Experimental

4.2.2.1 Chemical Reagents

Sodium borohydride (98 %, $NaBH_4$), gold(III) chloride trihydrate(>99 %, $HAuCl_4{\cdot}3H_2O$), trisodium citrate (>99.0 %), hexadecyltrimethylammonium bro-

mide (CTAB), hydrochloric acid (37 %,HCl),L-ascorbic acid (>99.0 %), sodium hydroxide (>97 %,NaOH) and lead(II) nitrate (>99.5 %, $Pb(NO_3)_2$) were all purchased from Sigma-Aldrich and used as received without further purification. Citrate-capped gold nanoparticles were provided by Mintek (Randburg, South Africa). All the solutions were prepared using deionised water with a resistivity 18.2 MΩ (25°C).

4.2.2.2 Instrumental

Electrochemical experiments were performed using a three-electrode system with an Autolab PGStat 20 computer-controlled potentiostat (Eco-Chemie, Utrecht, Netherlands). Platinum wire was employed as counter electrode and the reference electrode was an saturated calomel electrode (SCE, Radiometer, Copenhagen). A bare or modified glassy carbon (GC) electrode (3 mm diameter, BAS, Technical, UK) was used as working electrode. The GC electrode was polished before use with diamond paste(Kent, UK) of decreasing size (3.0, 1.0 and 0.1 mm) and sonicated in ultrasound bath. Scanning electron microscope (SEM) images were obtained on a JEOL 6500F FEGSEM by Mr. Chris Salter and Prof. Alison Crossley. All the electrochemistry experiments were carried out in 298 K.

4.2.2.3 Electrode Modification with Gold Nanoparticles

Seed-mediated growth method was used to modify a glassy carbon electrode [28, 42, 44, 48–50]. The polished GC electrode was immersed in the gold seeding solution containing 18 mL water, 0.5 mL (0.01 M) trisodium citrate, 0.5 mL $HAuCl_4$ (0.01

M) and 0.5 mL freshly prepared ice-cold $NaBH_4$ (0.10 M). After immersing in the seeding solution for 30 minutes, the electrode was sequentially rinsed by water and dried with nitrogen. Then the seeded electrode was immersed in the growth solution containing 18 mL CTAB (0.10 M), 0.5 mL $HAuCl_4$ (0.01 M) and 0.1 mL ascorbic acid (0.10 M) solutions for 2, 10 and 30 min to reach different degrees of coverage. The use of longer growing times was avoided since it resulted in a higher degree of agglomeration of particles which compromised the accuracy of the characterization method here presented. The modified electrode was rinsed thoroughly with deionized water and dried under nitrogen atmosphere before electrochemical experiments.

4.2.2.4 Electrochemical Characterization

The modified electrode was first immersed into 1 mM $Pb(NO_3)_2$, 0.1 M NaOH solution to run cyclic voltammetry at 50 $mV{\cdot}s^{-1}$ in the range of 0.20 to 0.73 V (vs. SCE). After the experiments with lead the modified electrode was rinsed with distilled water and transferred into 0.1 M HCl. Stripping experiments in hydrochloric acid were carried out by scanning between 0.70 and 1.30 V (vs. SCE). All the solutions were deoxygenated by purging with nitrogen gas for about 30 minutes and the experiments were carried out under N_2 atmosphere.

4.2.3 Results and Discussion

4.2.3.1 Electrochemical Characterization

Underpotential deposition (UPD) of metals as well as adsorption/desorption processes are surface-sensitive and they enable selective examination of the characteristics of metal substrates. In the case of gold surfaces, electro-oxidation in 0.5 M sulphuric acid medium is a commonly used approach for the determination of the surface area by integration of the cathodic peak [43]. However, as discussed in section 4.1, the use of this method for quantitative analysis is inappropriate given that the gold oxide growth is a function of the number of scans as a result of the formation of monolayer and multilayer oxidized products [21, 51, 52]. This effect was found in preliminary experiments of this work such that the reduction peak shifts towards less positive potentials in successive scans as reported in the literature [21].

Underpotential deposition is well known to be highly sensitive to the surface structure of the electrode, the process being dependent on the particular interactions between the surface and the depositing atoms [53]. Hernandez et al. [46] have proved lead UPD in alkaline solution to be a suitable system for the estimation of the surface area and surface structure of gold nanoparticles (NPs). Thus, lead forms a layer on gold surface at a slightly positive potential than bulk lead deposition [54] which is dissolved at different potentials depending on the facets of the gold nanocrystals. As shown below, the voltammograms corresponding to the lead deposition/stripping on gold provide better accuracy and reproducibility as well as further insights into the

gold surface sites.

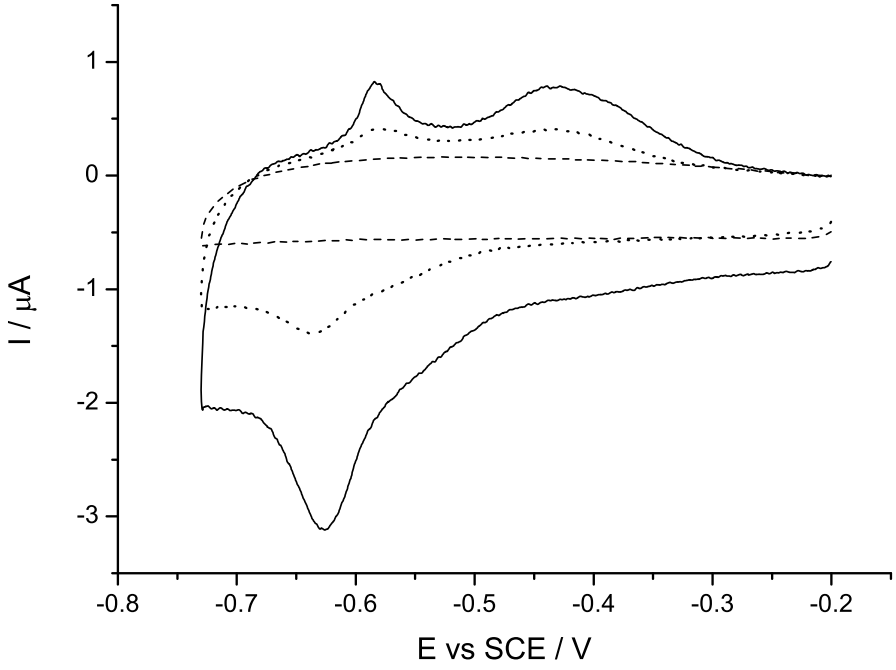


Figure 4.5: Comparison of the cyclic voltammogram corresponding to lead deposition on bare GC electrode (dashed line) and gold nanoparticles-modified GC electrode with 2 min (dotted line) and 30 min (solid line) growing time in 1 mM $Pb(NO_3)_2$ and 0.1 M NaOH solution. Scan rate: 50 $mV{\cdot}s^{-1}$.

The voltammetric profiles of bare and gold nanoparticle-modified (Au/GCE) glassy carbon electrodes in 1 mM $Pb(NO_3)_2$, 0.1 M NaOH solution are shown in Figure 4.5. Whereas no signal is observed on the bare GC(dashed line), the peaks corresponding to the deposition and subsequent stripping of lead are recorded after the modification with gold nanoparticles. In the seed-mediated growth method employed here the size of the nanoparticles (and so the total surface area) can be increased by immersing the seeded electrode in the growing solution for longer pe-

riods of time. Figure 4.5 shows the "fingerprint" in lead solution corresponding to 2 min(dotted line) and 30 min (solid line) growing time, the charge of lead deposition/stripping clearly increasing with the length of the growing step.

From the results obtained with single-crystal electrodes [46] it is known that Au(111), Au(100) and Au(110) have well-defined deposition/stripping peaks at different potentials. Thus, structural information is available along with the quantitative determination of the surface area of nanoparticles. The sharp stripping peak at -0.58 V (vs. SCE) in Figure 4.5 is associated with the Au(111) domain and a lead UPD charge of 380 μC·cm^{-2} [46, 54]. Au(110) facet contributes to the broader stripping peak at -0.38 V (vs. SCE) with a deposition charge associated of 330 μC·cm^{-2} [46]. No relevant contribution of (100) domains is observed in the voltammograms shown in Figure 4.5. Therefore, additionally to the determination of the gold surface area, lead UPD peaks enable us to identify the different surface sites on the NP surface and their relative areas. This is connected to the size and shape of the nanoparticles and it is essential to evaluate their suitability for a given application.

The quantification of the amount of gold deposited on the glassy carbon surface has been carried out by anodic stripping of the nanoparticles in 0.1 M hydrochloric acid [47]. According to studies on macro gold electrodes [29, 55] the resulting species are the complexes $AuCl_2^-$ and $AuCl_4^-$ according to the following equilibria [29, 47, 55]:

$$Au + 4Cl^- \leftrightarrows AuCl_4^- + 3e^- \tag{4.4}$$

$$AuCl_4^- + 2Au + 2Cl^- \leftrightarrows 3AuCl_2^- \tag{4.5}$$

Recent work in our group has extended the study to nanogold [47], the results showing that the charge of the stripping is quantitatively related to the loading of gold nanoparticles with a value of 1.9 ± 0.1 electrons transferred per gold atom. Thus, the electro-oxidation of gold nanoparticles was carried out via cyclic voltammetry in the potential range 0.70 - 1.30 V (vs. SCE). As can be observed in Figure 4.6.a, no signal is recorded on bare glassy carbon electrode(dashed line) which confirms that the stripping charge is all due to gold nanoparticles. After several scans (typically 3 scans, see Figure 4.6.b) the gold deposit is completely removed and the charge under the peaks enables the calculation of the total amount of gold deposited on the glassy carbon surface.

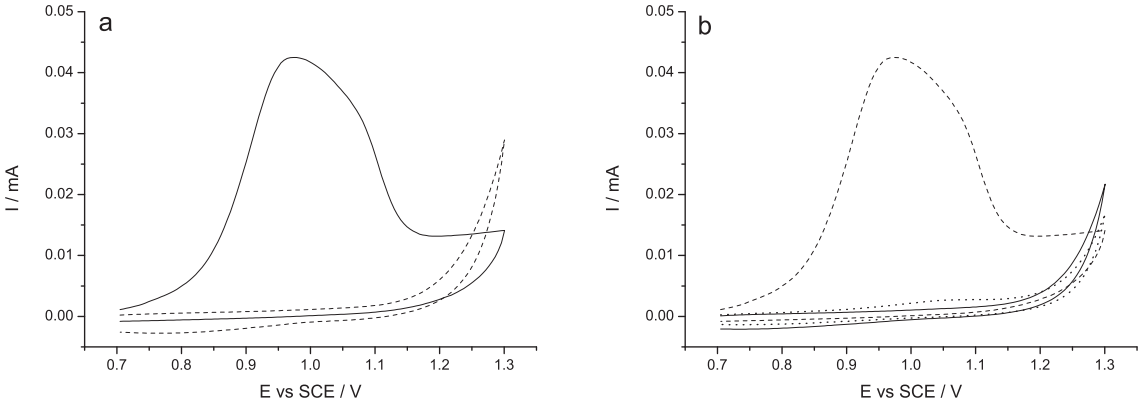


Figure 4.6: (a) Comparison of cyclic voltammograms obtained with gold nanoparticle-modified GC electrode(solid line) and bare GC electrode(dashed line) in 0.1 M HCl. Scan rate: 100 $mV \cdot s^{-1}$. (b) Successive cyclic voltammograms,1st scan (dashed line), 2nd scan (dotted line), 3rd scan (solid line), obtained with gold nanoparticle-modified GC electrodes in 0.1 M HCl. Scan rates: 100 $mV \cdot s^{-1}$.

By combining the values of the surface area (S) determined by lead UPD and the

amount of gold (Q) from anodic stripping in HCl the radius and number of nanoparticles on the GC electrode can be easily calculated from the following relationships:

$$\mathrm{S} = x\pi \mathrm{r}^2 \times \mathrm{N} \tag{4.6}$$

$$\mathrm{Q} = 1.9 \times \mathrm{e} \times \frac{\frac{x}{3}\pi r^3 \rho_{Au}}{M_{Au}} \times \mathrm{N_A} \times \mathrm{N} \tag{4.7}$$

where x = 2 for hemispherical and x = 4 for spherical nanoparticles, e is the electronic charge, r is the average radius of the nanoparticles, N is the number of particles,ρ_{Au} is the density of gold, M_{Au} is the molar mass of gold and $\mathrm{N_A}$ is the Avogadro constant.

Thus, from the ratio Q/S the radius of the nanoparticles can be determined:

$$\mathrm{r} = \frac{3\mathrm{M_{Au}}}{1.9\mathrm{e}\rho_{Au}\mathrm{N_A}} \times \frac{Q}{S} \tag{4.8}$$

Once the radius is known, the number of particles can be extracted from Eq. 4.6 or 4.7.

Following the above procedure the characteristics of the nanoparticles at the modified GC electrode have been examined for different growing times. The results are shown in Table 4.1. As expected, the values obtained for the diameter of the particles gradually increase with the growing time from ca.20 nm for 2 min growing time up to ca.40 nm for 30 min. Assuming a hemispherical shape for the particles, the mean value for the number of particles obtained is $(4 \pm 2)\times10^8$ NPs, which yields a value of particle density of ca. $(6 \pm 3)\times10^9$ NP·cm^{-2}.

Table 4.1: Values of the diameter (d) and number (N) of gold nanoparticles obtained through electrochemical characterization (i.e., lead deposition and stripping in HCl solution). Different growing times in the modification of the electrode are considered.

Growing time/min	d/nm	N/(10^8 particles)
2	23 ± 2	
10	32 ± 7	4 ± 2
30	39 ± 3	

4.2.3.2 Scanning Electron Microscope (SEM) Results

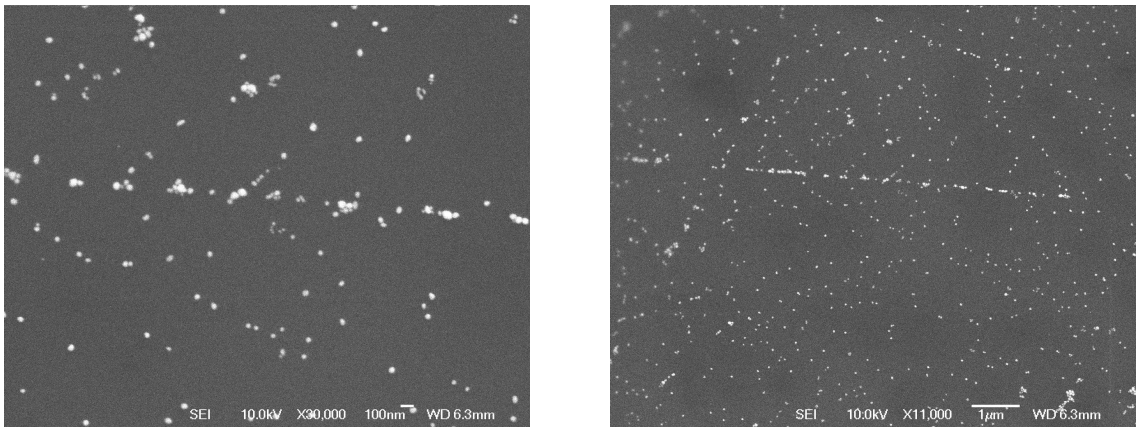


Figure 4.7: Scanning electron microscopy images of a glassy carbon surface modified with gold nanoparticles by seed-mediated growth method with a growing time of 30 min.

Scanning electron microscope (SEM) images of the surface of the modified GC electrodes were also obtained in order to evaluate the size and distribution of the nanoparticles and test the suitability of the electrochemical approach presented in section 4.2.3.1. SEM images of Au-NPs/GCE electrodes after growing times of 30 min are shown in Figure 4.7. As can be observed, gold nanoparticles have a spherical shape, with an average size of ca. 40 nm diameter, which agrees very well with the

results obtained with the electrochemical approach.

4.2.3.3 Application to Supplied Gold Nanoparticles

The electrochemical characterization method has also been tested by characterizing supplied nanoparticles (Mintek,Randburg, South Africa). The glassy carbon electrode was modified with 5 mL gold nanoparticles by the drop-casting method. The electrochemical characterization approach yields an average diameter of ca. 22 nm. These results are in good agreement with those obtained by SEM and anodic particle coulometry which yielded a diameter of 20 nm and 21 nm, respectively [47].

4.2.4 Conclusions

A simple electrochemical methodology has been developed for *in situ* characterization of gold nanoparticles. This can complement typically used imaging techniques since it provides faster and more representative results.

Gold nanoparticles under study are deposited on a glassy carbon electrode. First, the total surface area and structure of the particles are estimated from underpotential deposition of lead in alkaline medium. Next, the amount of gold is determined from the charge associated with the anodic stripping of gold in hydrochloric acid solution. Both measurements enable the extraction of the average size and number of nanoparticles as well as the estimation of the different surface sites.

The suitability of the method has been confirmed by examining glassy carbon electrodes modified with gold nanoparticles of different size by seed-mediated growth

method. The results obtained with the electrochemical approach agree well with those derived from scanning electron microscopy. The new characterization procedure has also been applied to the study of supplied nanoparticles.

Bibliography

[1] O. Magnussen, J. Wiechers and R. Behm, *Surface Science* **289** (1993) 139–151.

[2] M. Schneeweiss and D. Kolb, *Solid State Ionics* **94** (1997) 171–179.

[3] M. A. Schneeweiss, D. M. Kolb, D. Liu and D. Mandler, *Canadian Journal of Chemistry* **75** (1997) 1703–1709.

[4] A. Dakkouri, *Solid State Ionics* **94** (1997) 99–114.

[5] R. Nichols, O. Magnussen, J. Hotlos, T. Twomey, R. Behm and D. Kolb, *Journal of Electroanalytical Chemistry and Interfacial Electrochemistry* **290** (1990) 21–31.

[6] A. Hamelin, *Journal of Electroanalytical Chemistry* **407** (1996) 1–11.

[7] D. Kolb, *Electrochimica Acta* **45** (2000) 2387–2402.

[8] G. Liu, E. Luais and J. J. Gooding, *Langmuir* **27** (2011) 4176–4183.

[9] C. Shengli, W. Bingliang and Z. Hong, *Wuhan University Journal of Natural Sciences* **3** (1998) 102–107.

[10] S. Xia and V. Birss, *Journal of Electroanalytical Chemistry* **500** (2001) 562–573.

[11] C. Xiang, A. G. Güell, M. A. Brown, J. Y. Kim, J. C. Hemminger and R. M. Penner, *Nano Letters* **8** (2008) 3017–3022.

[12] H. Angerstein-Kozlowska, B. Conway, A. Hamelin and L. Stoicoviciu, *Journal of Electroanalytical Chemistry and Interfacial Electrochemistry* **228** (1987) 429–453.

[13] R. Adžić, S. Strbac and N. Anastasijević, *Materials Chemistry and Physics* **22** (1989) 349–375.

[14] B. Conway, *Progress in Surface Science* **49** (1995) 331–452.

[15] S. Bruckenstein and M. Shay, *Journal of Electroanalytical Chemistry and Interfacial Electrochemistry* **188** (1985) 131–136.

[16] H. Angerstein-Kozlowska, B. Conway, A. Hamelin and L. Stoicoviciu, *Electrochimica Acta* **31** (1986) 1051–1061.

[17] K. Sun, M. Kohyama, S. Tanaka and S. Takeda, *Journal of Physical Chemistry A* **116** (2012) 9568–9573.

[18] L. M. Fischer, M. Tenje, A. R. Heiskanen, N. Masuda, J. Castillo, A. Bentien, J. Émneus, M. H. Jakobsen and A. Boisen, *Microelectronic Engineering* **86** (2009) 1282–1285.

[19] C. Spegel, A. Heiskanen, J. Acklid, A. Wolff, R. Taboryski, J. Emnéus and T. Ruzgas, *Electroanalysis* **19** (2007) 263–271.

[20] M. F. M. Noh and I. E. Tothill, *Analytical and Bioanalytical Chemistry* **386** (2006) 2095–2106.

[21] G. Tremiliosi-Filho, L. DallAntonia and G. Jerkiewicz, *Journal of Electroanalytical Chemistry* **578** (2005) 1–8.

[22] M. S. El-Deab, T. Sotomura and T. Ohsaka, *Electrochemistry Communications* **7** (2005) 29–34.

[23] H. Xu, L. Zeng, S. Xing, G. Shi, Y. Xian and L. Jin, *Electrochemistry Communications* **10** (2008) 1839–1843.

[24] M. Ueda, H. Dietz, A. Anders, H. Kneppe, A. Meixner and W. Plieth, *Electrochimica Acta* **48** (2002) 377–386.

[25] E. Sheridan, J. Hjelm and R. J. Forster, *Journal of Electroanalytical Chemistry* **608** (2007) 1–7.

[26] J. Hoogvliet, M. Dijksma, B. Kamp and W. Van Bennekom, *Analytical Chemistry* **72** (2000) 2016–2021.

[27] G. Sandmann, H. Dietz and W. Plieth, *Journal of Electroanalytical Chemistry* **491** (2000) 78–86.

[28] N. R. Jana, L. Gearheart and C. J. Murphy, *Journal of Physical Chemistry B* **105** (2001) 4065–4067.

[29] M. A. Diaz, G. Kelsall and N. Welham, *Journal of Electroanalytical Chemistry* **361** (1993) 25–38.

[30] H. Angerstein-Kozlowska, B. Conway, B. Barnett and J. Mozota, *Journal of Electroanalytical Chemistry and Interfacial Electrochemistry* **100** (1979) 417–446.

[31] S. Cadle and S. Bruckenstein, *Analytical Chemistry* **46** (1974) 16–20.

[32] S. Vaddiraju, I. Tomazos, D. J. Burgess, F. C. Jain and F. Papadimitrakopoulos, *Biosensors and Bioelectronics* **25** (2010) 1553 – 1565.

[33] F. Campbell and R. G. Compton, *Analytical and Bioanalytical Chemistry* **396** (2010) 241–259.

[34] A. Corma and H. Garcia, *Supported Gold Nanoparticles as Oxidation Catalysts*, 389–426 (Wiley-VCH Verlag GmbH & Co. KGaA, 2008).

[35] M. T. M. Koper, *Nanoscale* **3** (2011) 2054–2073.

[36] D. Akin, *ChemMedChem* **2** (2007) 1534–1535.

[37] O. D. Velev and S. Gupta, *Advanced Materials* **21** (2009) 1897–1905.

[38] J. Zhang, M. Kambayashi and M. Oyama, *Electrochemistry Communications* **6** (2004) 683 – 688.

[39] T. Horibe, J. Zhang and M. Oyama, *Electroanalysis* **19** (2007) 847– 852.

[40] M. Oyama, S.-y. Yamaguchi and J. Zhang, *Analytical Sciences* **25** (2009) 249–253.

[41] M. S. El-Deab, T. Sotomura and T. Ohsaka, *Journal of the Electrochemical Society* **152** (2005) C1–C6.

[42] T. K. Sau and C. J. Murphy, *Journal of the American Chemical Society* **126** (2004) 8648–8649.

[43] X. Dai, O. Nekrassova, M. E. Hyde and R. G. Compton, *Analytical Chemistry* **76** (2004) 5924–5929.

[44] N. R. Jana, L. Gearheart and C. J. Murphy, *Langmuir* **17** (2001) 6782–6786.

[45] J. Solla-Gullón, P. Rodríguez, E. Herrero, A. Aldaz and J. M. Feliu, *Physical Chemistry Chemical Physics* **10** (2008) 1359–1373.

[46] J. Hernandez, J. Solla-Gullon and E. Herrero, *Journal of Electroanalytical Chemistry* **574** (2004) 185–196.

[47] Y.-G. Zhou, N. V. Rees, J. Pillay, R. Tshikhudo, S. Vilakazi and R. G. Compton, *Chemmical Communications* **48** (2011) 224–226.

[48] M. Oyama, *Analytical Sciences* **26** (2010) 1–12.

[49] C. J. Murphy and N. R. Jana, *Advanced Materials* **14** (2002) 80.

[50] Y. Cui, C. Yang, W. Zeng, M. Oyama and W. Pu, *Analytical Sciences* **23** (2007) 1421–1425.

[51] H. Angerstein-Kozlowska, B. Conway, A. Hamelin and L. Stoicoviciu, *Journal of Electroanalytical Chemistry and Interfacial Electrochemistry* **228** (1987) 429–453.

[52] L. Burke and P. Nugent, *Gold Bulletin* **30** (1997) 43–53.

[53] E. Herrero, L. J. Buller and H. D. Abruna, *Chemical Reviews* **101** (2001) 1897–1930.

[54] M. O. Finot, G. D. Braybrook and M. T. McDermott, *Journal of Electroanalytical Chemistry* **466** (1999) 234–241.

[55] A. Kolics, A. E. Thomas and A. Wieckowski, *Journal of the Chemical Society, Faraday Transactions* **92** (1996) 3727–3736.

Chapter 5

A Joint Experimental and Computational Search for Authentic Nano-electrocatalytic Effects: Electrooxidation of Nitrite and L-Ascorbate on Gold Nanoparticle-Modified Glassy Carbon Electrodes

In this chapter, section 5.1 introduces mechanistic studies of the electro-oxidation of the nitrite anion in aqueous media on different electrode materials. The voltammetric analytical determination of nitrite is in principle a very competitive method by virtue of being fast, easy to apply, economical and portable. In order to optimize the experimental conditions for the analytical determination it is essential to understand the reaction scheme and kinetics of the redox system. For this purpose square wave voltammetry is employed to examine the electro-oxidation of nitrite. The reaction mechanism and electrode kinetics are investigated, pointing out the effects of the solution pH, the electrode material (glassy carbon, edge plane pyrolytic graphite and gold) and the supporting electrolyte. A second order catalytic mechanism is suggested by the experimental results, with the nitrite being regenerated by disproportionation of the electrogenerated NO_2 with a rate constant $k_{disp} = (2.0 \pm 0.1) \times 10^6\ M^{-1} \cdot s^{-1}$. The electrode reaction is found to be reversible on gold macroelectrodes and much slower on carbon based electrodes with a blocking effect due to the presence of perchlorate anions.

The simulation program used in section 5.1 for square wave voltammetry was written and debugged by Dr. Eduardo Laborda. Work related with this section has been published in the Journal of Electroanalytical Chemistry, [1].

In section 5.2, the investigation of electrocatalytic nanoeffects is tackled via joint electrochemical measurements and computational simulations. The cyclic voltammetry of electrodes modified with nanoparticles is modelled considering the kinetics of the electrochemical process on the bulk materials of the different regions of the

electrode, that is, the substrate (glassy carbon) and the nanoparticles (gold). Comparison of experimental and theoretical results enables the detection of changes in the electrode kinetics at the nanoscale due to structural and/or electronic effects. This approach is applied to the experimental assessment of electrocatalytic effects by gold nanoparticles (Au-NPs) in the electrooxidation of nitrite and L-ascorbate. In particular, a glassy carbon electrode is modified with Au-NPs via the seed-mediated growth method. Divergence between the kinetics of these processes on gold macroelectrodes and gold nanoparticles is examined. Whereas claimed catalytic effects are not observed in the electrooxidation of nitrite, electrocatalytic nanoeffects are verified in the case of L-ascorbate. This is probably due to that the latter electron transfer process follows an adsorptive mechanism. The combination of simulation with experiments is commended as a general strategy of authentification, or not, of nanoelectrocatalytic effects.

The simulation program in this section was written and debugged by Dr. Kristopher Ward. SEM measurements were carried out by Mr. Chris Salter and Prof. Alison Crossley. Contents based in section 5.2 was published in Small, [2]. Dr. Eduardo Laborda helped with the data interpretation.

5.1 Electrochemical Oxidation of Nitrite: Kinetic, Mechanistic and Analytical Study by Square Wave Voltammetry

5.1.1 Introduction

The determination of the nitrite ion is of fundamental interest due to its potential effects on human health and its widespread presence in food, water and soils [3–6]. These effects include serious problems, for example, leading to carcinogenic compounds in the digestive system or interfering in the oxygen availability for tissues. Therefore, knowledge of nitrite concentration is essential in assessing the quality of food and water.

Many analytical methods have been employed including spectroscopic, chromatographic, electrophoretic and electrochemical methods [7]. The latter have important advantages due to their rapid response, easy use and cheap and portable instrumentation. Among the electrochemical methods, electro-oxidation of nitrite is preferable to electro-reduction where several interferences operate (mainly, nitrate and molecular oxygen) and the understanding of the reaction mechanism involved is more complex.

With the aim of decreasing the overpotential required for the nitrite electro-oxidation, reducing interferences and increasing the analytical sensitivity, electrodes modified with carbon nanotubes, metal nanoparticles, polymeric films, etc. [6] (and

references therein) have been widely employed. The electrode modification may affect the electrode kinetics, the effective surface area and the diffusion regime [8, 9], modifying the magnitude of the signal and the overpotential where this appears. For the effective and rational electrode modification it is necessary to understand the reactions involved in the redox system, as well as the effect of the experimental variables.

In the case of nitrite electro-oxidation, various papers have been devoted to the study of possible reactions coupled to the electrode process, but less attention has been paid to the analysis of the electrode kinetics. This section deals with the mechanistic and kinetic study of the electro-oxidation of nitrite by using square wave voltammetry (SWV). This differential pulse technique has well-known advantages in electroanalysis, such as well-defined peak-shaped response and reduced capacitative effects [10]. SWV can also be very valuable for quantitative kinetic analysis given that the distorting effects are minimized, the voltammograms are peak shaped and they are very sensitive to the electrode kinetics (see below) [8, 11]. This makes the extraction of parameters easier and more accurate.

Thus, we have characterized the reaction mechanism and the electrode kinetics by means of square wave voltammetry through the variation with the frequency of the characteristic parameters of the voltammograms: peak current, peak potential and half-peak width. A second-order catalytic mechanism (Eq. 5.1 and Eq. 5.2) accounts for the experimental results obtained in square wave and cyclic voltammetry under a range of time scales:

$$NO_2^- \overset{k_{ox}}{\rightleftarrows} NO_2 + e^- \tag{5.1}$$

$$2NO_2 + H_2O \overset{k_{disp}}{\rightleftarrows} 2H^+ + NO_3^- + NO_2^- \tag{5.2}$$

The effects of pH, supporting electrolyte and electrode material on the electrode kinetics are discussed.

5.1.2 Experimental

5.1.2.1 Chemical Reagents

Sodium phosphate monobasic dihydrate (>99 %), potassium sulphate (K2SO4, >99 %), sodium sulphate (Na_2SO_4, >99 %), sodium perchlorate monohydrate (NaClO4, >98 %), potassium chloride (KCl, 99.0100.5 %), sodium chloride (NaCl, >99 %), hydrochloric acid (37 %), acetic acid (> 99 %), sodium acetate trihydrate (>99 %), sodium hydroxide (>97 %), sodium phosphate dibasic (>99 %) and sodium nitrite ($NaNO_2$, >99 %) were all purchased from SigmaAldrich and used as received without further purification.

Buffer solutions were prepared as follows: pH 1 - 3: 0.1 - 0.001 M hydrochloric acid; pH 4.6: 0.1 M acetic acid and 0.1 M sodium acetate; pH 6.8: 0.025 M sodium phosphate dibasic and 0.025 M sodium phosphate; pH 9.2: 0.05 M disodium tetraborate; pH $10 - 12$: $0.0001 - 0.01$ M sodium hydroxide.

Experiments on the influence of pH were made in different buffers containing

0.1 M potassium chloride as supporting electrolyte and 1 mM sodium nitrite. Experiments for the kinetic study of the electro-oxidation of nitrite were carried out in solution at pH 4.6, with a constant ionic strength of the supporting electrolyte 0.5 M and 2 mM sodium nitrite. The concentration of nitrite was verified with ultravioletvisible spectroscopy (U-2001 spectrophotometer, HITACHI, UK) at 355 nm (ε_{355} = 23 mol^{-1} dm^3 cm^{-1}) [12]. A precision digital pH meter (PH213 Microprocessor pH meter, HANNA Instruments, UK) was used for pH measurements. Deionised water with 18.2 MΩ cm (25 °C) was used to prepare all the solutions and the temperature was controlled at 20 °C during the experiments.

5.1.2.2 Instrumental

Electrochemical experiments were performed using a three-electrode system with an Autolab PGStat 20 computer-controlled potentiostat (Eco-Chemie, Utrecht, Netherlands). A glassy carbon electrode (GC, 3.0 mm diameter, BAS, Technical, UK), a gold electrode (1.0 mm diameter, BAS, Technical, UK), and edge plane pyrolytic graphite (EPPG, 4.0 mm diameter, BAS, Technical, UK) were used as the working electrodes. A Platinum wire was employed as the counter electrode and the reference electrode was a saturated calomel electrode (SCE, Radiometer, Copenhagen). The GC electrode was polished before use with diamond paste (Kenet, Kent, UK) of decreasing size (3 μm, 1 μm and 0.1 μm). Gold and EPPG electrodes were polished prior to experiments on alumina lapping compounds (BDHS) of decreasing sizes (10.3 μm). All of them were sonicated in an ultrasound bath prior to use. All the

electrochemistry experiments were carried out at 298 K.

5.1.2.3 Simulation Details

The simulation of the electrochemical experiments has been carried out with the commercial package DigiSim^{TM} in the case of cyclic voltammetry and with a finite difference homemade program for square wave voltammetry and chronoamperometry.

Regarding the latter, the results presented in Refs. [13, 14] have been applied such that the chemical and diffusion changes are evaluated sequentially, with the Crank-Nicolson method for time-integration preceded by four initial extrapolation steps to avoid oscillations. For the spatial discretization, exponentially expanding grid with high expansion factors and four-point formulae has been used.

The simulation program was developed and debugged by Dr. Eduardo Laborda. The fitting for square wave voltammetry was completed with the assistance of Dr. Eduardo Laborda.

5.1.3 Results and Discussion

The complete electrochemical characterization of redox systems requires the identification of the reaction mechanism, the determination of the heterogeneous and homogeneous kinetics, and the behaviour of the species involved in solution.

With this aim, square wave voltammetry (SWV) is employed. Besides being very advantageous in electroanalysis, this differential pulse technique is attractive

for quantitative analysis since it offers voltammograms better resolved, less distorted by capacitative effects and more sensitive to electrode kinetics than cyclic voltammograms. Further, the peak shape of the voltammograms facilitates its analysis through the variation with frequency of three well defined parameters: the peak current (I_p), the peak potential (E_p) and the half-peak width ($w_{1/2}$). Following this procedure, next the electro-oxidation of nitrite is investigated on glassy carbon, gold and EPPG macroelectrodes in different media.

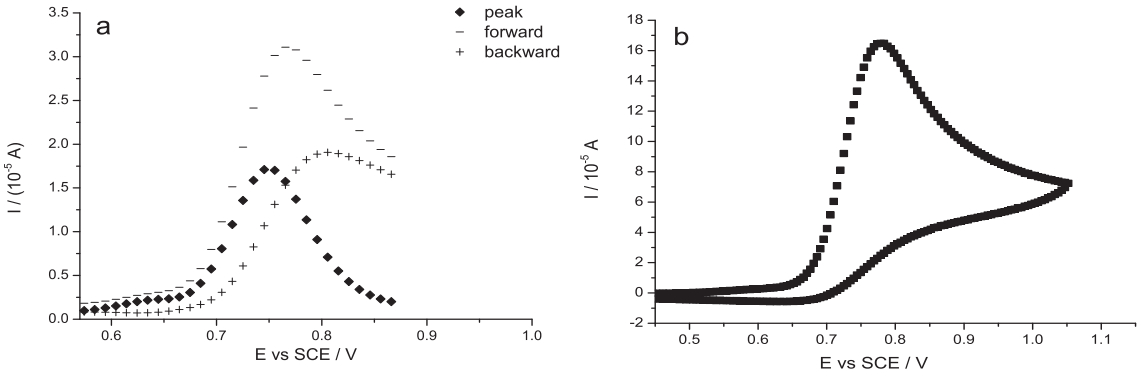


Figure 5.1: Representative forward, backward and net components of (a) a square wave voltammogram (f = 10 Hz, pulse amplitude = 15 mV, step potential = 10 mV) and (b) CV ($\upsilon = 0.1$ V$\cdot$ s^{-1}) of the electro-oxidation of nitrite on glassy carbon electrode. Solution: 2 mM $NaNO_2$, 0.16 M Na_2SO_4, pH 4.6.

A first qualitative analysis of the voltammograms reveals the absence of the reverse reaction (i.e., reduction of NO_2) in the backward component of the SWV voltammograms (Figure 5.1.a) as well as in the CV signal (Figure 5.1.b) which shows a single oxidative peak (situated at 0.78 V (vs. SCE) on glassy carbon). This could be explained by the inference of an irreversible electrode process (E_i mechanism) or a coupled chemical reaction consuming the oxidized species, namely, EC− or catalytic−type mechanisms. The quantitative analysis of the experimental

results (see below) indicates the occurrence of the second-order catalytic mechanism proposed by Guidelli *et al.* [15] (see Eq.5.1 and Eq.5.2), according to which nitrite is regenerated in solution by the disproportionation of electrogenerated NO_2.

Regarding the electrode kinetics, according to the Butler-Volmer formalism, the oxidation and reduction rate constants are given by:

$$k_{ox} = k^0 \cdot e^{\beta\eta} \tag{5.3}$$

$$k_{red} = k^0 \cdot e^{-(1-\beta)\eta} \tag{5.4}$$

with $\eta = F(E\text{-}E_f^0)/RT$, E_f^0 being the formal potential, T the absolute temperature and k^0 the standard heterogeneous rate constant, β is the transfer coefficient.

The above catalytic reaction scheme is also compatible with limiting current chronoamperograms (shown in Figure 5.2) such that a current greater than that expected for an E or EC mechanism $D_{NO_2^-} = 1.8 \times 10^{-5}$ cm^2 ·s^{-1} [12, 15, 16] is obtained, due to the regeneration of the reduced electroactive species. From the fitting of the chronoamperograms with the diffusion coefficient of nitrite (D) and the disproportionation constant (k_{disp}) as adjustable parameters, and considering the reaction scheme given by Eq. 5.1 and Eq. 5.2, the following values were obtained: D = (1.9 ± 0.1) × 10^{-5} cm^2 ·s^{-1} and k_{disp} = (2.0 ± 0.1)× 10^6 M^{-1} ·s^{-1}. These are in good agreement with previous data in the literature [12, 15, 16] and enable satisfactory fitting of SWV (see below).

Moreover, this mechanism has been employed successfully in several studies [4–

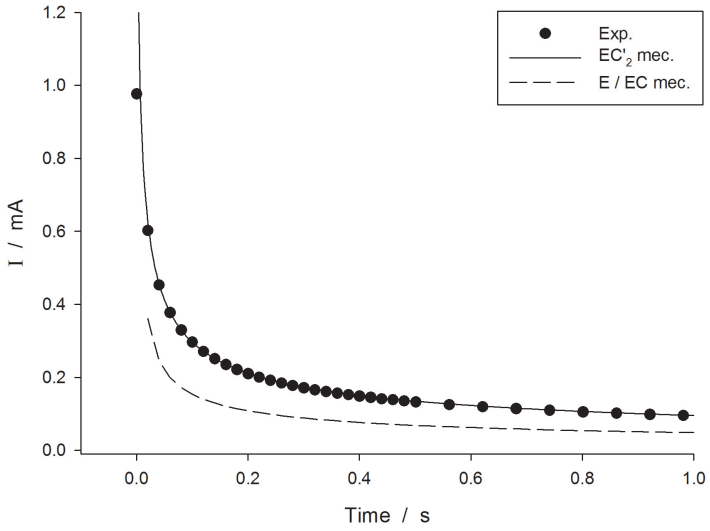


Figure 5.2: Experimental (points) limiting current chronoamperograms recorded on glassy carbon. Solid line corresponds to the best-fit theoretical curve considering the reaction mechanism given by Eq.5.1 and 5.2 and dashed line to the chronoamperogram predicted for E and EC mechanisms with $D_{NO_2^-}$=1.8×10^{-5}cm^{2}s^{-1}. Solution: 3 mM $NaNO_2$, 0.5 M NaCl, pH 4.6.

6, 12, 15–17], and data for the disproportionation constant (k_{disp}) have been reported by means of electrochemical and non-electrochemical methods [12]. In contrast, the electrode kinetics has received less attention such that this has been usually presumed or its effects have been avoided by working under diffusion-limited conditions. Here, the study of the redox system (Eq. 5.1 and Eq. 5.2) is carried out by characterizing both the chemical and electrochemical processes, extracting the disproportionation rate constant, k_{disp}, and the parameters associated with the electrode kinetics.

First, the effect of the solution pH on the electrochemical response is evaluated. The variation of the peak current and potential of cyclic voltammograms at glassy

carbon electrode are shown in Figure 5.3. As can be seen, the peak current increases gradually with pH while the peak overpotential decreases, both magnitudes reaching a stable value for pH > 4. The latter is in agreement with the irreversible chemical reaction assumed in Eq. 5.1 and Eq.5.2. The decrease of the electrochemical signal at low pH can be attributed to the instability of the predominant electroactive species HNO_2 (pKa = 3.3 at 25 °C) [18]. However, basic solutions can promote the formation of oxide layers on the electrode surface which inhibit the oxidation of nitrite [12]. Consequently, a compromise value of 4.6 was employed for subsequent studies.

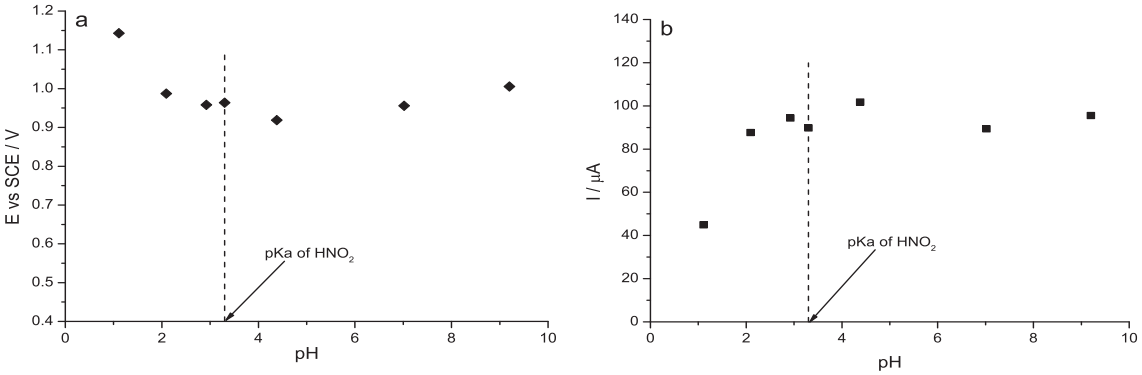


Figure 5.3: Influence of pH on the (a) peak potential and (b) peak current of cyclic voltammograms corresponding to the electro-oxidation of nitrite at glassy carbon electrode. $\upsilon = 1$ V$\cdot$ s^{-1}. Solution: 1 mM $NaNO_2$, 0.1 M NaCl.

Figure 5.4 shows the experimental and theoretical SWV voltammograms for different electrodes and supporting electrolytes. The analysis of the voltammograms indicates that in all cases the electron transfer rate increases in passing from GC to EPPG to gold electrodes, such that the height of the peak increases and the peak potential is situated at smaller overpotentials. Nevertheless, this initial conclusion

must be taken with caution due to the inference of the coupled disproportionation reaction and the quantitative analysis of the peaks is required. This has been done by the simultaneous fitting of the peak height (I_p), peak potential (E_p) and half-peak width ($w_{1/2}$) at different frequencies in the range 10 - 200 Hz.

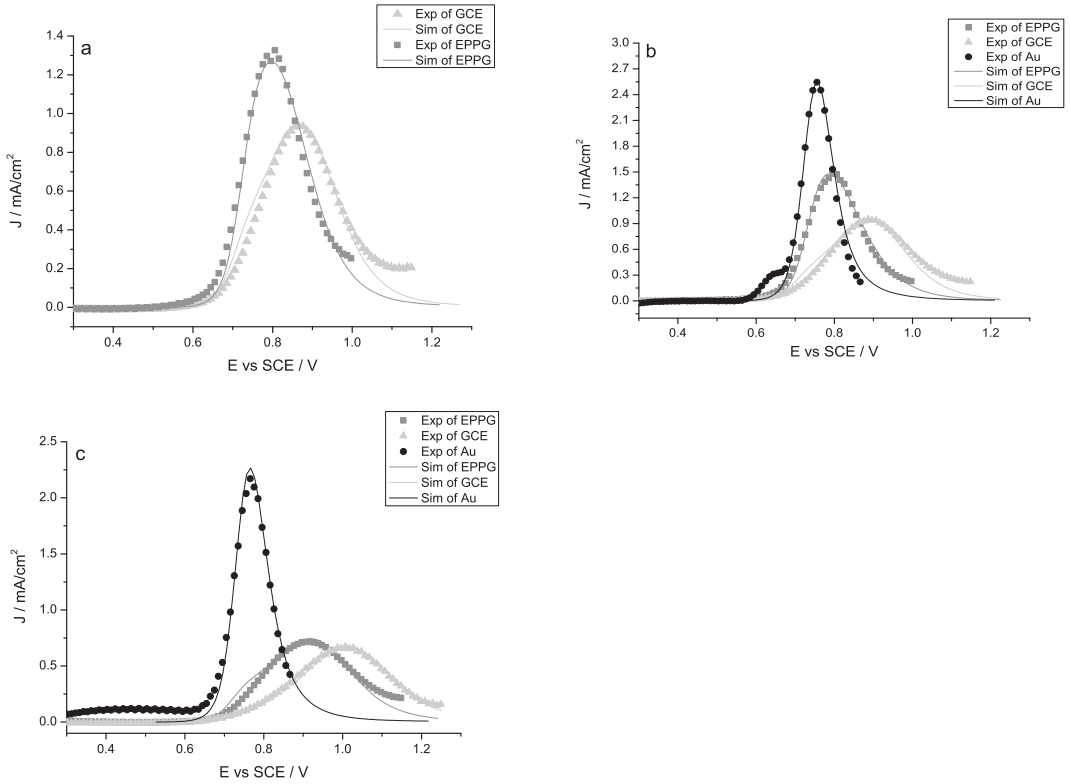


Figure 5.4: Experimental (points) and theoretical (solid line) SWV voltammograms corresponding to the electro-oxidation of nitrite at different electrodes with (a) NaCl, (b) Na_2SO_4 and (c) $NaClO_4$ as supporting electrolyte. Frequency = 100 Hz, pulse amplitude = 15 mV, step potential = 10 mV. Solution: 2 mM $NaNO_2$, pH 4.6, ionic strength of the supporting electrolyte = 0.5 M.

In the case of GC electrodes, the study of the electro-oxidation of nitrite shows that this process is very sluggish. In such a case, the peak current and width are only dependent on the disproportionation rate constant and the electron transfer coefficient (β). Thus, from I_p and $w_{1/2}$, the value for k_{disp} has been corroborated

and the β value obtained (given in Table 5.1). These give rise to satisfactory fitting of square wave and cyclic voltammograms for all the supporting electrolytes considered and all the frequencies employed (see Figure 5.4 and Figure 5.5).

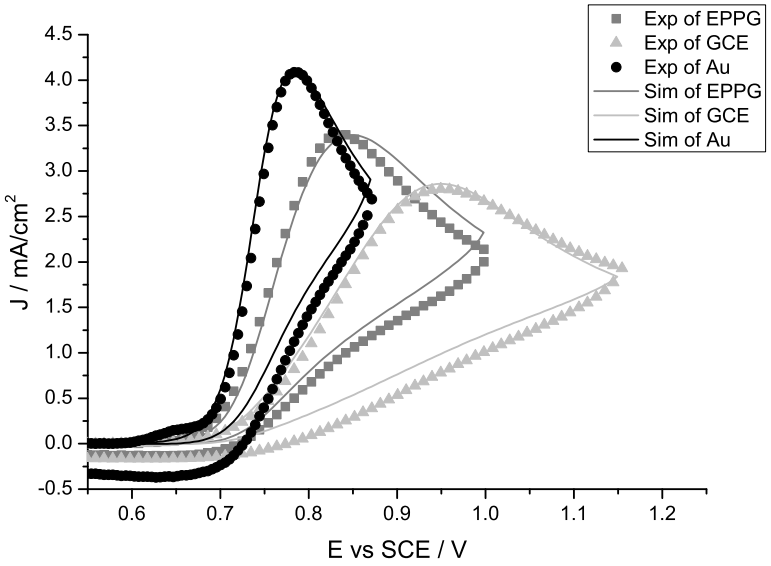


Figure 5.5: Experimental (points) and theoretical (solid) CV voltammograms corresponding to the oxidation of nitrite in Na_2SO_4 solution. The parameters employed for the simulations are those obtained from SWV (Table 5.1). v = 1 V $\cdot$ s^{-1}. Other conditions as in Figure 5.4.

Given that the nitrite oxidation kinetics is very slow on GC, the values of k_0 and E_f^0 cannot be determined separately from the voltammetric response and so the value $k^0 e^{\beta F E_f^0/RT}$ is given instead.

For EPPG electrode, quasireversible or irreversible behaviours are encountered, depending on the supporting electrolyte employed (see below). In the first case, the k_0 and β values were obtained from the values of the peak current and half-peak width, and once these were known, the peak potential enabled to extract

Table 5.1: Values for the electrochemical kinetic parameters obtained from the fitting of square wave voltammograms at different frequencies in the range 10 - 200 Hz.

Electrode	Electrolyte	k^0 / cm $\cdot s^{-1}$	E_f^o (*vs.* SCE) / V	β	$k^0 e^{\beta F E_f^o / RT}$/(cm $\cdot$ s^{-1})
EPPG	NaCl	0.026±0.001	0.782±0.001	0.620±0.001	–
	Na_2SO_4	0.032±0.001	0.792±0.001	0.64 ± 0.01	–
	$NaClO_4$	–	–	0.663 0.006	5.00×10^{-12}
GCE	NaCl	–	–	0.637±0.006	2.76×10^{-11}
	Na_2SO_4	–	–	0.643±0.006	1.83×10^{-11}
	$NaClO_4$	–	–	0.68±0.01	2.19×10^{-12}
Au	Na_2SO_4	> 0.1	0.776±0.001	–	–
	$NaClO_4$	> 0.1	0.786±0.004	–	–

the E_f^0value. In all the conditions studied (see Figure 5.4), the electrode reaction on EPPG is faster than on GCE. This behaviour has been reported previously for other redox systems [19] and it is related to the higher proportion of edge plane sites on the EPPG surface [20]. In the same way, this also explains the electrocatalytic effects reported for the oxidation of nitrite on carbon nanotube electrodes [21].

Finally, the electrode process was found to be reversible ($k^0 > 0.1$ cm $\cdot$ s^{-1}) on gold electrodes in all the conditions considered. Thus, the electrode process is much faster than on carbon-based electrodes (EPPG, GCE) such that the electron transfer rate decreases in the order: Au > EPPG > GCE. This significant influence of the nature of the electrode joins previous evidences of the strong dependence of the nitrite electro-oxidation on the state of the electrode surface [12, 17, 22]. This suggests that the electron transfer is inner-sphere and so strong interactions take place between the electroactive species and the electrode surface: adsorption

of nitrite [23–25].

Accordingly, the use of gold electrodes or the modification with gold particles is recommended for nitrite sensing, giving rise to greater signals at smaller overpotentials. As can be inferred by comparing Figure 5.4.b and Figure 5.5, the gain expected by the enhancement of electrode kinetics is greater in SWV than in cyclic voltammetry (CV). This result points out the greater sensitivity to the electrode kinetics of the peak current in SWV, which is very beneficial in terms of accuracy for quantitative analysis of electrode kinetics.

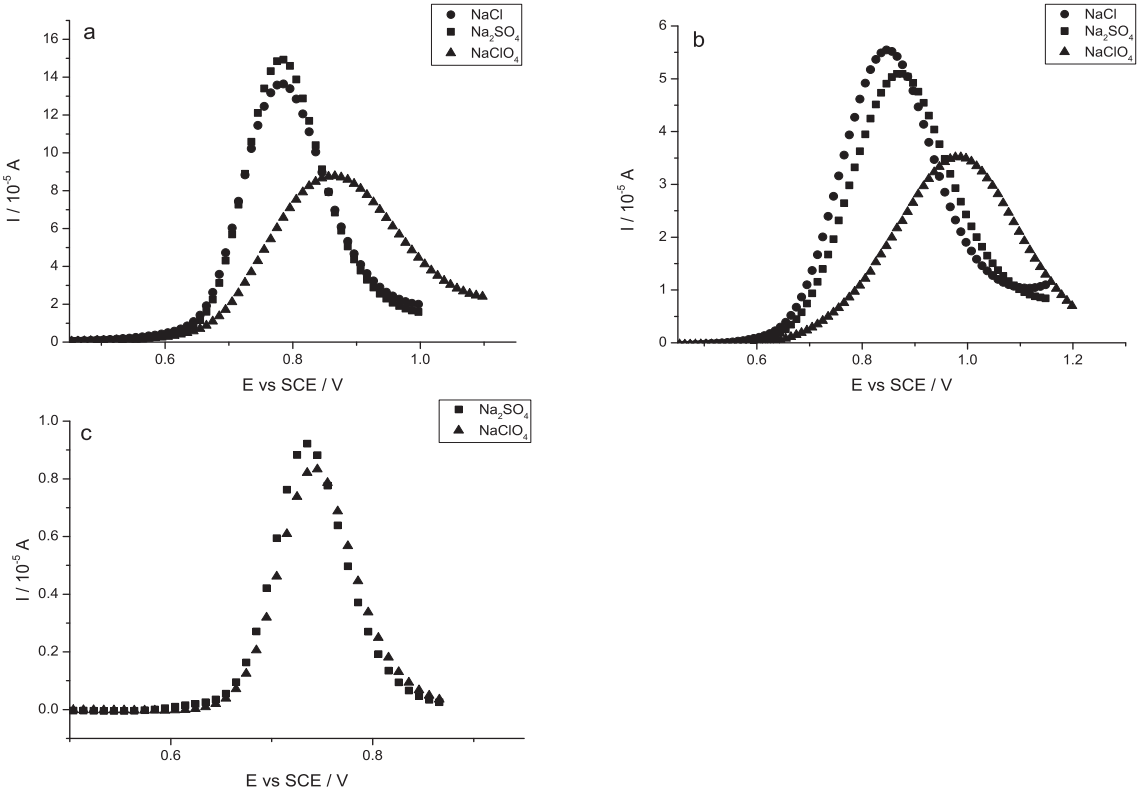


Figure 5.6: Experimental SWV voltammograms corresponding to the electrooxidation of nitrite on (a) EPPG (f = 50 Hz), (b) GC (f = 50 Hz) and (c) gold electrodes (f = 10 Hz), when different supporting electrolytes are used. Other conditions as in Figure 5.4.

The influence of the supporting electrolyte is investigated in Figure 5.6 at analogous conditions of ionic strength. From Figure 5.6 one can infer that the kinetics of the electrode reaction is significantly affected on carbon electrodes. The effect is much less significant in the case of gold electrodes, where the electrode reaction is essentially reversible both in Na_2SO_4 and $NaClO_4$ solutions (see Table 5.1). As shown in Figure 5.7, the signal for electro-oxidation of nitrite on gold electrode in chloride solution is very distorted due to the electrode surface oxidation promoted by Cl^-.

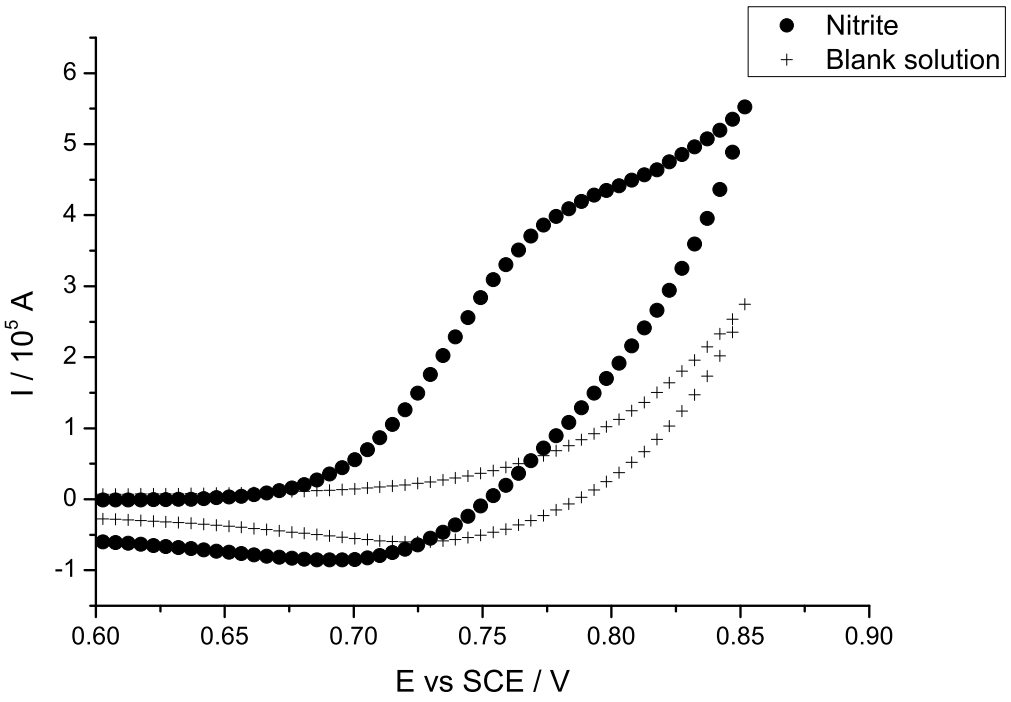


Figure 5.7: Cyclic voltammogram in the presence (circle points) and absence (plus points) of nitrite when gold electrodes are used in NaCl solution. Other conditions as in Figure 5.4.

Thus, the electrode reaction on EPPG and GC electrodes is slower in the presence

of perchlorate anions than when chloride or sulphate salts are used as supporting electrolyte. This behaviour was investigated by recording SWV voltammograms in solutions of different compositions and the presence of perchlorate anions seems to be responsible for the change in the electrode kinetics observed. As can be concluded from Figure 5.8, the addition of $NaClO_4$ to fully-supported nitrite solutions in NaCl or Na_2SO_4 gives rise to the decrease of the peak height and the shift of the peak towards greater overpotentials. Given the inner-sphere nature of the electron transfer process, a plausible explanation for this behaviour is the blocking effect of perchlorate anions inhibiting the necessary interaction between nitrite and the electrode surface.

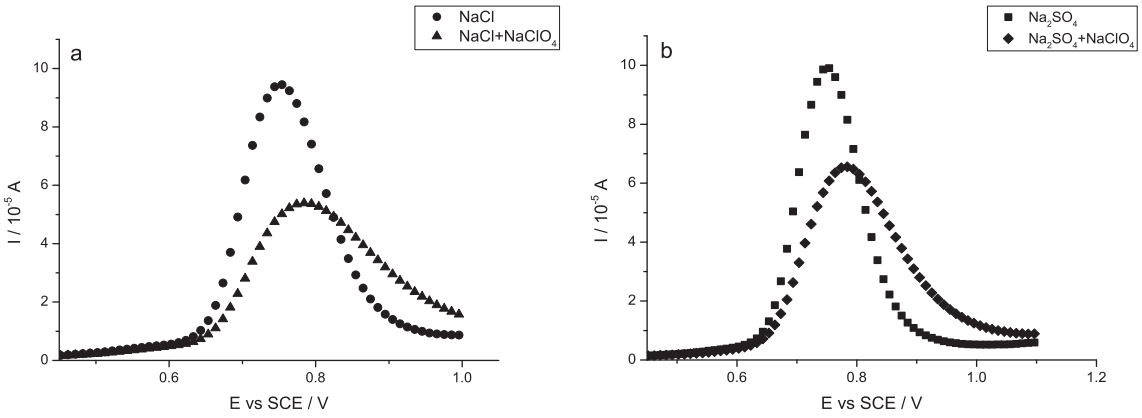


Figure 5.8: Influence of perchlorate anions on the SWV voltammograms recorded on EPPG electrode in 2 mM $NaNO_2$, 0.5 M NaCl (a) or Na_2SO_4 (b) solution in the absence (circle) and presence (0.5 M, triangle) of sodium perchlorate. f = 10 Hz, unbuffered solution. Other conditions as in Figure 5.4.

The above data and discussion can assist the development of more effective methodologies for electroanalysis of nitrite by employing bare or modified electrodes. This will be further discussed in section 5.2.

5.1.4 Conclusions

The electro-oxidation of nitrite at different electrodes and under different conditions of pH and supporting electrolyte has been investigated by square wave voltammetry. Besides the well-known advantages of SWV to obtain well-defined peaks, these have proven to be more sensitive to the electrode kinetics than cyclic voltammograms. This enables a more accurate evaluation of the kinetic parameters.

The experimental results indicate that this redox system follows a second-order catalytic mechanism:

$$NO_2^- \overset{k_{ox}}{\rightleftarrows} NO_2 + e^- \tag{5.5}$$

$$2NO_2 + H_2O \overset{k_{disp}}{\rightleftarrows} 2H^+ + NO_3^- + NO_2^- \tag{5.6}$$

The mechanistic and kinetic characterization of the system has given a value for the disproportionation rate constant of $k_{disp} = (2.0 \pm 0.1) \times 10^6$ $M^{-1} \cdot s^{-1}$, independently of the nature of the supporting electrolyte employed. The values obtained for the transfer coefficient, β, are significantly greater than 0.5 ($\beta = 1 - \alpha$) = 0.62 - 0.68).

The electrode kinetics exhibits a significant dependence on the nature of the electrode and the supporting electrolyte. In general, a reversible behaviour is found on gold macroelectrode, quasireversible on edge plane pyrolytic graphite and irreversible on glassy carbon. This trend suggests an inner-sphere nature of the electro-oxidation process such that a strong interaction occurs between the nitrite and the electrode surface for the electron transfer. The identity of the anion of the support-

ing electrolyte also affects the electrode kinetics on carbon electrodes such that it is inhibited by the presence of perchlorate anions.

5.2 Electro-oxidation of Nitrite and Ascorbic Acid on Gold Nanoparticles: a Joint Approach Using Computation and Experiment.

5.2.1 Introduction

Extensive works are devoted to the development of nanotechnology with groundbreaking applications in (electro) catalysis [26, 27], chemical analysis [28, 29], material science [30], medicine [31]. Geometric and electronic features of materials can vary with size affecting their physical (electrical, optical, magnetic, mechanic) and chemical properties [27, 32–34]. Understanding and controlling the behavior of nano-sized materials is essential for the efficient progress of nanoscience and it demands the development of methodologies for the preparation of structure-controlled nanoparticles (NPs) and the analysis of their characteristics.

In electrochemistry metal nanoparticles are widely employed for the modification of the electrode surface in order to develop (bio)sensors and energy production cells [26–29] as well as for environmental applications [35]. Nanoparticle-modified electrodes provide large effective surface area, enhanced mass transport and high control over local environment [29]. In addition, the reduction of the amount of

material enables the decrease of fabrication costs and environmental impact. In many cases modification with nanoparticles just leads to the increase of the surface area without affecting the electrode kinetics with respect to the bulk material. The aim of this section is to identify ***authentic*** nano-effects, that is, changes of the electron transfer kinetics at the nanoscale.

A widely-used strategy for electrode modification with metal nanoparticles is the drop-cast deposition of chemically prepared NPs. Synthesis of nanoparticles by reduction of a metal salt enables a better control of the size and structure of nanoparticles [36–38] though it often requires the use of capping agents that can alter the electrochemical response of both nanoparticles and substrate-electrode [39, 40].

Regarding characterization techniques, transmission electron microscopy (TEM), scanning electron microscopy (SEM), scanning tunneling microscopy (STM), atomic force microscopy (AFM) and X-ray diffraction (XRD) are commonly employed [33]. Electrochemical methods are also valuable to obtain information about metal nano particles [41, 42], given that the electrochemical response of electrode processes is influenced by the properties of the electrode material. When the particular properties of nanosized materials give rise to enhanced electrode kinetics, electrocatalytic effects are observed. Major issues in nanoelectrochemistry are related to the detection of these effects and their relationship with structural and/or electronic properties of the nanosized material in comparison with the bulk material.

Many examples of electrocatalysis have been claimed in the literature when modifying electrodes with noble metal nanoparticles, such as gold, platinum and silver

NPs [29]. Apart from the importance of understanding the nature of electrocatalysis, such effects are potentially very valuable in electroanalysis and energy production given that the triggering of the electrode reaction is facilitated. Moreover, the investigation of these phenomena can provide further insight into the factors governing electron transfer processes.

In most cases, electrocatalysis is tentatively identified from the reduction of the overpotential where the electrode reaction occurs and the increase of the magnitude of experimental voltammograms. Nevertheless, the corroboration of electrocatalytic effects must be carried out more carefully given that modification of electrodes involve changes in the electrode-solution interface that can mimic the effects expected when the electrode kinetics is enhanced [9, 43, 44]. For example, when porous layers are employed for the electrode modification, thin-layer diffusion of the electroactive species trapped between the layers takes place and gives rise to the shift of the voltammograms towards smaller overpotentials. Even in the case of bare electrodes modified with "naked" nanoparticles, the changes observed in the voltammograms might be explained simply by the response of an "array" of assembled nanoelectrodes with the same characteristics as the bulk material.

In this section, we tackle the detection of electrocatalytic nanoeffects by combining electrochemical experiments and computational simulations as summarized in the scheme shown in Figure 5.9. Thus, the response of the electrode modified with nanoparticles is first simulated assuming that the particles retain the electrode kinetics of the bulk material; this enables us to predict the response in

the absence of nanoeffects. Separately electrochemical experiments are performed with nanoparticle-modified electrodes, the characteristics of the modification being examined by electrochemical and imaging techniques. Finally, the comparison of simulated and experimental voltammograms enables the detection of differences between the kinetics at the bulk material and at the nanoparticles and, therefore, for revealing authentic nanoeffects.

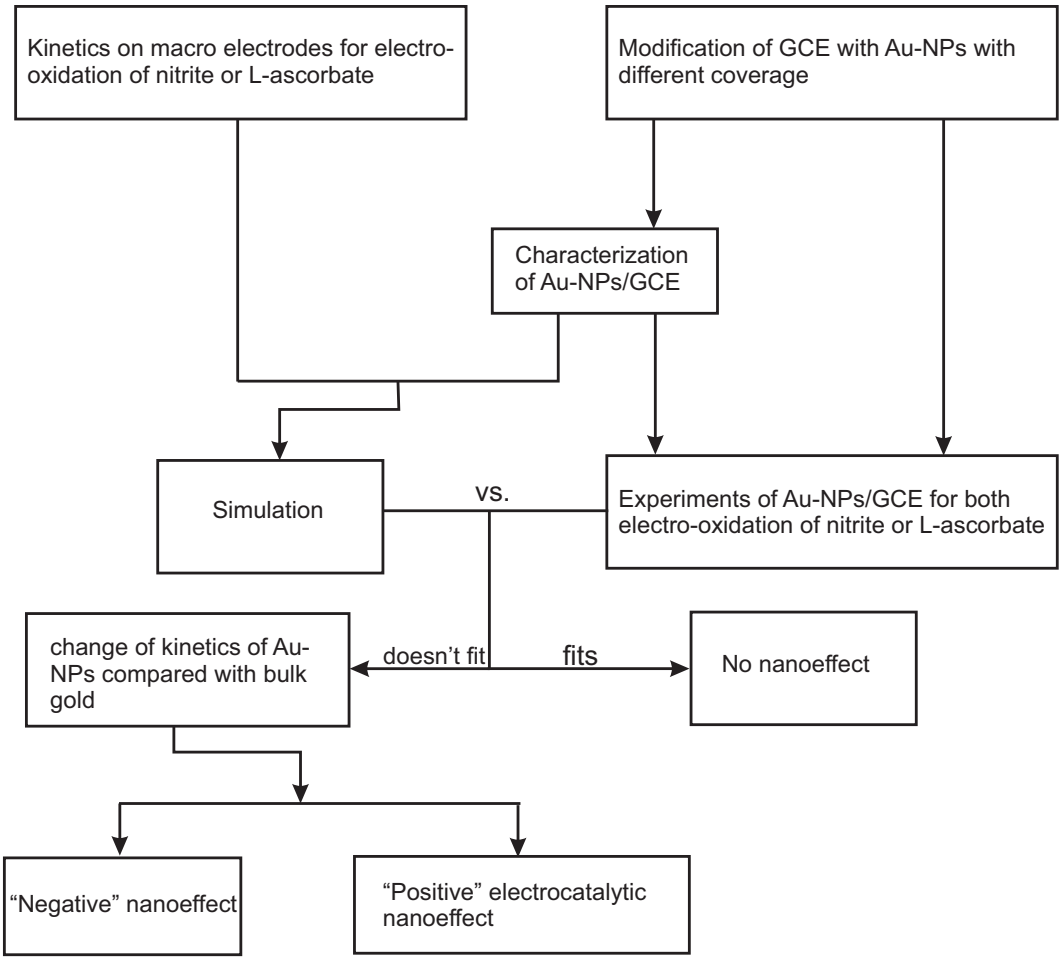


Figure 5.9: Approach followed in this work for the detection of nanoelectrocatalysis of the electrooxidation of nitrite and L-ascorbate by gold nanoparticles combining electrochemical measurements with computational simulations.

The theory is applied to the study of two electrode processes of biological and

industrial importance for which electrocatalytic effects by gold nanoparticles have been reported repeatedly [29]: electrooxidation of nitrite [6] and L-ascorbate [45–47] in aqueous solution. Modification of glassy carbon (GC) and indium tin oxide (ITO) electrodes with gold nanoparticles gives rise to significant shift of the voltammograms towards smaller overpotentials, which is commonly ascribed to electrocatalytic effects. The nature of these behaviours is investigated in this chapter by comparing the theoretical response predicted in absence of nanoeffects with that obtained on a glassy carbon electrode modified with ca. 20 - 90 nm-diameter gold NPs via the seed-mediated growth method [36–38, 48–50]. The comparison of the simulated and experimental results show that electrocatalysis is not observed for the electrooxidation of nitrite. On the other hand, the authentic enhancement of the electrooxidation kinetics of L-ascorbate on gold nanoparticles with respect to gold macroelectrodes is pointed out. The origin of such electrocatalytic nanoeffects is likely associated with the adsorptive mechanism of this electron transfer process.

5.2.2 Theory

5.2.2.1 Reaction Schemes

The electrooxidation of the nitrite ion in aqueous solution at the working pH of 4.6 on both gold and glassy carbon electrodes is known to proceed by the second order catalytic (DISP2) mechanism [1, 12] as discussed in section 5.1:

$$NO_2^- \xrightarrow{k_o} NO_2 + e^- \tag{5.7}$$

$$2NO_2 + H_2O \xrightarrow{K_{disp}} 2H^+ + NO_3^- + 2NO_2^- \tag{5.8}$$

This process consists of charge transfer at the electrode surface followed by a second-order disproportionation reaction which partially regenerates the starting material (the nitrite ion).

The electrooxidation of L-ascorbic acid at the working pH of 6.8 proceeds by the following scheme [40, 51, 52]:

$$AH^- \xrightarrow{k_1^o} A^- + H^+ + e^- \tag{5.9}$$

$$A^- \xrightarrow{k_2^o} DHA + e^- \tag{5.10}$$

$$DHA + H_2O \xrightarrow{k} HDHA \tag{5.11}$$

such that the two electron, one proton oxidation of L-ascorbate (AH-) results in the initial form of dehydro-L-ascorbic acid (DHAA) which undergoes hydrolysis (the product of which can suffer further oxidation) [40]. Accordingly, the above scheme has been modelled considering an EEC mechanism.

5.2.2.2 Numerical Simulation

Simulation program in this section was written and debugged by Dr. Kristopher Ward. Dr. Eduardo Laborda helped with the data interpretation.

The simulation methods employed are as used previously by this group for hemi-

spherical particles [53], and heterogeneous surfaces [54], although this is the first time a simulation of an array electroactive hemispherical particles on an electroactive surface has been performed. A summary of the important points is presented below.

Throughout this study, the substrate electrode used consists of a disc of glassy carbon (GC) modified with gold nanoparticles. The supporting glassy carbon substrate is a macro electrode (radius = 1.5 mm); the size and number of the nanoparticles vary depending on the growing time and were typically in the range 20 - 90 nm diameter and 2×10^8 - 6×10^8 particles respectively. The nanoparticles are assumed to be hemispherical in shape, and the surface coverage by the particles, Θ , is defined as:

$$\Theta = \frac{N\pi r_e^2}{A} \tag{5.12}$$

where N is the number of particles, r_e is the radius of a single nanoparticle and A is the area of the GC substrate. For the purposes of simulation, it is assumed that nanoparticles are of uniform size and that they are regularly distributed across the GC surface. Previous studies have demonstrated that for the time scale employed in this work there is little difference between the simulated voltammograms of arrays regularly and randomly distributed [55].

Computationally, the electrode is modelled in a 2D space through use of the diffusion domain approximation [56, 57]. The Butler-Volmer equation with an applied potential waveform appropriate to cyclic voltammetry is used to model electrode ki-

netics and diffusion is determined by Ficks second law which is discretised according the ADI method [58]. The simulation method employed allows the current response at each electroactive material (gold nanoparticle and GC electrode substrate) to be recorded separately. The resolution of the voltammetry into separate components in this manner allows for a greater insight into the mass transport phenomena present in the system. Simulation and duffusion domain approximation were introduced in chapter 2.

5.2.3 Experimental

5.2.3.1 Chemical Reagents

Sodium borohydride (98%, $NaBH_4$), gold(III) chloride trihydrate(>99%, $HAuCl_4 \cdot 3H_2O$), trisodium citrate (>99.0%), hexadecyltrimethylammonium bromide (CTAB), hydrochloric acid (37%,HCl),L-ascorbic acid (>99.0%), sodium hydroxide (>97%,NaOH) and lead(II) nitrate (>99.5%, $Pb(NO_3)_2$) were all purchased from Sigma-Aldrich and used as received without further purification. Citrate-capped gold nanoparticles were provided by Mintek (Randburg, South Africa). All the solutions were prepared using deionised water with a resistivity 18.2 MΩ (25° C).

5.2.3.2 Instrumental

Instrumental details for electrochemical measurements followed the same strategy described in the section 5.1.2.2.

5.2.3.3 Electrode Modification with Gold Nanoparticles

Seed-mediated growth method was used to modify a glassy carbon electrode [36–38, 48–50]. The polished GC electrode was immersed in the gold seeding solution containing 18 mL water, 0.5 mL (0.01 M) trisodium citrate, 0.5 mL $HAuCl_4$ (0.01 M) and 0.5 mL freshly prepared ice-cold aqueous $NaBH_4$ (0.10 M). After immersing in the seeding solution for 30 minutes, the electrode was sequentially rinsed by water and dried with nitrogen. Then the seeded electrode was immersed in the growth solution containing 18 mL CTAB (0.10 M), 0.5 mL $HAuCl_4$ (0.01 M) and 0.1 mL ascorbic acid (0.10 M) solutions for 2, 10 and 30 min to reach different degrees of coverage. Longer growing times may result in a higher degree of agglomeration of particles which compromised the accuracy of the characterization method here presented. The modified electrode was rinsed thoroughly with deionized water and dried under nitrogen atmosphere before electrochemical experiments.

5.2.4 Electrochemical Characterization

The modified electrode was first immersed into 1 mM $Pb(NO_3)_2$, 0.1 M NaOH solution to run cyclic voltammetry at 50 $mV{\cdot}s^{-1}$ in the range of 0.20 to 0.73 V (*vs.*SCE). After the experiments with lead the modified electrode was rinsed with distilled water and transferred into 0.1 M HCl. Stripping experiments in hydrochloric acid were carried out by scanning between 0.70 and 1.30 V (*vs.*SCE). All the solutions were deoxygenated by purging with nitrogen gas for about 30 minutes and the

experiments were carried out under N_2 atmosphere.

5.2.5 Results and Discussion

5.2.5.1 Characterization of Au NP-Modified GC Electrodes

Electrochemical characterization of the modified electrode was carried out immediately following each experiment with nitrite or L-ascorbate. The total coverage of NPS, that is, the surface area of gold nanoparticles, was estimated by the lead deposition method developed by Hernandez *et.al* [59]. Underpotential deposition (UPD) is commonly used to characterize the electrode surface structure as it is sensitive to the arrangement of atoms. Lead UPD in alkaline solution has proved to be a suitable system to estimate the surface area and morphology of gold NPs [60]. In chapter 4, a detailed explanation for this method was introduced.

Figure 5.10 shows the voltammetric profiles of a bare glassy carbon and Au-NPs/GCE in the presence of 1 mM $Pb(NO_3)_2$ and 0.1 M NaOH at 298 K, 50 mVs^{-1}. The surface area of gold nanoparticles can be determined from the stripping peaks [59, 60]. Au(111) contributes to the narrow and sharp stripping peak at potential 0.58 V (*vs.* SCE) and 380 $\mu C \cdot cm^{-2}$ is the charge associated with the lead UPD process [59, 60]. A broader stripping peak at 0.42 V (*vs.* SCE) corresponds to Au(110) and Au(100) crystal planes. The charge associated with the lead UPD process have been reported to be 330 $\mu C \cdot cm^{-2}$ and 340 $\mu C \cdot cm^{-2}$ for Au(110) and Au(100) respectively [59].

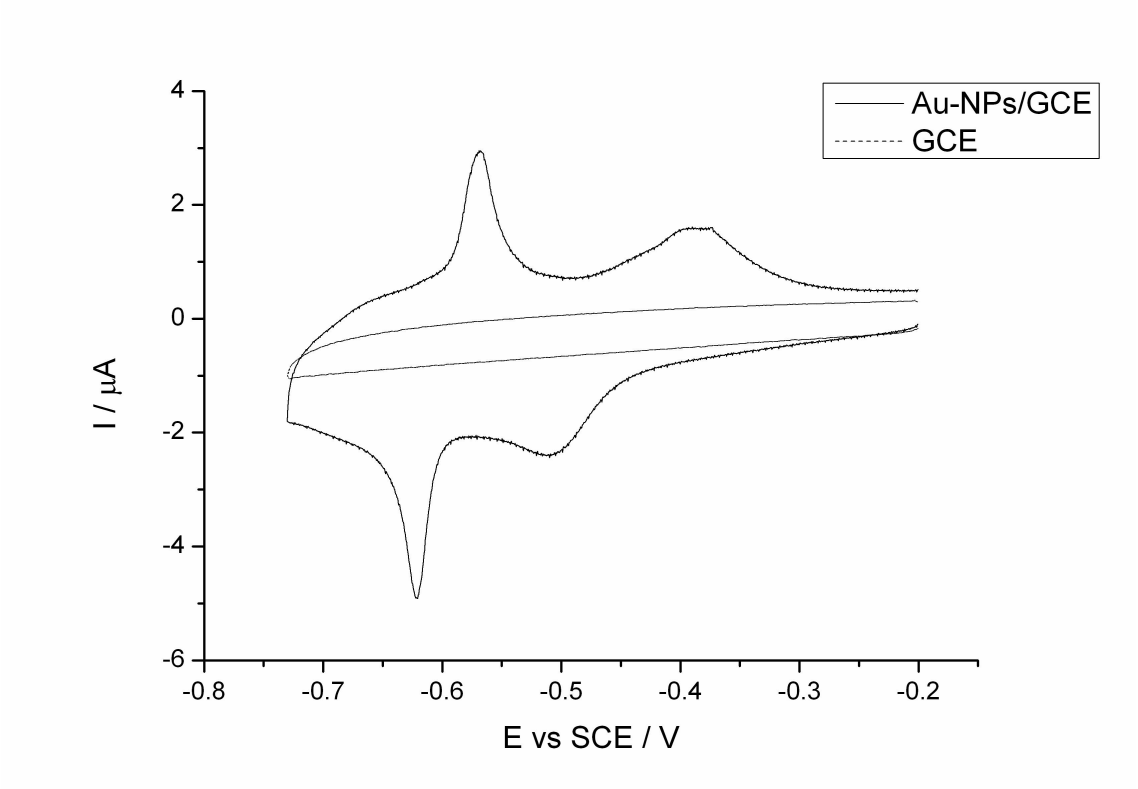


Figure 5.10: Cyclic voltammogram corresponding to lead deposition on gold nanoparticles deposited on GC electrode in 1 mM $Pb(NO_3)_2$ and 0.1 M NaOH solution. Scan rate: 50 mVs^1.

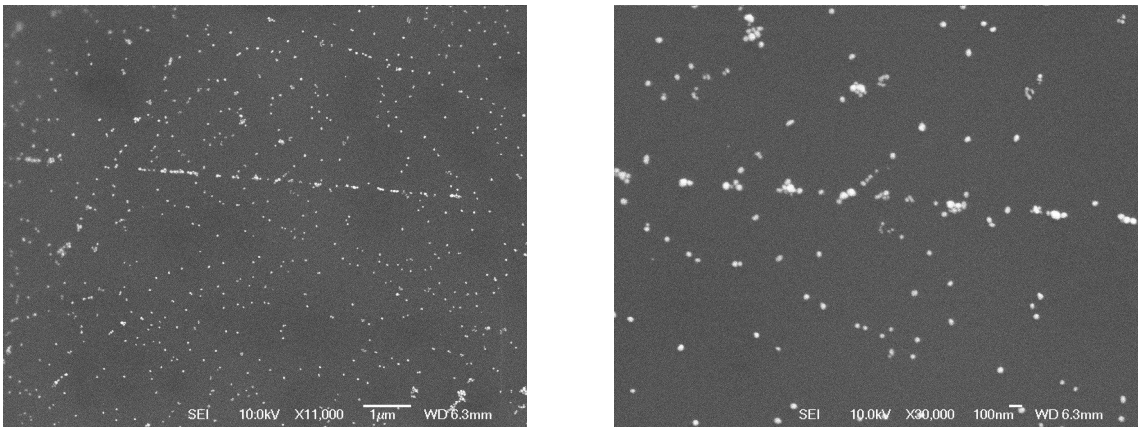


Figure 5.11: Scanning electron microscopy images of a glassy carbon electrode modified with gold nanoparticles by seed-mediated growth method with a growing time of 30 min.

Scanning electron microscope (SEM) images of the surface of the modified GC electrodes were also obtained in order to evaluate the size and distribution of the nanoparticles. The SEM images of Au/GC electrodes after a growing time of 30 min are shown in Figure 5.11. Gold nanoparticles show spherical shape, with an average size of ca. 40 nm diameter and a total number of ca. 10^8 NPs (i.e., ca. 10^9 NP cm^{-2}). The SEM images also point out the monodispersity and even distribution of the particles on the GC surface.

The size of the particles was confirmed to increase during the growing time with an average diameter of ca. 20 nm after 2 min, 30 nm after 10 min and 40 nm after 30 min. Due to problems of aggregation [61] the electrochemical approach could not be used for sizing the nanoparticles obtained with a growing time of 120 min. In this case, SEM images were employed determining a size similar to that for 30 min growing time (i.e., ca. 40 nm diameter). This is a consequence of the effect of the capping agent (CTAB), the adsorption of which on the nanoparticle surface slows down and eventually prevents its growth.

The above sizes of nanoparticles correspond to coverage values in the range Θ = 1 - 8 %.

5.2.5.2 "Side Effects" of the Electrode Modification on the Electrooxidation Kinetics

The adsorption of the surfactant employed in the electrode modification (CTAB) on gold and carbon surfaces has been previously documented in the literature [40, 62,

63]. Accordingly, its effect on the electrooxidation kinetics of nitrite and L-ascorbate was evaluated in this work.

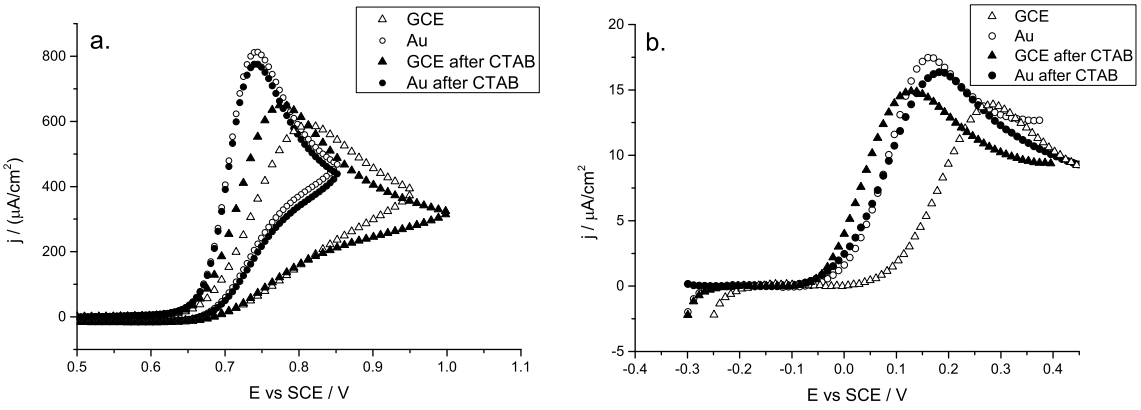


Figure 5.12: Effect of the immersion of the gold and glassy carbon electrodes in a CTAB solution on the electrooxidation of nitrite (a) and L-ascorbate (b). White points correspond to the bare electrodes and black points to the electrodes after 30 min immersion in a 0.1 M CTAB solution and rinse with water. Scan rate: 25 mVs^{-1}. Nitrite solution: 2 mM $NaNO_2$, 0.3 M Na_2SO_4, pH 4.6. L-ascorbate solution: 0.1 mM L-ascorbic acid, 0.1 M PBS, pH 6.8.

The effect on the electro-oxidation of nitrite and L-ascorbate was examined by recording cyclic voltammograms of both processes on gold and glassy carbon macro-electrodes before (white points in Figure 5.12) and after immersion in 0.1 M CTAB solution for 30 min and rinse with distilled water (black points in Figure 5.12). As can be seen in Figure. 5.12.a for nitrite and Figure 5.12.b for L-ascorbate, the CTAB treatment influences the electrochemical response on gold and glassy carbon in opposite ways, the kinetics being slowed down in the former and speeded up in the latter. Both effects are more apparent in the case of L-ascorbate giving rise to the inversion of the kinetics with respect to the bare electrodes. Thus, whereas at bare electrodes (white points) the process is faster on Au than on GC electrodes,

the L-ascorbate electrooxidation is faster on GC than on Au after the "CTAB treatment" (white points). The greater sensitivity of the L-ascorbate electro-oxidation to CTAB adsorption points out that the inner-sphere character of this electrode process is higher than the nitrite electro-oxidation.

Table 5.2: Kinetic parameters for the electro-oxidation of nitrite on gold and glassy carbon electrodes after immersion in CTAB solution 0.1 M for 30 min. The values are obtained from fitting of experimental cyclic voltammograms at different scan rates: 50 - 500 mVs^{-1}. See scheme given by Eq. 5.7 and Eq. 5.8.

Electrode	k^0 / ($cm{\cdot}s^{-1}$)	α	E_f^0 / (mV vs SCE)	k_{disp} / $M^{-1}{\cdot}s^{-1}$
CTAB/Au	0.075	-	776	2.0×10^6
CTAB/GCE	0.013	0.6		

Table 5.3: Kinetic parameters for the electrooxidation of L-ascorbate on gold and glassy carbon electrodes after immersion in CTAB solution 0.1 M for 30 min. The values are obtained from fitting of experimental cyclic voltammograms at different scan rates: 25 - 100 mVs^{-1}. See scheme given by Eq. 5.9 - Eq. 5.11.

	$k^0 exp((1-\alpha)E_f^0F/RT)$ / $cm{\cdot}s^{-1}$			
Electrode	Eq. 5.9	Eq. 5.10	α	k / s^{-1}
CTAB / Au	4.40×10^{-4}	1.47×10^{-4}	0.54	1.3×10^3
CTAB / GCE	2.79×10^{-4}	1.47×10^{-2}		

In order to take into account the above effects in our study, the kinetics of both electrooxidation processes were examined on CTAB-modified electrodes (referred as CTAB/Au and CTAB/GC hereafter). Thus, bare gold and GC macroelectrodes were immersed in a 0.1 M CTAB solution for a time equivalent to that employed

in the growing step of the electrode modification. Then, the electrodes were thoroughly rinsed with water, placed into the nitrite or L-ascorbate solution and cyclic voltammograms were recorded at different scan rates between 50 and 500 mVs^{-1}. From the fitting of the experimental results with the simulation software DigiSim the quantitative kinetic analysis of both systems was carried out according to the reaction mechanisms discussed in section 5.2.2.1. The values of the diffusion coefficient employed in the simulations were 1.9 $\times 10^{-5}$ $cm^2 \cdot s^{-1}$ for nitrite and 6.0 $\times$ 10^{-6} $cm^2 \cdot s^{-1}$ for L-ascorbate, both in good agreement with the values reported in the literature [1, 64–66]. As representative cases, the kinetic parameters obtained after 30 min immersion in the CTAB solution (0.1 M) are given in Tables 5.2 and 5.3. The relatively fast electron transfer rate constant in the electro-oxidation of nitrite may indicate a similar molecular structure (bond lengths, angles) of NO_2^- to NO_2. In contrast, a variety of reasons may lead to the slow electron transfer rate constant in the electro-oxidation of L-ascorbate, such as a markedly dissimilar structure between the reactant and the product, solvation effects and/or weak coupling between the electronic states of the electrode and the solution species.

The origin of the contrasting behaviour on gold and GC electrodes was further investigated by examining the adsorption of CTAB on the GC and gold electrode surfaces via X-ray photoelectron spectroscopy (XPS). The spectra of GC electrodes (Figure 5.13.) after immersion in 0.1 M CTAB solution for 30 min clearly show the peaks of N1s and Br, confirming the adsorption of CTAB on GC surfaces. In the case of gold electrodes (Figure 5.14), the presence of Br on the surface was also

confirmed. On the other hand, the results for N1s were not conclusive since peaks in the binding energy region of nitrogen were observed on gold samples both before and after the CTAB modification.

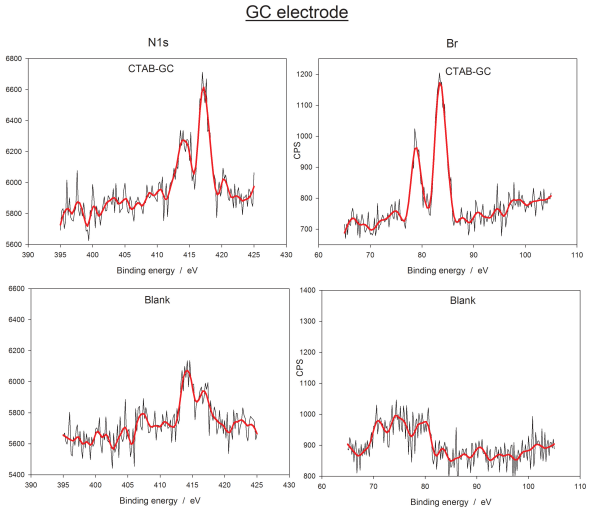


Figure 5.13: XPS spectra corresponding to the glassy carbon electrode before (bottom) and after (top) immersion in a 0.1 M CTAB solution for 30 minutes.

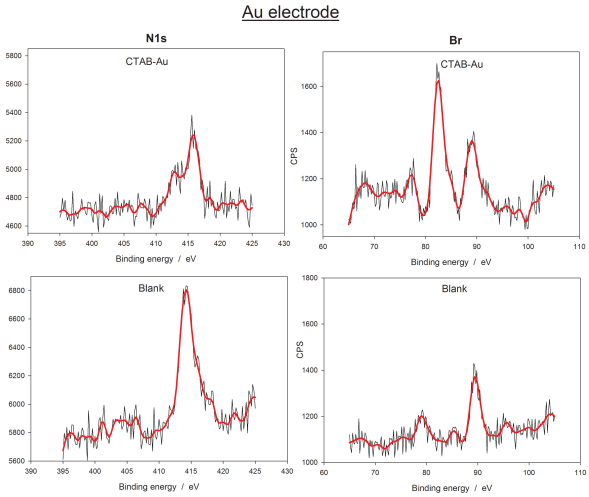


Figure 5.14: XPS spectra corresponding to the Au electrode before (bottom) and after (top) immersion in a 0.1 M CTAB solution for 30 minutes.

In view of this, cyclic voltammograms were recorded after immersing the gold

electrode in a 0.1 M NaBr solution in order to assess the effect of the bromide adsorption on the electrooxidation processes. The effect on the experimental voltammograms (Figure 5.15) was similar to those obtained after immersion in CTAB solution (Figure 5.12), that is, the shift of the peaks to more positive potentials and smaller peak currents. This along with the XPS results suggests that the Br^{-1} adsorption is the main responsible for the kinetic changes described above. Note that this is also in agreement with the contrasting behavior observed for the electrooxidation kinetics on GC and Au electrodes after the CTAB treatment.

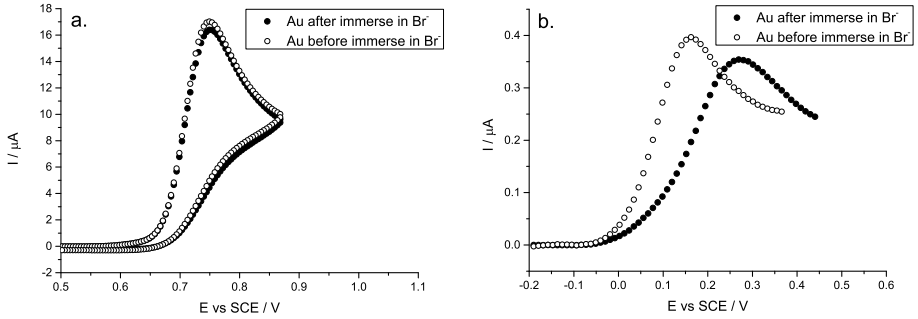


Figure 5.15: Effect of the adsorption of bromide on the gold electrode for the electrooxidation of (a). nitrite and (b). L-ascorbate. Open circles correspond to the bare electrodes and solid circles to the electrodes after 30 min immersion in a 0.1 M NaBr solution and rinse with water.Scan rate: 25 mVs^{-1}. Nitrite solution: 2 mM $NaNO_2$, 0.3 M Na_2SO_4, pH 4.6. L-ascorbate solution: 0.1 mM Lascorbic acid, 0.1 M PBS, pH 6.8

5.2.5.3 Electro-oxidation of Nitrite on Gold Nanoparticle Modified GC Electrodes: No Nanoelectrocatalysis

Nitrite solutions were prepared at pH 4.6 with a buffer solution containing acetic acid and sodium acetate according to previous studies [1]. As can be observed in Figure 5.12.a, a single oxidative peak at 0.74 V (vs SCE) on CTAB/Au and 0.78 V (vs

SCE) on CTAB/GCE electrodes is obtained given that the reactant species (NO_2^-) is regenerated in solution according to the DISP2 mechanism given by Eq. 5.7 and Eq. 5.8 (described in section 5.1) . The peak shows a higher density current on gold than on glassy carbon and it is situated at smaller overpotentials as corresponds to a more reversible process [1].

The experimental voltammograms obtained with the glassy carbon electrode modified with gold nanoparticles are shown in Figure 5.16 (circle points) for different coverage and scan rates at 298 K. After the modification, the shift of the voltammograms towards smaller overpotentials and the increase of the peak current are observed; the larger the gold NP coverage, the more apparent the changes in the voltammetry. The experimental results were compared with the simulations obtained considering the gold coverage on the GC electrode and the kinetic parameters obtained for bare glassy carbon and gold electrodes (black solid line). In all cases the agreement between experimental and theoretical results is good. The theoretical contributions of the gold nanoparticles (red line) and the GC substrate (grey line) are also plotted. Note that the peaks of both components are situated at similar potentials given that the electrode modification shifts the peak corresponding to the GC component with respect to the bare GC electrode as a result of the consumption of electroactive species by the Au-NPs. As expected, the NP component increases with the coverage from 40 % for $\Theta = 2$ % up to 70 % for $\Theta = 6$ % such that the responses obtained are representative and informative about the nanoparticle properties.

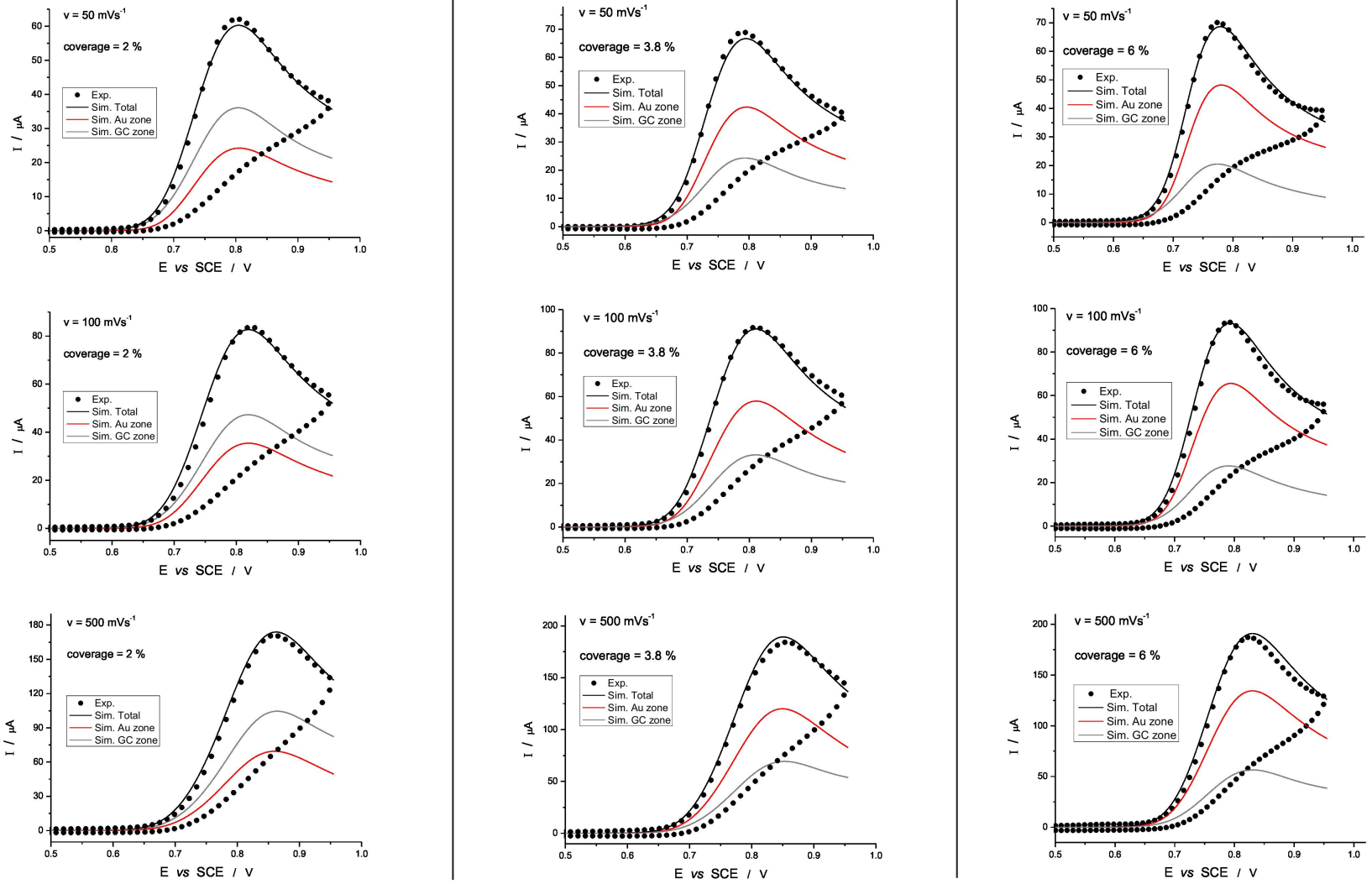


Figure 5.16: Experimental (points) and simulated (line) cyclic voltammograms corresponding to the electrooxidation of nitrite on CTAB/Au, CTAB/GC and Au-NP/GC electrodes at different scan rates and coverage (indicated on the graphs). Other conditions as in Figure 5.12.

From the good agreement of experimental and simulated voltammograms changes in the electrode kinetics of the electrooxidation of nitrite between the bare gold macroelectrode and the gold nanoparticles cannot be inferred. Accordingly, electrocatalytic nanoeffects can be discounted for the conditions of this study given that the electrochemical response observed agrees with that expected for a heterogeneous electrode with two spatial zones of different kinetics, i.e., the glassy carbon substrate and the gold nanoparticles.

5.2.5.4 Electrooxidation of L-Ascorbate on Gold Nanoparticle Modified GC Electrodes: Nanoelectrocatalysis.

The study of the electrooxidation of L-ascorbic acid was carried out at pH 6.8 (0.1 M PBS). A single oxidative peak at 0.18 V (vs SCE) on CTAB/Au and 0.13 V (vs. SCE) on CTAB/GC electrodes is observed corresponding to the two-electron oxidation of L-ascorbate. According to the scheme given by Eq. 5.9 - Eq. 5.11, the product of the electrode reaction undergoes hydrolysis and no reductive peak is observed at the scan rates employed (υ = 25 - 100 mV·s^{-1}).

According to the results shown in Figure 5.12.b assuming that the reactivity of L-ascorbate is the same on gold at both the macro- and nano-scales, the modification of GC electrode with Au NPs by seed-mediated growth method is not expected to have a catalytic effect on the response (i.e., increase of the current and decrease of the overpotential) given that the electrode reaction is slower on CTAB/Au (see Figure 5.17 and Table 5.3). Indeed, the results obtained from digital simulations

show that the cyclic voltammetry is not predicted to be affected significantly by the modification with Au NPs (see Figure 5.17) and that the contribution of the nanoparticles to the electrochemical signal is quite small(ca. 12 % in the peak current, see Figure 5.18. On the other hand, the experimental results with the modified electrodes show the shift of the voltammograms towards smaller overpotentials and greater current densities with respect to the theoretical predictions based on the kinetic parameters determined at the macro-scale (Table 5.3); the greater the coverage, the more apparent these effects (see Figure 5.18). This indicates that the electrode kinetics on the gold nanoparticles is faster than on gold macroelectrode and so the occurrence of electrocatalytic nanoeffects is verified.

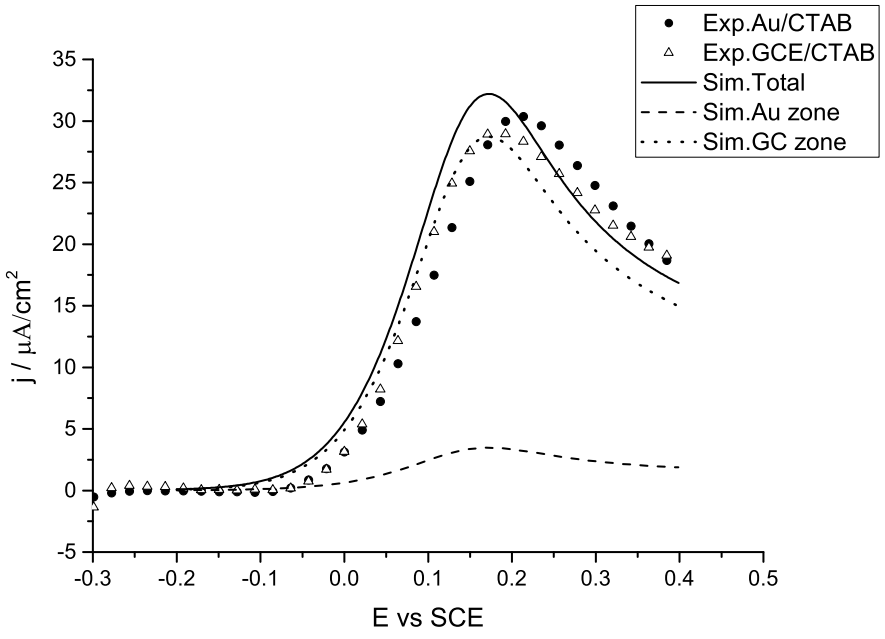


Figure 5.17: Experimental voltammograms (points) corresponding to the electrooxidation of L-ascorbate on CTAB/Au and CTAB/GC. Simulated voltammograms (line) corresponding to 8 % coverage are also plotted. Scan rate: 100 mVs^{-1}. Other conditions as in Figure 5.12 .

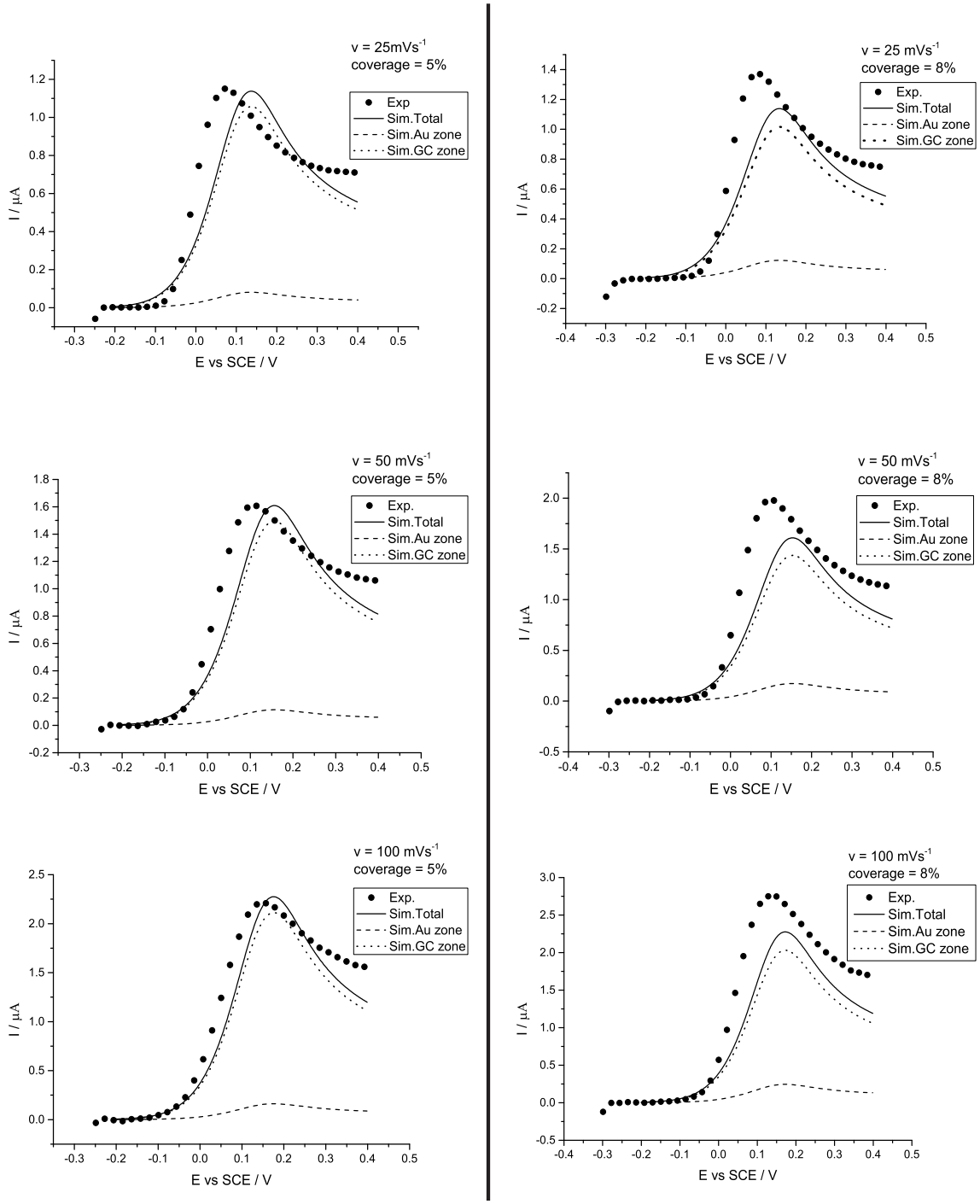


Figure 5.18: Experimental (points) and simulated (line) voltammograms corresponding to the electrooxidation of L-ascorbate on CTAB/Au, CTAB/GC and Au-NP/GC electrodes at different scan rates and coverage (indicated on the graphs). Other conditions as in Figure 5.12 .

Possible reasons of the electrocatalysis can be found attending to that electrooxidation of L-ascorbic acid is structure sensitive and significant differences between the voltammetry on polycrystalline gold electrodes and single crystal electrodes have been reported [40]. Accordingly, the electrocatalytic effects observed can be due to a change of mechanism (i.e., of the relative rates of the two electron transfer steps) associated with the surface structure of gold nanoparticles [67, 68]. However, nanoeffects related to particular electronic properties of the nanoparticles should also be considered. The quantitative comparison of the kinetics at gold nanoparticles and single crystal electrodes is of great interest to elucidate these fundamental aspects. The electrochemical approach for assessment of nanoeffects here presented can contribute to this aim.

5.2.6 Conclusions

An electrochemical approach for the detection of nanoeffects has been developed. The electrochemical response of electrodes modified with nanoparticles (NPs) is modelled considering different electrode kinetics on the surface of the substrate-electrode and on the NPs. This enables the evaluation of kinetic changes of electrode processes associated with the use of nanosized materials and therefore the investigation of electrocatalytic nanoeffects. The theory has been applied to the study of the possible electrocatalysis of the electrooxidation of nitrite and L-ascorbate by gold NPs. Glassy carbon macroelectrodes have been modified with Au NPs of 20 - 90 nm-diameter via the seed-mediated growth method. By comparison of experi-

mental and simulated voltammograms it is inferred that no differences are observed between the kinetics of electrooxidation of nitrite on gold nanoparticles and on gold macroelectrodes. So, electrocatalytic nanoeffects under the conditions here considered can be discarded. On the other hand, the authentic enhancement of the kinetics of the electrooxidation of L-ascorbate by nano-gold has been confirmed. The modification of the electrode can affect the surface of the substrate beyond the changes expected from the presence of the nanoparticles. Thus, the adsorption of the surfactant(CTAB) on glassy carbon affects the electrode kinetics of both electrooxidation processes which are faster after the CTAB-modification, particularly in the case of L-ascorbic acid. On the other hand, the bromide adsorption on gold electrodes gives rise to a decrease of the degree of reversibility, although this effect is less apparent than that due to CTAB adsorption.

Bibliography

[1] Y. Wang, E. Laborda and R. G. Compton, *Journal of Electroanalytical Chemistry* **670** (2012) 56–61.

[2] Y. Wang, K. R. Ward, E. Laborda, C. Salter, A. Crossley, R. M. Jacobs and R. G. Compton, *Small* **9** (2013) 478–486.

[3] W. J. Santos, P. R. Lima, A. A. Tanaka, S. M. Tanaka and L. T. Kubota, *Food Chemistry* **113** (2009) 1206–1211.

[4] C. Yu, J. Guo and H. Gu, *Electroanalysis* **22** (2010) 1005–1011.

[5] N. Spătaru, T. N. Rao, D. A. Tryk and A. Fujishima, *Journal of the Electrochemical Society* **148** (2001) E112–E117.

[6] B. R. Kozub, N. V. Rees and R. G. Compton, *Sensors and Actuators B: Chemical* **143** (2010) 539–546.

[7] M. J. Moorcroft, J. Davis and R. G. Compton, *Talanta* **54** (2001) 785–803.

[8] E. Laborda, A. Molina, F. Martínez-Ortiz and R. G. Compton, *Electrochimica Acta* **73** (2012) 3–9.

[9] I. Streeter, G. G. Wildgoose, L. Shao and R. G. Compton, *Sensors and Actuators B: Chemical* **133** (2008) 462–466.

[10] V. Mirceski, S. Komorsky-Lovric and M. Lovric, *Square-wave voltammetry: theory and application* (Springer, 2007).

[11] A. Molina, E. Laborda, F. Martínez-Ortiz, D. F. Bradley, D. J. Schiffrin and R. G. Compton, *Journal of Electroanalytical Chemistry* **659** (2011) 12–24.

[12] B. Piela and P. K. Wrona, *Journal of the Electrochemical Society* **149** (2002) E55–E63.

[13] F. Martínez-Ortiz, A. Molina and E. Laborda, *Electrochimica Acta* **56** (2011) 5707–5716.

[14] F. Martínez-Ortiz, N. Zoroa, Á. Molina, C. Serna and E. Laborda, *Electrochimica Acta* **54** (2009) 1042–1055.

[15] R. Guidelli, F. Pergola and G. Raspi, *Analytical Chemistry* **44** (1972) 745–755.

[16] X. Xing and D. A. Scherson, *Analytical Chemistry* **60** (1988) 1468–1472.

[17] B. Piela, P. Piela and P. K. Wrona, *Journal of the Electrochemical Society* **149** (2002) E357–E366.

[18] W. Braida and S. K. Ong, *Water, Air, & Soil Pollution* **118** (2000) 13–26.

[19] C. E. Banks, T. J. Davies, G. G. Wildgoose and R. G. Compton, *Chemical Communications* 829–841.

[20] C. E. Banks and R. G. Compton, *Analyst* **131** (2006) 15–21.

[21] Y. Zhao and S. Udpa, *IEEE Antennas and Propagation Society, AP-S International Symposium (Digest)* **2** (2003) 189–192.

[22] J. A. Cox and P. J. Kulesza, *Journal of Electroanalytical Chemistry and Interfacial Electrochemistry* **175** (1984) 105–118.

[23] I. G. Casella and A. M. Salvi, *Electroanalysis* **9** (1997) 596–601.

[24] A. J. Bard and L. R. Faulkner, *Electrochemical methods: fundamentals and applications, 2nd Edition*, volume 2 (Wiley New York, 2001).

[25] R. G. Compton and C. E. Banks, *Understanding voltammetry, 2^{nd} edition* (Imperial College Press, 2007).

[26] D. Astruc, *Nanoparticles and catalysis* (Wiley Online Library, 2008).

[27] M. T. M. Koper, *Nanoscale* **3** (2011) 2054–2073.

[28] S. Vaddiraju, I. Tomazos, D. J. Burgess, F. C. Jain and F. Papadimitrakopoulos, *Biosensors and Bioelectronics* **25** (2010) 1553 – 1565.

[29] F. W. Campbell and R. G. Compton, *Analytical and Bioanalytical Chemistry* **396** (2010) 241–259.

[30] O. D. Velev and S. Gupta, *Advanced Materials* **21** (2009) 1897–1905.

[31] T. Vo-Dinh, *Nanotechnology in biology and medicine: methods, devices, and applications* (CRC Press, 2007).

[32] D. Uzio and G. Berhault, *Catalysis Reviews* **52** (2010) 106–131.

[33] M.-C. Daniel and D. Astruc, *Chemical Reviews* **104** (2004) 293–346.

[34] J. Solla-Gullón, F. Vidal-Iglesias and J. Feliu, *Annual Reports Section" C"(Physical Chemistry)* **107** (2011) 263–297.

[35] L. Rassaei, F. Marken, M. Sillanpää, M. Amiri, C. M. Cirtiu and M. Sillanpää, *TrAC Trends in Analytical Chemistry* **30** (2011) 1704–1715.

[36] M. Oyama, *Analytical Sciences* **26** (2010) 1–12.

[37] N. R. Jana, L. Gearheart and C. J. Murphy, *Langmuir* **17** (2001) 6782–6786.

[38] N. R. Jana, L. Gearheart and C. J. Murphy, *Journal of Physical Chemistry B* **105** (2001) 4065–4067.

[39] X.-L. Wen, Y.-H. Jia and Z.-L. Liu, *Talanta* **50** (1999) 1027–1033.

[40] V. Ferreira, J. Solla-Gullón, A. Aldaz, F. Silva and L. Abrantes, *Electrochimica Acta* **56** (2011) 9568–9574.

[41] J. Hernández, J. Solla-Gullón, E. Herrero, J. Feliu and A. Aldaz, *Journal of Nanoscience and Nanotechnology* **9** (2009) 2256–2273.

[42] J. Solla-Gullon, F. Vidal-Iglesias, P. Rodriguez, E. Herrero, J. Feliu, J. Clavilier and A. Aldaz, *Journal of Physical Chemistry B* **108** (2004) 13573–13575.

[43] G. P. Keeley and M. E. Lyons, *International Journal of Electrochemical Science* **4** (2009) 794–809.

[44] E. Laborda, A. Molina, F. Martínez-Ortiz and R. G. Compton, *Electrochimica Acta* **73** (2012) 3–9.

[45] G. Hu, Y. Ma, Y. Guo and S. Shao, *Electrochimica Acta* **53** (2008) 6610–6615.

[46] L. Zhang and X. Jiang, *Journal of Electroanalytical Chemistry* **583** (2005) 292–299.

[47] P. Kannan, S. Sampath and S. A. John, *Journal of Physical Chemistry C* **114** (2010) 21114–21122.

[48] C. J. Murphy and N. R. Jana, *Advanced Materials* **14** (2002) 80 – 82.

[49] Y. Cui, C. Yang, W. Zeng, M. Oyama and W. Pu, *Analytical Sciences* **23** (2007) 1421–1425.

[50] T. K. Sau and C. J. Murphy, *Journal of the American Chemical Society* **126** (2004) 8648–8649.

[51] M. Rueda, A. Aldaz and F. Sanchez-Burgos, *Electrochimica Acta* **23** (1978) 419–424.

[52] R. G. Compton and F.-M. Matysik, *Electroanalysis* **8** (1996) 218–222.

[53] K. R. Ward, N. S. Lawrence, R. S. Hartshorne and R. G. Compton, *Journal of Physical Chemistry C* **115** (2011) 11204–11215.

[54] K. R. Ward, N. S. Lawrence, R. S. Hartshorne and R. G. Compton, *Physical Chemistry Chemical Physics* **14** (2012) 7264–7275.

[55] T. J. Davies and R. G. Compton, *Journal of Electroanalytical Chemistry* **585** (2005) 63–82.

[56] H. Reller, F. Kirowa-Eisner and E. Gileadi, *Journal of Electroanalytical Chemistry and Interfacial Electrochemistry* **138** (1982) 65–77.

[57] C. Amatore, J. Saveant and D. Tessier, *Journal of Electroanalytical Chemistry and Interfacial Electrochemistry* **147** (1983) 39–51.

[58] W. H. Press, S. A. Teukolsky, W. T. Vetterling and B. P. Flannery, *Numerical recipes: the art of scientific computing. 2007*, 2007.

[59] J. Hernandez, J. Solla-Gullon and E. Herrero, *Journal of Electroanalytical Chemistry* **574** (2004) 185–196.

[60] M. O. Finot, G. D. Braybrook and M. T. McDermott, *Journal of Electroanalytical Chemistry* **466** (1999) 234–241.

[61] Y. Wang, E. Laborda, C. Salter, A. Crossley and R. G. Compton, *Analyst* **137** (2012) 4693–4697.

[62] J. Vivek and I. J. Burgess, *Langmuir* **28** (2012) 5031–5039.

[63] C. Hu and S. Hu, *Electrochimica Acta* **49** (2004) 405–412.

[64] P. Karabinas and D. Jannakoudakis, *Journal of Electroanalytical Chemistry and Interfacial Electrochemistry* **160** (1984) 159–167.

[65] J. J. Mertens, E. Jacobs, A. J. Callaerts and A. Buekens, *Analytical Chemistry* **54** (1982) 2620–2622.

[66] H. Ernst and M. Knoll, *Analytica Chimica Acta* **449** (2001) 129–134.

[67] I. F. Hu and T. Kuwana, *Analytical Chemistry* **58** (1986) 3235–3239.

[68] Z. Dursun, L. Pelit and I. Taniguchi, *Turkish Journal of Chemistry* **33** (2009) 223–31.

Chapter 6

Oxygen Reduction Reaction in Strong Acid Media on Different Sizes of Gold Nanoparticle

In this chapter, the electron transfer kinetics for oxygen reduction reaction in 0.5 M sulphuric acid solution are investigated at different sizes of gold nanoparticles. In the section 6.1, kinetic and mechanistic studies of the oxygen reduction reaction (ORR) in oxygen saturated 0.5 M sulphuric acid at 298 K at a gold macro electrode and at a electrodeposited gold nanoparticles modified glassy carbon electrode are reported. The conditions of electrodeposition are optimized to obtain small nanoparticles of diameter from 17 nm to 40 nm. The mechanism and kinetics of ORR on gold macro electrodes are studied and compared with those extracted for nanoparticle-modified electrodes. The mechanism involves two electron and two proton transfers with hydrogen peroxide as the final product. The first electron transfer step corresponding to the reduction of O_2 to $O_2^{-\cdot}$ is defined as the rate determining step. No significant changes are found for the nanoparticles here employed: the electron transfer rate constant (k_0) is $k_{0,bulk} = 0.30$ cm $\cdot$ s^{-1} on bulk material and $k_{0,nano} = 0.21$ cm$\cdot$ s^{-1} on

nanoparticles; transfer coefficient(α) changes from 0.45 at the macro-scale to 0.37 at the nano-scale.

The simulation program used was written and debugged by Dr. Kristopher Ward. The SEM images were obtained by Dr. Kristina Tschulik. Dr. Eduardo Laborda helped with the data interpretation. This work has published as a full paper in *Nanoscale*, [1].

In section 6.2, citrate-capped gold nanoparticles (AuNPs) of 5 nm in diameter are synthesized via wet chemistry approach and deposited on a glassy carbon electrode through electrophoresis. The kinetics of the oxygen reduction reaction (ORR) on the modified electrode is determined quantitatively in oxygen-saturated 0.5 M sulphuric acid solution by modelling the cathode as an array of diffusionally interactive nanoelectrodes. Quantitative analysis of the cyclic voltammetry shows that no apparent ORR electrocatalysis takes place, the kinetics on AuNPs being effectively the same as on bulk gold.

In contrast with the above, strong ORR catalysis is found when Pb^{2+} is added to the oxygen saturated solution or when the modified electrode is cycled in lead alkaline solution such that lead dioxide is repeatedly electrodeposited and stripped off on the nanoparticles. In both cases, the underpotential deposition of lead on the gold nanoparticles is found to be related to the catalysis.

The simulation program for this work was developed by Dr. Kristopher Ward. The SEM and TEM images were obtained by Dr. Kristina Tschulik and Dr. Christine Damm. The XPS spectrum and related data interpretation were carried out by

Dr. Robert G. Palgrave and Dr. Blake J. Plowman. Dr. Eduardo Laborda helped with the data interpretation. This work has published as a full paper in *Physical Chemistry Chemical Physics*, [2].

In the section 6.3, the electron transfer kinetics associated with both the reduction of oxygen to hydrogen peroxide (H_2O_2) and of protons to form hydrogen (H_2) at gold nanoparticles are shown to display strong retardation when studied at citrate capped ultra small (2 nm) gold nanoparticles. Negative nanocatalysis in the hydrogen evolution reaction (HER) is observed and reported for the first time.

The simulation program for this work was developed by Dr. Kristopher R. Ward. The TEM analysis was carried out by Dr. Kristina Tschulik and Dr. Christine Damm. Dr. Eduardo Laborda helped with the data interpretation. This work has published in *Nanoscale*, [3].

6.1 A Kinetic Study of the Oxygen Reduction Reaction at, and Characterization of Electrodeposited Gold Nanoparticles of Diameter Between 17 nm and 40 nm in 0.5 M Sulphuric Acid

6.1.1 Introduction

Nanoparticle-modified electrodes are widely used to improve the working efficiency of sensors and fuel cells [4–7] due to the enhanced effective surface area, mass transport, high control over local environment and possible catalytic properties [6]. Thus, changes of electroactivity can be expected considering that nanoparticles *may* have altered electronic properties [8–10], surface structures [8, 9] and electron transfer kinetics with respect to the bulk material depending on their size. For example, there is a dramatic decrease of (111) facets in gold nanoparticles with size below 3 nm, whereas for particles with size bigger than 10 nm, the (111) facets are found to be predominant [8]. White *et al.* [9] have also suggested that there is a decrease of the density of states from bulk gold to gold nanoparticles.

The above changes at the nanoscale can lead to different electrochemical behaviour on nanosized materials; so-called "nanoeffects". Electrocatalytic effects caused by noble metallic nanoparticles such as platinum [11, 12], gold [13, 14] and

palladium [15] have been extensively studied. These refer to an enhanced electrochemical behaviour giving rise to the decrease of the signal overpotential and increase of its magnitude. However, the corresponding changes in mass transport also have to be considered when investigating electrocatalytic effects at the nanoscale because the diffusion field will change at nanoparticle-modified electrodes compare to bulk material. For example, apparent electrocatalytic effects can be caused by thin-layer diffusion on porous film electrodes, where the electroactive species is trapped within pores on the electrode surface leading to the decrease of the overpotential of the voltammograms [16–18].

Table 6.1: Electrodeposition of gold nanoparticles on glassy carbon (GCE), indium tin oxide (ITO), highly ordered pyrolytic graphite (HOPG) and fluorine-doped tin oxide (FDTO) electrodes.

Size/nm	Method	Substrate	Additives	Ref.
32	Double-pulse Electrodeposition	FDTO	no	[19]
5-20	Single-pulse Electrodeposition	GCE	no	[20]
10-24	Electrodeposition	–	20 g/ dm^3 PVP + 2.5 g/ dm^3 SDBS	[21]
30	Potential-step Electrolysis	GCE and HOPG	0.1 mM I^{-1}	[22]
27 ± 16	Cyclic Voltammetry	GCE	no	[23]
22 ± 9	Single-pulse Electrodeposition	ITO	0.125 mM L-cysteine	[24]

Wet chemistry synthesis [25] and electrodeposition (Table 6.1 [19–28]) are two

commonly used methods for the synthesis of nanoparticles. In wet chemistry methods, nanoparticles are usually synthesised through seeding and growing steps. The first seeding process can follow either progressive or instantaneous nucleation [25]. Progressive nucleation leads to broader size distributions because of nucleation and growth happening at the same time, while a more uniform distribution of the particle size is achieved by instantaneous nucleation on a shorter time scale. In the growth step, nanoparticles grow under either kinetic or diffusion control. The size of the nanoparticles under kinetic control conditions has a wider distribution compared to that in the diffusion controlled region [25]. Instantaneous nucleation and diffusion controlled growth is the preferred method to realise a more uniform size of nanoparticles [29, 30].

However, surfactants are usually employed in wet chemistry methods to control the particle size and stabilize nanoparticles. In chapter 5, an effect of cetyl trimethylammonium bromide (CTAB) on the kinetics of electro-oxidation of nitrite and L-ascorbic acid was confirmed on gold and glassy carbon electrodes. Methods for removal of the surfactant can involve change of the surface morphology and loss or aggregation of nanoparticles. Therefore, an electro-deposition method without additives is employed in this chapter to get surfactant free nanoparticles.

A general experimental and simulation approach was developed to investigate the kinetics of electron transfer reactions on nanoparticles [31] (detailed in Chapter 5). Thus, the response of a nanoparticle modified electrode is simulated using the diffusion domain approximation (see chapter 2) and assuming that the particles

are of uniform size and evenly distributed on the substrate surface. By fitting the experimental results with the mechanism determined for the bulk material, it is possible to obtain the kinetics on nanoparticles. This approach was applied to two different systems: the electro-oxidation of nitrite, where authentic catalysis was thought not to occur, and the electro-oxidation of L-ascorbic acid, which shows authentic nanocatalysis as discussed in Chapter 5.

In this section, the above strategy will be extended to the study of the oxygen reduction reaction (ORR). This has a very significant importance in biological process and energy transformation, especially in fuel cells [4]. Direct electrodeposition is employed in order to get surfactant free gold nanoparticles with adjustment of the optimum conditions (concentration of gold salt, deposition time and potential) to control the size and number density of the nanoparticles. The ORR kinetics is studied at the resulting modified electrode where, under the conditions of the present study, there is a negligible contribution from the supporting electrode, which provides a "clean window" for the study of the kinetics on nanoparticles. The absence of a distorting effect due to the capping agent or substrate enables an accurate and representative study of the kinetics on gold nanoparticles. Comparison are made with the same process on gold macro electrodes.

6.1.2 Experimental

6.1.2.1 Chemical Reagents

Sulphuric acid (H_2SO_4, Fisher, >95%), gold (III) chloride trihydrate ($HAuCl_4 \cdot 3H_2O$, Sigma-Aldrich, >99%), hydrochloric acid (Sigma-Aldrich, >37%), lead(II) nitrite (Sigma-Aldrich, >99.5%), sodium hydroxide (Sigma-Aldrich, >97%) were all used as received, without further purification. All the solutions were prepared using deionised water with a resistivity of 18.2 MΩ cm (25 °C).

6.1.2.2 Instrumental

All electrochemical experiments were performed using a three-electrode system with an Autolab PGStat 20 computer-controlled potentiostat (Eco-Chemie, Utrecht, Netherlands). A platinum wire was employed as counter electrode and a saturated calomel electrode (SCE, Radiometer, Copenhagen) was used as reference electrode. A bare or modified glassy carbon electrode (GCE, 3 mm diameter, BAS, Technical, UK) or a bare gold electrode (2mm diameter, BAS, Technical, UK) were employed as working electrodes. The glassy carbon electrode was polished using 3.0, 1.0 and 0.1 μm diamond spray (Kenet, Kent,UK) and the gold electrode was polished with a decreasing size of 1.0, 0.3, 0.05 μm alumina lapping compounds (Bucher, Germany). All electrodes were sonicated in an ultrasound bath prior to use. Scanning Electron Microscope (SEM) images were obtained on a LEO Gemini 1530 (Zeiss) using an in-lens detector and a beam voltage of 5 kV. This was undertaken by Dr. Kristina

Tschulik.

6.1.3 Results and Discussion

6.1.3.1 Characterization of Gold Nanoparticles on Glassy Carbon Electrodes

The characterization of Au-NPs/GCE was performed by the electrochemical method [31, 32] introduced in section 4.2 as well as by Scanning Electron Microscopy (SEM). Regarding the electrochemical characterization, lead underpotential deposition (UPD) on gold nanoparticles [33] and subsequent anodic stripping of gold in hydrochloric acid [34] were employed to determine the total surface area and amount of gold, respectively, as discussed earlier in chapter 4. Lead UPD in alkaline solution has proved to be an effective method for estimating the surface area and morphology of gold nanoparticles [31–33]. A typical cyclic voltammogram of a gold nanoparticle modified glassy carbon electrode(solid line) and bare glassy carbon (dashed line) in the presence of 0.1 mM $Pb(NO_3)_2$ with 0.1 M NaOH is shown in Figure 6.1. As reported by Hernandez *et al.* [33], the sharp peak at around -0.56 V (*vs SCE*) is assigned to the stripping of lead on the Au(111) crystal plane with a charge transfer per atom of 380 μC / cm^{-2} [33]. Au(100) and Au(110) crystal planes contribute to the broad peak that appears at around -0.39 V (*vs SCE*). The associated charge is 340 μC / cm^{-2} [33] for Au(100) plane and 330 μC / cm^{-2} [33] for Au(110) plane.

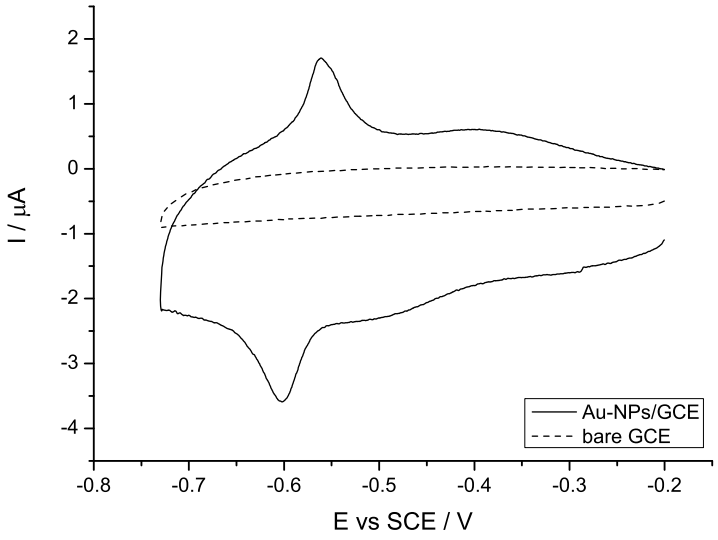


Figure 6.1: Cyclic voltammogram of underpotential deposition of lead on gold nanoparticles modified glassy carbon electrode(solid line) and bare glassy carbon electrode(dashed line) in 0.1 mM $PbNO_3$ and 0.1 M NaOH, 50 mVs^{-1}.

The amount of electrodeposited gold nanoparticles was determined from anodic stripping of Au-NPs/GCE in 0.1 M HCl. As discussed before, at the macro scale, the soluble complexes $AuCl_2^-$ and $AuCl_4^-$ will be formed during the oxidation process of gold in 0.1 M HCl. Our group extended this study into the nanoscale and found that the charge in the stripping process is related to the loading of gold nanoaprticles with a value of 1.9 electrons transfer per gold atom [34]. Figure 6.2 shows the anodic stripping of gold nanoparticles-modified glassy carbon electrode in 0.1 M hydrochloric acid. Normally three scans is sufficient to strip off all the gold nanoparticles. Thus, by combining the results from lead UPD and anodic stripping, and assuming that the nanoparticles are hemispherical, the number and size of particles can be

calculated from the following expressions:

$$\mathrm{S} = x\pi \mathrm{r}^2 \times \mathrm{N} \tag{6.1}$$

$$\mathrm{Q} = 1.9 \times \mathrm{e} \times \mathrm{N_A} \times \mathrm{N} \times \frac{\frac{x}{3} \times \pi \mathrm{r}^3 \rho}{\mathrm{M}} \tag{6.2}$$

where, x=2 for hemispherical and x=4 for spherical nanoparticles, e is the electron transfer charge, r is the average radius of nanoparticles, N is the number of particles, ρ is the density of gold, M is the molar mass of gold and N_A is the Avogadro constant.

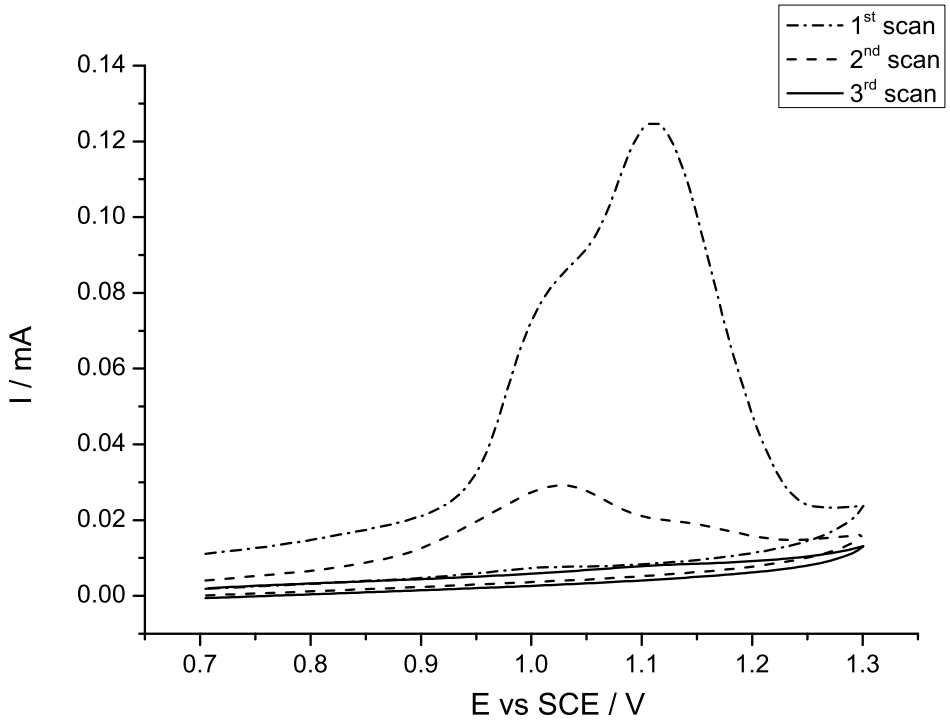


Figure 6.2: Anodic stripping of a gold nanoparticle modified glassy carbon electrode in 0.1 M HCl, 100 mVs^{-1}.

SEM has also been employed in the present study to evaluate the size and dis-

tribution of gold nanoparticles on the glassy carbon electrode. The SEM image (obtained by Dr. Kristina Tschulik) in Figure 6.3 shows the glassy carbon surface after electrodeposition for 30 s at -0.2 V (*vs SCE*) in 0.1 mM $HAuCl_4$ solution.

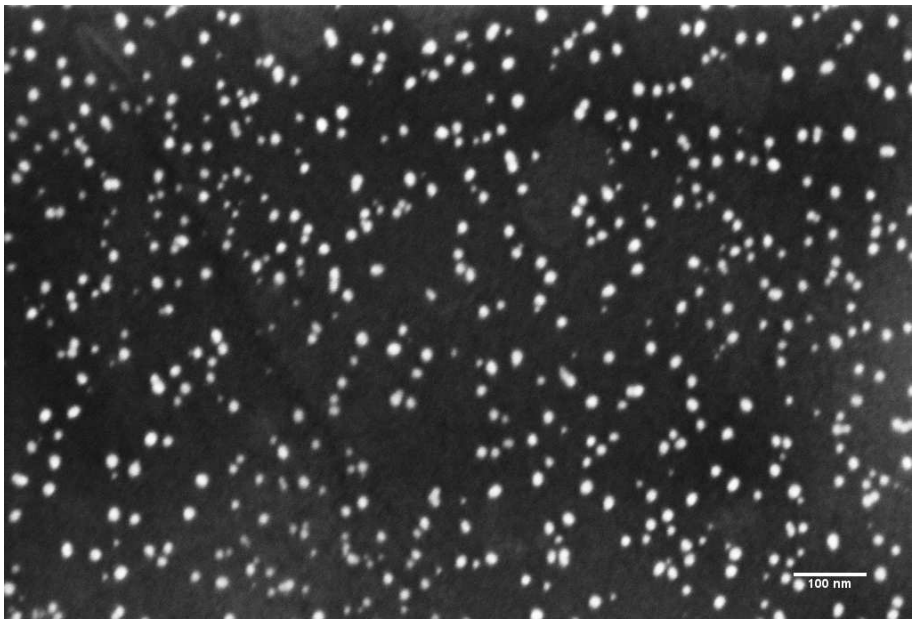


Figure 6.3: Scanning electron microscope of glassy carbon surface after electrodeposition at -0.2 V (*vs SCE*) in 0.1 mM $HAuCl_4$ for 30 s

The SEM images obtained were analysed with ImageJ software (1.47, National Institutes of Health, USA). The results show gold nanoparticles of rounded shape, reasonably evenly distributed on the glassy carbon surface, and with a diameter of 24 ± 9 nm and a total coverage($=100 \times \pi r^2/A$ where A is the glassy carbon area) of $8.4 \pm 0.7\%$. The electrochemical characterization for Au-NPs/GCE under the same deposition conditions yields a particle diameter of 35 ± 10 nm; moreover, assuming that the particles are hemispherical, the coverage determined is of $8 \pm 1\%$. These values agree acceptably well with the SEM ones, especially in terms of coverage that is the factor that predominantly defines the electrochemical response in the

conditions of the present study, that is, *case 4* of diffusional behaviour to an array of nanoparticles [35]. Case four diffusion is described in chapter 2.

6.1.3.2 The Electrodepostion of Gold Nanoparticles on Glassy Carbon Electrodes

A high density nanoparticle-modified electrode was prepared by electrodeposition [19]. In this method, the seeding and the growing laws of wet chemistry method still operate but there is another variable in the growing procedure, that is, the "Inter Diffusion Coupling" (IDC). Deposition at large overpotentials promotes instantaneous nucleation [19] and therefore small particle seeds. If a subsequent growing pulse is applied, IDC is found to be the main factor determining the distribution of particle size [19, 25]. The depletion layer of neighbouring nanoparticles overlaps and, therefore, the size of the nanoparticles strongly depends on the distance and distribution of its neighbours. Providing the process is under diffusion control, Plieth [36] and Penner [25] found that the influence of IDC is negligible in the electrochemical kinetic controlled region. Forster *et al.* [19] controlled particle sizes by a double-pulse technique. A first pulse was applied at large overpotentials to generate small seeds followed by a second pulse in the kinetic control region to realise slow growth avoiding the generation of more seeds as well as IDC. In the present paper, only the first seeding pulse is applied in order to get smaller nanoparticles.

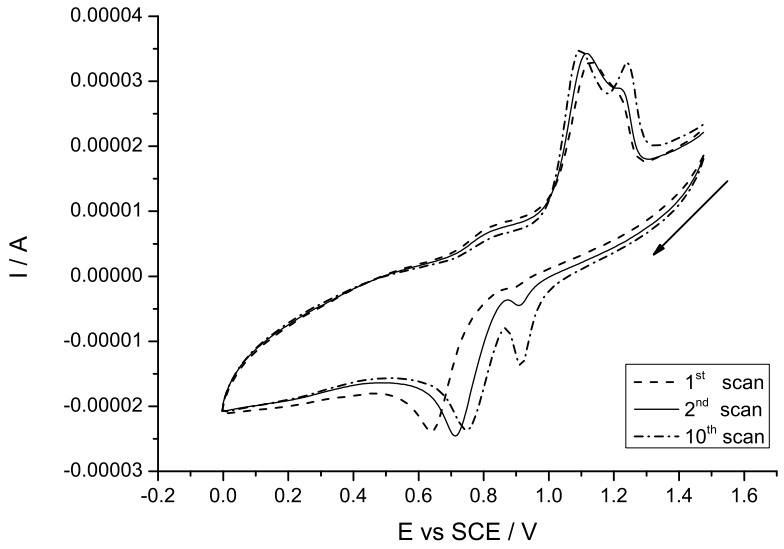


Figure 6.4: Cyclic Voltammograms of bare macro glassy carbon electrode in nitrogen saturated 0.5 mM $HAuCl_4$ and 0.5 M sulphuric acid solution at 298 K and 100 mVs^{-1} : 1^{st} (dash line) ; 2^{nd} (solid line) ; 10^{th} scan (dash dot line)

Figure 6.4 depicts cyclic voltammograms of electroreduction of $HAuCl_4$ on a bare glassy carbon electrode in 0.5 M H_2SO_4 containing 0.5 mM $HAuCl_4$. As can be seen, in the first reduction scan gold deposition on glassy carbon happens at around 0.64 V (vs SCE), the deposition peak shifting to lower overpotentials for about 70 mV in the second scan and finally stabilizing at 0.75V (vs SCE). This decrease in overpotential in subsequent scans shows that electrodeposition on gold deposit is more favourable than on carbon [19, 23, 26, 28]. The small reduction peak increased with scans at around +0.89 V (vs SCE) and may be related to the reduction of gold oxides formed in the reverse oxidation process in the repetitive scan [37]. Reflecting these results, deposition potentials between -0.2V and -0.5V were chosen in the following studies to get instantaneous nucleation.

Table 6.2: Electrodeposition of $HAuCl_4$ in nitrogen saturated 0.5 M H_2SO_4 at 293.15 K : Influence of deposition time; surface coverage by nanoparticles (Θ) in the table is defined as: $\Theta = \frac{N\pi r^2}{A} \times 100$, where, where N is the number of particles, r is the radius of a single nanoparticle and A is the area of the GC substrate.Error bars calculated from 3-20 experimental measurements.

c / mM	Deposition potential / V (*vs* SCE)	t / s	d / nm	Θ / %
0.1	-0.20	30	35±10	8±1
		10	30±1	6.8±0.4
		0.05	36±1	3.8±0.1

Table 6.3: Electrodeposition of $HAuCl_4$ in nitrogen saturated 0.5 M H_2SO_4 at 293.15 K : Influence of concentration of $HAuCl_4$, surface coverage calculated as indicated above in Table 6.2.

t / s	Deposition potential / V (*vs* SCE)	c / mM	d / nm	Θ / %
30	-0.20	0.10	35±10	8±1
		0.05	24±3	3.7±0.6
2	-0.20	0.50	59±2	9.0±0.2
		0.25	47±2	8.1±0.5
		0.10	44±8	3.8±0.5
0.5	-0.50	0.50	43±2	8.2±0.4
		0.30	35±2	10.8±0.1

Table 6.4: Electrodeposition of $HAuCl_4$ in nitrogen saturated 0.5 M H_2SO_4 at 293.15 K : Influence of deposition potential, surface coverage calculated as indicated above in Table 6.2

t / s	c / mM	Deposition potential / V (*vs* SCE)	d / nm	Θ / %
30	0.10	-0.20	35±10	8±1
		-0.50	18±3	10±1
10	0.10	-0.20	29±1	6.8±0.4
10		-0.35	21±3	6.6±0.3
8		-0.40	21±2	7±2
7		-0.50	22±2	8±1

Besides the deposition potential, the $AuCl_4^-$ anion concentration and the deposition time are the other two main variables in single pulse electrodeposition. Tables 6.2 - 6.4 show the correlations between particle size and coverage with these three variables. Regarding the effect of deposition time, the results in Table 6.2 show that the influence on the particle number is more significant than on the average size. Thus, the particle size does not change significantly for deposition times between 30 s and 0.05 s while the coverage changes from 8 % to 4 %. Accordingly, increasing deposition time will lead to a major effect on the number density of nanoparticles but not the size of nanoparticles. Tables 6.3 and 6.4 demonstrate that both concentration and potential are critical in controlling particle size and numbers. A slight decrease of size happens when concentration drops. However, concentration can only decrease particle size to a certain extent. A more significant decrease of particle size is achieved by increasing the overpotential which provides a large driving force for deposition. In Table 6.4 particle sizes smaller than 20 nm are gained with a deposition potential around -0.5 V (*vs SCE*). Deposition potentials more negative than -0.6 V were avoided due to hydrogen discharge. In conclusion, small gold concentrations and large overpotentials are used for the synthesis of small nanoparticles.

6.1.3.3 Kinetic Studies of the ORR on a Polycrystalline Bulk Gold Electrode

The Oxygen reduction reaction (ORR) on metal electrode surfaces has been in the spot-light for several decades [38–54]. A number of mechanisms for ORR in acid

media have been proposed and are still under debate [45, 53, 54]. A sequential pathway including two electron transfers to hydrogen peroxide or an overall four electron transfer reaction to water have been proposed depending on the solution conditions and electrode materials [44, 45, 53, 54].

On polycrystalline gold electrode in strong acid media, the reduction of oxygen to hydrogen peroxide has been reported [45]. Therefore, the following mechanism is employed in the simulations with the parameters shown in Table 6.6:

$$\mathrm{O_2} + e^- \overset{k_{0,1},E_1^0,\alpha_1}{\leftrightharpoons} \mathrm{O_2^{-\cdot}} \tag{6.3}$$

$$\mathrm{O_2^{-\cdot}} + \mathrm{H^+} \overset{K_{eq1},k_{f1}}{\leftrightharpoons} \mathrm{HO_2^{\cdot}} \tag{6.4}$$

$$\mathrm{HO_2^{\cdot}} + e^- \overset{E_2^0 \gg E_1^0}{\leftrightharpoons} \mathrm{HO_2^-} \tag{6.5}$$

$$\mathrm{HO_2^-} + \mathrm{H^+} \overset{K_{eq2},k_{f2}}{\leftrightharpoons} \mathrm{H_2O_2} \tag{6.6}$$

where, k_{0i} is the electron transfer rate constant for step i; α_i the transfer coefficient; E_i^0 the formal potential; K_{eqi} the equilibrium constant and k_{fi} the forward rate constant.

The first electron transfer (Eq.6.3) leading to the formation of the superoxide ion is thought to be the rate determining step (RDS) regardless of the electrode material and medium. In the following, this is confirmed via Tafel analysis. At low pH [45], this reaction is followed by fast protonation (step 6.4) and a further fully driven electron transfer step as shown in Eq. 6.5. The final product, hydrogen peroxide,

is formed by rapid protonation of HO_2^-. Gold has been acknowledged as having the least adsorption of the noble metals for oxygen species, although adsorption of intermediates, such as O_2^- and $HO_2^{\cdot}$, may still happen [45, 48, 50, 53] and there may be changes in this respect between macro and nano gold.

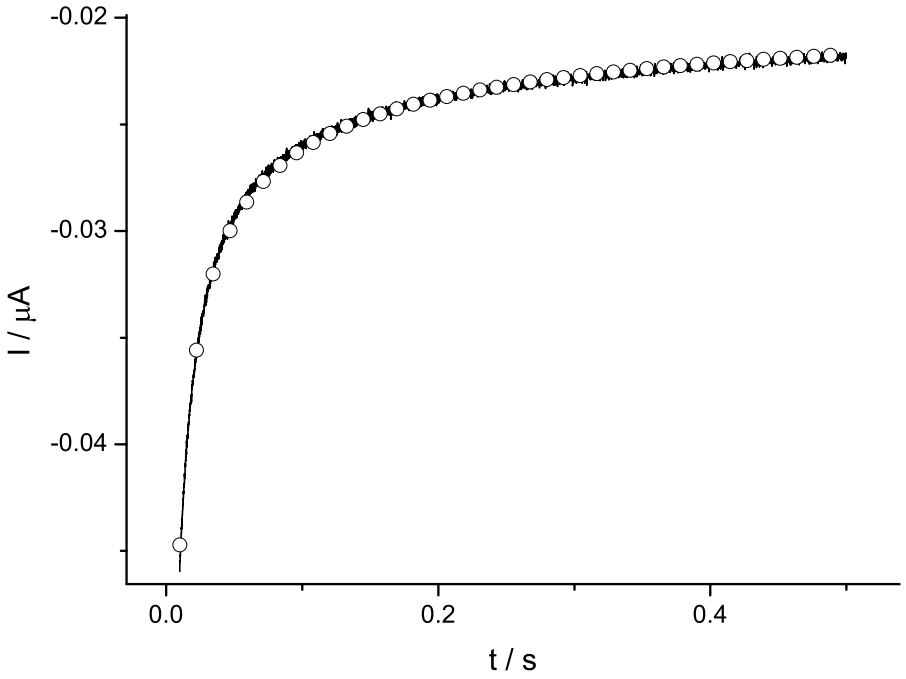


Figure 6.5: Determination of diffusion coefficient and concentration of oxygen in oxygen saturated 0.5 M sulphuric acid solution at 298 K by Shoup and Szabo equation. Open circle is for simulation and solid line is for experiment.

In this chapter, kinetic studies of ORR on polycrystalline bulk gold electrode are reported in oxygen saturated 0.5 M sulfuric acid solution at 298 K (pH=0.39). Thermostatic control is essential due to the fact that the solubility, diffusion coefficient and electron transfer kinetics are temperature sensitive. Determination of diffusion coefficient and concentration are completed on a gold microelectrode ($r_o = 13$ μm)

via potential step chronoamperometry through the Shoup and Szabo equation (Figure 6.5) [55]. The values obtained for the diffusion coefficient and concentration are $(1.26 \pm 0.03) \times 10^{-5}$ cm$^2 \cdot$ s^{-1} and 1.43 ± 0.02 mM, respectively, which are in good agreement with the literature [56].

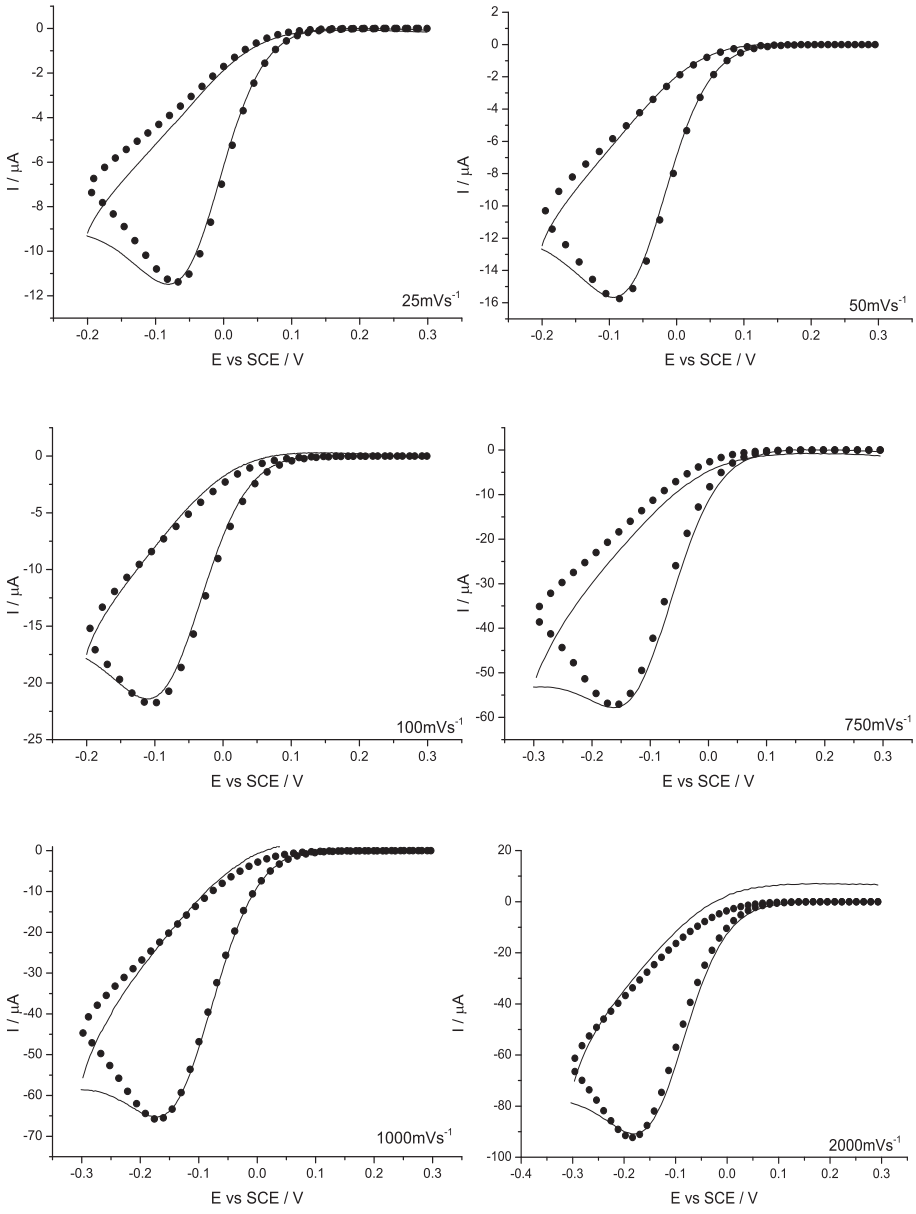


Figure 6.6: Simulated (circle) and experimental (solid line) voltammograms on macro gold electrode in oxygen saturated 0.5 M sulphuric acid solution at 298 K from 25 mVs^{-1} to 2000 mVs^{-1}

The kinetics of the ORR on polycrystalline bulk gold electrode in strong acid media is reported in Table 6.6 based on the mechanism proposed by Eqs. 6.3 - 6.6. The satisfactory fitting between the experimental (solid line) and simulated (dashed line) voltammograms over a wide range of scan rates from 25 mVs^{-1} to 2000 mVs^{-1} in Figure 6.6 suggest the validity of the mechanism proposed. The homogeneous kinetics for steps 6.4 and 6.6 are widely reported [39]. Superoxide ion will protonate rapidly once after it is formed. Kastening and Divisek suggested step two (Eq. 6.4) to be diffusion-limited and the acid dissociation constant $pK_a = 4.88$ for $HO_2^{\cdot}$ [39]. The homogeneous reaction Eq. 6.6 is also a fast protonation step (diffusion-limited) with $pK_a = 11.62$ for hydrogen peroxide [57], so HO_2^- is consumed immediately. Moreover, considering the formal potential value of the redox couple $HO_2^{\cdot}/HO_2^-$ (see Table 6.6), it is expected that step 6.5 is fully driven, that is, $HO_2^{\cdot}$ is immediately reduced to HO_2^-.

Based on all the discussion above, the kinetics of step 6.3 determines the rate of the overall reaction. The standard redox potential for the couple $O_2/O_2^{-\cdot}$ [38] has been determined to be -0.21 V (vs SCE) and more negative values for the formal potential of up to -0.434 V(vs SCE) [41] (Table 6.5) have been reported by different means such as thermodynamic calculations and electrochemical measurements. Using $E^0_{O_2/O_2^{-\cdot}}$, α_1 and $k_{0,1}$, as fitting parameters, the values $E^0_{O_2/O_2^{-\cdot}} = -0.298$ V (vs SCE), $\alpha_1 = 0.45$ and $k_{0,1} = 0.30$ $cm{\cdot}s^{-1}$ correspond to the best fitting of the voltammograms from 25 mVs^{-1} to 2000 mVs^{-1} shown in Figure 6.6. Note that the α value relates to the single step defined by Eq. 6.3. Figure. 6.7 shows voltammograms for

the ORR on Au-NPs/GCE (solid line) and bare GCE (dash line) in oxygen saturated 0.5M sulphuric acid at 100 mVs^{-1} and 298 K. As can be seen, the response from GCE is almost negligible in the range where ORR happens on Au-NPs/GCE. This allows a more accurate study of the kinetics onthe gold nanoparticles.

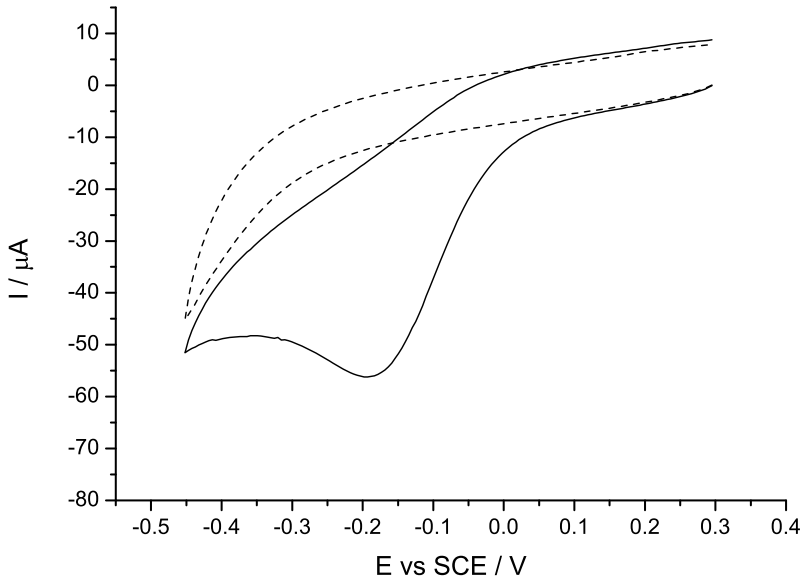


Figure 6.7: ORR on bare glassy carbon electrode (dashed line) and 8 % Au-NPs/GCE (solid line) in 0.5 M sulphuric acid solution in 298 K at 100 mVs^{-1}.

Table 6.5: Literature value of $E^0_{O_2/O_2^{-\cdot}}$ in aqueous solution

$E^0_{O_2/O_2^{-\cdot}}$ /V(*vs* SCE)	Methods	Ref
-0.210	Thermodynamic calculation (Standard electrode potential)	[38]
-0.358	Tafel plot	[39]
-0.399	Pulse radiolysis	[40]
-0.434	Thermodynamic calculation	[41]
-0.355	Tafel plot	[42]
-0.424	Thermodynamic calculation	[43]

6.1.3.4 Kinetic studies of the ORR on Au-NPs/GCE

In the section 6.1.3.3, the kinetic and mechanistic study on bulk gold was reported. The next stage is to investigate the ORR kinetics on gold nanoparticles under the same experimental conditions. Au-NPs/GCE are prepared following the electrodeposition method discussed in section 6.1.3.2. The coverage and size of nanoparticles for each particular Au-NPs/GCE are obtained by the electrochemical characterization method discussed in the chapter 4 and the section 6.1.3.1 immediately after investigation of oxygen reduction. Note that all the studies are based on the first voltammograms with freshly prepared Au-NPs/GCE. Subsequent scans were found to yield irreproducible results that may be due to the poisoning of gold surface. Conventional cleaning methods of gold macro electrode with repetitive scans in nitrogen saturated sulfuric acid have been found to promote defects and alter the morphology of gold nanoparticles [58]. Moreover, repetitive scans of Au-NPs/GCE in sulphuric acid can lead to detachment of nanoparticles [58, 59].

A simulation program was developed by Dr. Kristopher Ward under the assumption of diffusion domain approximation together with hemi-spherical nanoparticles of uniform size and evenly distributed on the substrate as detailed in [31, 60]. The influence of different shape and size on the voltammograms has been investigated prior to the study. Comparison of simulated voltammograms of nanoparticles of different size with spherical, hemispherical and disk shapes showed negligible divergence for the conditions of this study, the response being defined almost exclusively

by the nanoparticle coverage.

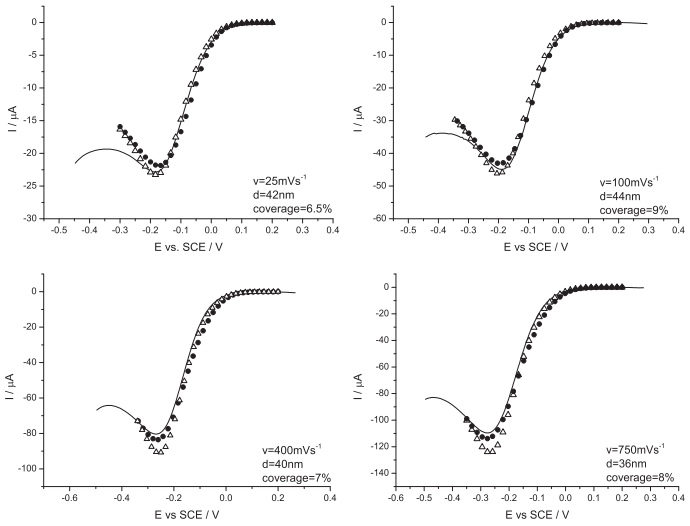


Figure 6.8: Comparison of experiment (black solid line), simulation with kinetics obtained from macro gold electrode (open triangle) and simulation with changed kinetics for gold nanoparticles nanoparticles (solid circle) for ORR on 40 nm Au-NPs/GCE in oxygen saturated 0.5 M sulphuric acid solution at 298 K from 25 mVs^{-1} to 750 mVs^{-1}.

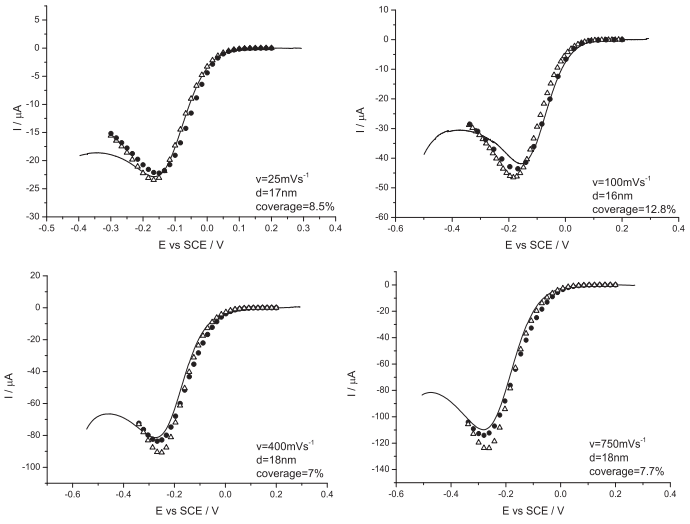


Figure 6.9: Comparison of experiment (black solid line), simulation with kinetics obtained from macro gold electrode (open triangle) and simulation with kinetics for gold nanoparticles nanoparticles (solid circle) about ORR on 17 nm Au-NPs/GCE for oxygen saturated 0.5 M sulphuric acid solution at 298 K from 25 mVs^{-1} to 750 mVs^{-1}.

There are two steps in the following study of the ORR kinetics on gold nanoparticles. The first is to identify whether there is a kinetic change with respect to the bulk material. If so, the second step is to obtain the new kinetics from fitting. The ORR response were recorded on nanoparticles of diameter from 17 nm to 40 nm with coverage from 6.5% to 12.8%. It is worth pointing out that, for suitable simulation, very high coverage should be avoided to prevent the formation of porous films on the electrode. Meanwhile, very low coverage is not preferred because the voltammograms will have a predominant contribution from the glassy carbon substrate. Comparison of experimental voltammograms (solid line) and simulation (open triangle) considering the coverage for nanoparticles and kinetics from bulk gold are shown in Figure 6.8 (40 nm) and Figure 6.9 (17 nm). It can be inferred that the fitting of the peak current is worse with the increasing of the scan rate. Simulated voltammograms with new kinetics (solid circle) are shown in Figure 6.8 and Figure 6.9 from 25 mVs^{-1} to 750 mVs^{-1}. Considering the whole range of scan rates, a higher quality fitting is achieved with the best fit parameters shown in Table 6.6. Figure 6.10 shows the correlation of the experimental (open square) and simulated (solid square) peak potentials against natural logarithm of scan rate for a similar coverage (8 %). A good linearity ($R^2 = 0.997$) is obtained for experimental data, and these are well fitted with the simulation. In Figure 6.11, peak current is plotted as a function of square root of scan rate. A good agreement of experimental and simulated results can be seen. The experimental value $\alpha_{exp} = 0.36$ calculated from the slope of I_p *vs.*$\sqrt{\nu}$ in Figure 6.11 agrees with the value employed in the simulation

of $\alpha_{sim} = 0.37$.

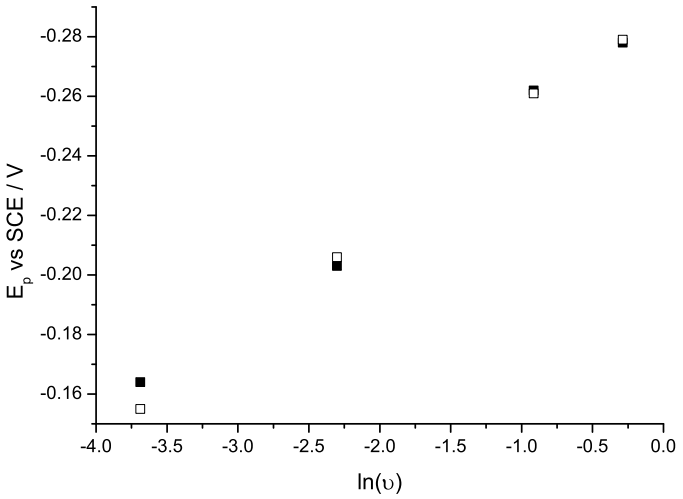


Figure 6.10: Comparison of peak potential of ORR on Au-NPs/GCE in 0.5 M sulphuric acid at 298 K from 25 mVs^{-1} to 750 mVs^{-1} from experiment (solid square) and best fit simulation (open square) with respect to natural logarithm of scan rates.

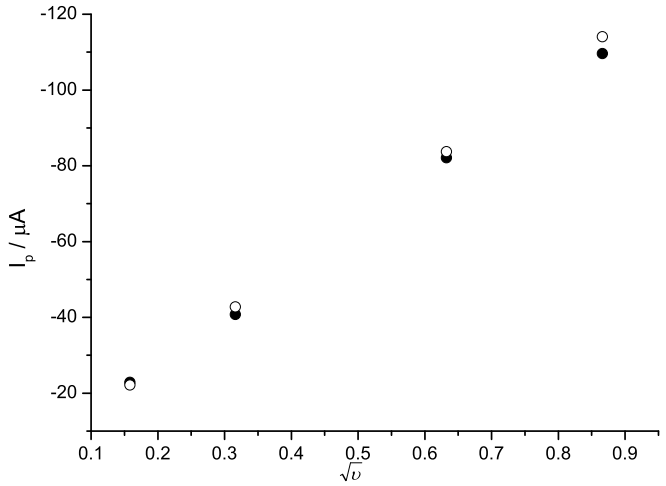


Figure 6.11: Comparison of peak potential of ORR on Au-NPs/GCE in 0.5 M sulphuric acid at 298 K from 25 mVs^{-1} to 750 mVs^{-1} from experiment (solid circle) and best fit simulation (open circle) against square root of scan rates.

Table 6.6: Summary of kinetics of ORR in 0.5 M sulphuric acid at 298 K on gold macro electrode and gold nanoparticles modified glassy carbon electrode

	Gold macro electrode	Au-NPs/GCE
step 1	$k_{0,1}$=0.30 cm· s^{-1} (this work) $E_1^0 = -0.298$ V(*vs* SCE)(this work) $\alpha_1 = 0.45$(this work)	$k_{0,1}$=0.21 cm·s^{-1} (this work) $E_1^0 = -0.298$ V(*vs* SCE)(this work) $\alpha_1 = 0.37$(this work)
step 2	pKa_{HO_2} =4.88[39]	pKa_{HO_2} =4.88[39]
step 3	E_2^0=1.19 V(*vs* SCE)[61]	E_2^0=1.19 V(*vs* SCE)[61]
step 4	$pKa_{H_2O_2}$ =11.62[57]	$pKa_{H_2O_2}$ =11.62[57]

The electrode kinetics on nanoparticles of diameter from 17 nm to 40 nm have been summarized in Table 6.6 based on the fitting of voltammograms measured at the scan rates from 25 mVs^{-1} to 750 mVs^{-1}. The transfer coefficient (α) changes from 0.45 on the bulk material to 0.37 at the nanoscale. Adźić [52] revealed that ORR shows different transfer coefficient (α) at different crystalline planes:$\alpha_{(100)}$ = 0.49, $\alpha_{(111)} = 0.34$ and $\alpha_{(110)} = 0.49$. Therefore, the change of α here may be related to the different domains of crystalline planes on the nanoparticles. Regarding the rate constant of electron transfer (k_o), this is slightly smaller on nanoparticles of diameter from 17 nm to 40 nm (0.21 cm·s^{-1}) compared to gold macro electrode (0.30 cm·s^{-1}). However, comparing the kinetics on bulk material and nano particles (see Table 6.6), one can infer that the change is not significant. Extraordinary electrocatalytic effects has been reported on gold nanoparticles smaller than 3-5 nm, for example, for the electro-oxidation of carbon monoxide [62] and oxygen reduction

reaction [63].

6.1.4 Conclusions

In this section, kinetic and mechanistic studies of oxygen reduction reaction (ORR) on gold macro electrode and electrodeposited gold nanoparticles of diameter from 17 nm to 40 nm modified glassy carbon electrode have been completed in oxygen saturated 0.5 M sulphuric acid solution at 298 K. An overall ECEC mechanism with two electron, two proton transfers and hydrogen peroxide as final product has found to be consistent with the experimental voltammetry. The first electron transfer step corresponding to the reduction of O_2 to $O_2^{-\cdot}$ is defined as the rate determining step. For this, the kinetics on gold macro electrode is obtained through the fitting of cyclic voltammetry in the range of 25 mVs^{-1} to 2000 mVs^{-1}: $E^0_{O_2/O_2^{-\cdot}} = -0.298$ V (vs SCE), $\alpha_{bulk} = 0.45$ and $k_{0,bulk} = 0.30$ $cm{\cdot}s^{-1}$. Although these kinetic parameters do not enable to fit satisfactorily of the voltammetry on nanoparticles, the change of kinetics at nano-scale is not significant, obtaining the following values: $\alpha_{nano} = 0.37$ and $k_{0,nano} = 0.21$ $cm{\cdot}s^{-1}$.

The electrochemical behaviour for the ORR system of electrodeposited gold nanoparticles of size between 17 nm and 40 nm is not significantly different from that on the bulk material. The small change of electrode kinetics from macro to nano scale may indicate that gold nanoparticles in the range of diameter from 17 nm to 40 nm are not small enough to observe apparent nanoeffects. Therefore, it will be of interest to extend the strategy to the study of the electrocatalytic activity

of smaller gold nanoparticles, where more significant change of properties (surface site domain and electronic properties) are expected. This is adressed in section 6.2 and section 6.3.

6.2 The Strong Catalytic Effect of Pb(II) on the Oxygen Reduction Reaction on 5 nm Gold Nanoparticles

6.2.1 Introduction

The high overpotential of the oxygen reduction reaction (ORR) is one of the main performance limiting factors for energy conversion in fuel cells. Accordingly, much effort is being made in the development of new cathode materials with the aim of increasing the efficiency and lowering the cost of the corresponding large-scale technologies.

As presented in the section 6.1, nanocatalysis is not observed for on electrodeposited gold nanoparticles of diameter between 17 nm and 40 nm for ORR in 0.5 M sulphuric acid solution [1].

In this section, the study is extended to smaller gold nanoparticles, where differences between the properties at the macro- and nanoscales are expected to be more apparent, for the ORR under the same conditions in the previous section.

A smaller particle size is reached (*ca.* 5 nm in diameter) *via* solution-phase

chemical reduction of a gold(III) salt and, subsequently, nanoparticles are deposited on glassy carbon electrodes through electrophoresis. Assuming that the reaction mechanism is the same as introduced before [1] in Eq. 6.3 - Eq. 6.6, the ORR kinetics on gold nanoparticles in sulfuric acid medium is determined and compared with gold macroelectrodes.

In addition, different catalytic activities are observed between the particles before and after a surfactant-removal treatment based on lead oxide deposition-stripping [64, 65]. Thus, whereas the "uncleaned" nanoparticles do not show a significant change in ORR kinetics with respect to bulk gold, significant electrocatalysis is observed after the cycling in lead alkaline solution. The origin of the "activation" of the gold particles after the "cleaning" treatment is investigated and found to be related to the enhanced ORR kinetics by the bimetallic Pb-Au surface.

6.2.2 Experimental

6.2.2.1 Chemical Reagents

Sulphuric acid (H_2SO_4, Fisher, >95%), gold (III) chloride trihydrate ($HAuCl_4 \cdot 3H_2O$, Sigma-Aldrich, >99%), hydrochloric acid (Sigma-Aldrich, >37%), lead(II) nitrite (Sigma-Aldrich, >99.5%), sodium hydroxide (Sigma-Aldrich, >97%), sodium borohydride (>98%) and trisodium citrate (>99.0%) were all used as received, without further purification. All the solutions were prepared using deionised water with resistivity of 18.2 MΩ cm (25 °C).

6.2.2.2 Instrumental

The instrumental details for electrochemistry measurements were the same as detailed in the section 6.1.2.2.

X-ray photoelectron spectroscopy (Thermo Scientific K-Alpha) was carried out using a 72 W monochromated Al K alpha source (E =1486.6 eV). The X-rays are microfocused at the source to give a spot size on the sample of 400 microns in diameter. The analyser is a double focusing 180 degree hemisphere with mean radius 125 mm. It is run in constant analyser energy (CAE) mode. The pass energy was set to 200 eV for survey scans and 50 eV for high resolution regions. All XPS spectra were referenced according to the adventitious C 1s peak (285 eV). The spectra were obtained and interpreted by Dr. Robert G. Palgrave and Dr. Blake J. Plowman.

TEM studies were performed using a FEI TECNAI T20 (200 kV/ LaB6- filament/ EDX- Oxford-detector). Diffraction contrast allowed the identification of both facetting of individual and possible agglonmeration of multiple nanoparticles. Nanodiffraction and high resultion images (not shown) confirmed the cubic structure of the analysed Au nanoparticles. Scanning Electron Microscopy (SEM) images were obtained on a LEO Gemini 1530 (Zeiss) using an in-lens detector and a beam voltage of 5 kV. The freshly sonicated Au NP stock suspension was drop-casted onto a carbon coated TEM grid of 3 mm in diameter. SEM images were carried out on uncleaned and "cleaned" Au-NPs/GCE. The adsorption of nanoparticles was characterized with ultraviolet-visible spectroscopy (U-2001 spectrophotometer, HI-

TACHI, UK) from 700 nm to 300 nm at a scan rate of 100 min^{-1} . The SEM and the TEM analysis were carried out by Dr. Kristina Tschulik and Dr. Christine Damm.

6.2.2.3 Modification of Glassy Carbon Electrodes with Gold Nanoparticles

After polishing and sonication (detailed in the section 6.1.2.2), the GCE was transferred into the nanoparticle synthesis solution containing 0.01 M $HAuCl_4$ (0.5 mL), 0.01 M trisodium citrate (0.5 mL), 0.1 M freshly prepared ice-cold $NaBH_4$ (0.6 mL) and 14.4 mL water [31, 66–71]. Under open circuit conditions the sticking of nanoparticles on the glassy carbon surface was found to occur very slowly and so a very low nanoparticle coverage was obtained even after 2 hours. To speed up the modification step, electrophoretic deposition was employed recognising the negatively charged citrate layer on the nanoparticle surface. Therefore, a positive potential of +0.65 V (vs SCE) was applied for 5-10 minutes. This potential value was chosen in order to promote the migration of the citrate capped nanoparticles towards the glassy carbon surface while avoiding gold electrooxidation.

6.2.2.4 "Cleaning" of Gold Nanoparticle Surface

The conditions for the nanoparticle synthesis employed in this work is reported to yield spherical, citrate-capped particles with diameter of *ca.* 4 nm [66–69]. According to previous studies, the electron transfer kinetics can be affected by the capping agent [31]. A commonly-used method to remove the capping agent is by electroox-

idation in sulfuric acid [72] or sodium hydroxide solutions [73]. However, these methods can alter the surface properties of the nanoparticles [58], for instance, as a result of surface reconstruction [37, 74] and an increased number of surface defects [75, 76].

Hernández *et.al* [65] introduced a less aggressive alternative for the removal of organic capping agents from gold nanoparticles based on the electrochemical cycling of the nanoparticles modified-electrode in an alkaline solution of lead nitrate. By scanning towards positive potentials, lead oxides are electrodeposited on the nanoparticle surface that protects the gold surface structure while promoting the oxidation of the capping agent [64, 65]. Prior to ORR experiments gold nanoparticle-modified glassy carbon electrodes were cycled in 1 mM $Pb(NO_3)_2$, 0.1 M NaOH solution from -0.73 V (*vs*. SCE) to +0.5 V with three cycles performed followed by a linear scan from -0.73 V (*vs*. SCE) to 0 V. Following this "cleaning" procedure, the nanostructured electrodes were rinsed by deionised water prior to ORR experiments.

6.2.2.5 Characterization of Gold Nanoparticle-modified Glassy Carbon Electrodes

The characterization of the Au-NPs/GCE surface was carried out by coulometry, X-ray photoelectron spectroscopy (results discussed in section 6.2.3.2) and scanning and transmission electron microscopies.

The diameter of the nanoparticles synthesized according to the method described in section 6.2.2.3 is reported to be *ca*. 4 nm. This is in agreement with the UV-

vis spectrum shown in Figure 6.12 corresponding to a representative NP synthesis solution with a dilution factor of 3 at 298 K. The main absorption peak arising at 507 nm indicates that the size of the synthesized gold nanoparticles is smaller than 5 nm [77, 78].

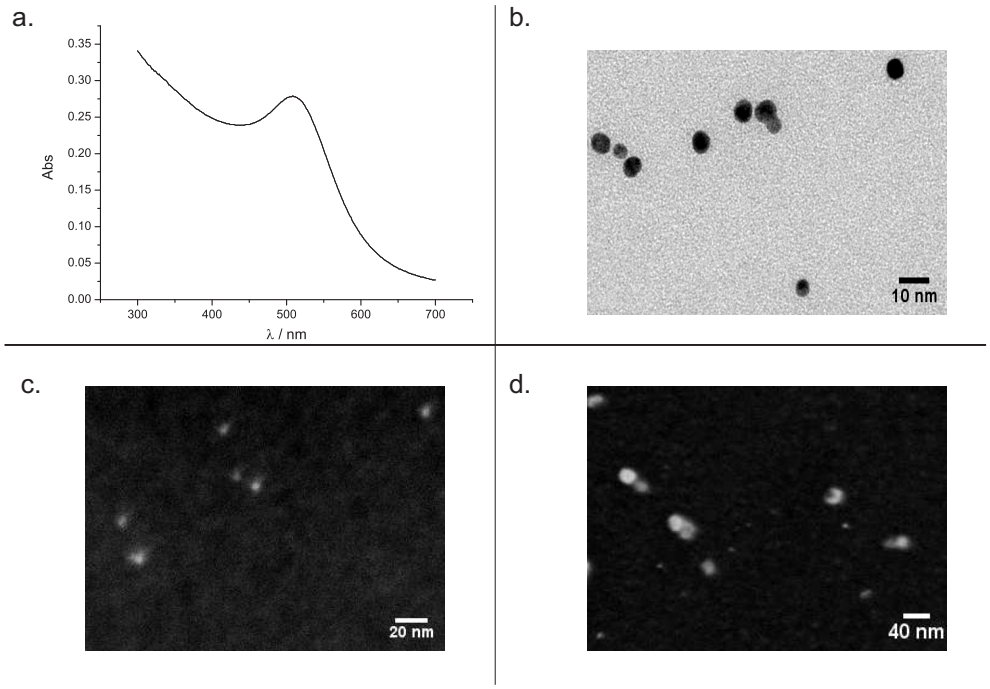


Figure 6.12: Characterization of gold nanoparticles: a. UV-vis spectrum of the synthesis solution with a dilution factor of 3 at 25 °C, b. TEM of gold nanoparticles after synthesis, c. SEM of Au-NPs/GCE before the "cleaning" process, d. SEM of Au-NPs/GCE after the "cleaning" process

The particle size and shape were also investigated by transmission electron microscopy (TEM) and scanning electron microscopy (SEM). As can be seen in Figure 6.12, SEM and TEM images show spherical nanoparticles. The analysis of 8 TEM images including 595 particles with ImageJ software (1.47, National Institutes of Health, USA) yields a diameter of 4.7 ± 0.6 nm.

Regarding the electrochemical characterization, each Au-NPs/GC electrode was

transferred to a hydrochloric acid solution and scanned anodically in order to oxidize the gold nanoparticles (a mean value of 1.9 electrons are transferred per gold atom [34, 79, 80]). Given that the average particle diameter is known (*ca.* 5 nm), the total number of particles (N) is determined from the stripping charge in 0.1 M HCl medium, providing the nanoparticle surface coverage ($=N\,\pi\,r_{NP}^2/A_{GC}$, where r_{NP} is the radius of nanoparticles, A_{GC} the geometric area of the glassy carbon electrode) as required for the simulations. This was done *immediately after* ORR experiments in order to obtain representative results of the electrode surface employed for each experiment and to minimize subsequent alterations due to nanoparticle oxidation and/or detachment.

6.2.2.6 Oxygen Reduction Reaction on Au-NPs/GCE

Studies of oxygen reduction reaction on Au-NPs/GCE were carried out in oxygen saturated 0.5 M sulfuric acid solution at 298 K. For the studies of ORR on "uncleaned" Au-NPs/GCE in the presence of Pb^{2+}, 10 μL of 0.1 M $Pb(NO_3)_2$ was added into 10 mL of oxygen saturated 0.5 M sulfuric acid at 298 K.

6.2.3 Results and Discussion

6.2.3.1 Oxygen Reduction Reaction on "Uncleaned" Au-NPs/GCE

The mechanism of the ORR on metal electrodes has been extensively investigated over many decades [38, 44–46, 81]. The ORR mechanism and kinetics on a polycrystalline gold macroelectrode and nanoparticles (with size from 17 nm to 40 nm)

in strong acid media were presented in section 6.1 [1]. In all cases, the voltammetric response was parameterized satisfactorily for a wide range of scan rates with an ECEC mechanism corresponding to a two-electron, two-proton transfer that leads to hydrogen peroxide as final product shown in Eq. 6.3 - Eq. 6.6. The electron transfer kinetics were obtained on a gold macroelectrode by fitting experimental voltammetry from 25 mVs^{-1} to 2000 mVs^{-1}. No significant change of ORR kinetics was found between bulk gold electrode and gold nanoparticles of size 17 nm to 40 nm [1]. According to the literature, the diffusion coefficient and concentration of oxygen under our experimental conditions (oxygen saturated 0.5 M sulphuric acid solution at 298 K) are 1.26×10^{-5} $cm^2 \cdot s^{-1}$ and 1.43 mM, respectively [1, 56].

Based on the reaction scheme (Eq. 6.3 - Eq. 6.6), the kinetics of the rate determining step of oxygen to superoxide ion (Eq. 6.3) is characterized by comparison of experimental and theoretical voltammograms. The latter are obtained with a home-written simulation program (by Dr. Kristopher R. Ward) [31, 60] which models the nanoparticle-modified surface as an array of evenly-distributed nanoelectrodes of the same size under the assumptions of the diffusion domain approximation [60]. This approach has proven to fully describe the system and has shown good agreement with experiments [1, 31]. Simulations predict that, for the range of surface coverage of this study, the influence of size and shape of the nanoparticles is not primarily significant and the response is almost exclusively defined by the surface coverage. This is determined for each particular Au-NPs/GCE immediately after oxygen electroreduction as described in section 6.2.2.5. All the studies of the ORR kinetics are

based on the first voltammogram recorded for the freshly prepared Au-NPs/GCE.

Figure 6.13 shows the comparison of experimental voltammetry (solid line) of ORR on "uncleaned" Au-NPs/GCE with simulations run with the ORR kinetics on bulk gold (dashed line). The satisfactory fitting of simulation and experimental results indicates that there is no significant change between the kinetics on gold macroelectrodes and citrate-capped 5 nm Au-NPs for the ORR system are shown in Table 6.7.

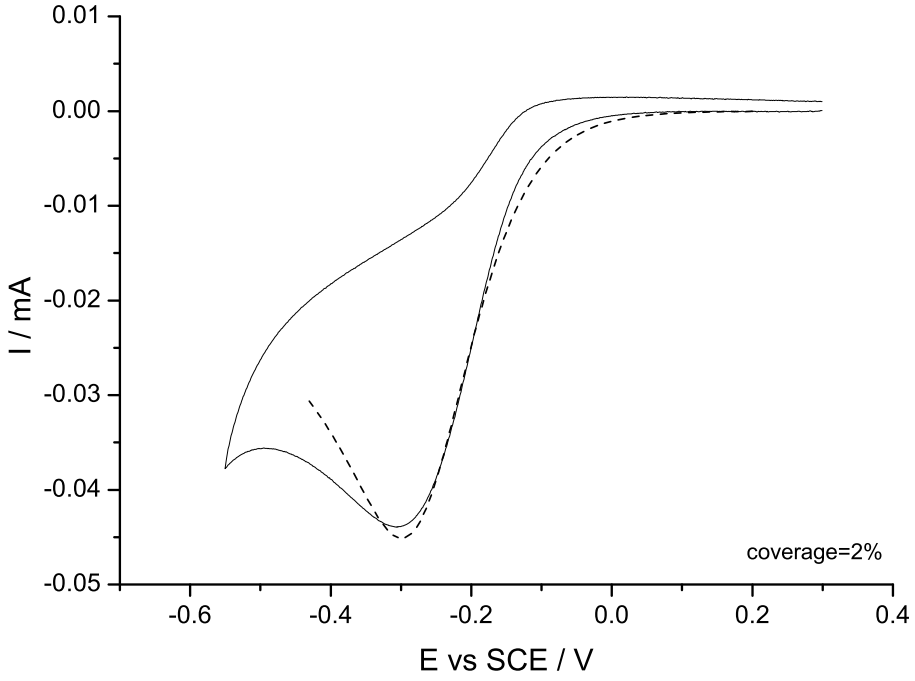


Figure 6.13: Comparison of ORR experimental (solid line) on a gold nanoparticle modified glassy carbon electrode and simulated (dashed line) voltammograms calculated assuming the kinetics on bulk gold at 100 mVs^{-1}.

Table 6.7: Summary of the ORR kinetics in 0.5 M sulfuric acid at 298 K on gold macroelectrode and gold nanoparticle-modified glassy carbon electrode in the absence (Au-NPs/GCE) and presence (Au-NPs/GCE + Pb^{2+}) of Pb^{2+} in the solution (see text).

	Au-NPs/GCE + Pb^{2+}	Gold macroelectrode and Au-NPs/GCE
step 1	$k_{0,1}$= 0.55 cm·s^{-1} (this work) $E_1^0 = -0.298$ V(*vs* SCE) ([1]) $\alpha_1 = 0.52$ (this work)	$k_{0,1}$=0.30 cm·s^{-1} ([1]) $E_1^0 = -0.298$ V(*vs* SCE) ([1]) $\alpha_1 = 0.45$ ([1])
step 2	pKa_{HO_2} =4.88 [39]	pKa_{HO_2} =4.88 [39]
step 3	E_2^0=1.19 V(*vs* SCE) [61]	E_2^0=1.19 V(*vs* SCE) [61]
step 4	p$Ka_{H_2O_2}$ =11.62 [57]	p$Ka_{H_2O_2}$ =11.62 [57]

6.2.3.2 Oxygen Reduction Reaction on "Cleaned" Au-NPs/GCE

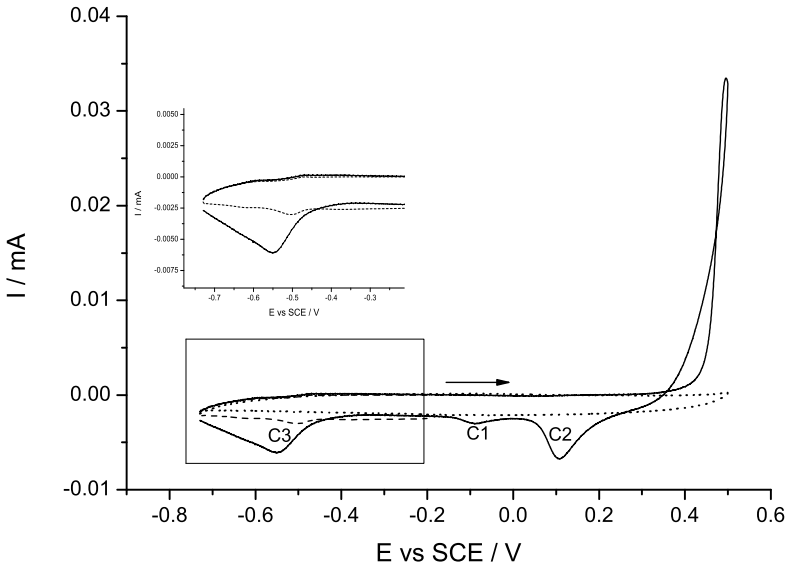


Figure 6.14: Cyclic voltammograms corresponding to the cleaning process of Au-NPs/GCE (solid line), bare GCE (dotted line) and underpotential deposition of lead on the same Au-NPs/GCE (dashed line) in 0.1 mM $Pb(NO_3)_2$ and 0.1 M NaOH, 50 mVs^{-1}. Inset corresponds to the potential region where underpotential deposition of lead on gold takes place in this medium.

Figure 6.14 shows typical cyclic voltammograms corresponding to the "cleaning" treatment on a Au-NPs/GCE (solid line) and a bare GCE (dotted line) and to the underpotential deposition of lead on the same Au-NPs/GCE (dashed line) in 1 mM $Pb(NO_3)_2$ and 0.1 M NaOH at a sweep rate of 50 mVs^{-1}. The inset in Figure 6.14 corresponds to the potential region where underpotential deposition of lead on gold takes place. At the high pH medium of this treatment, Pb_3O_4 and PbO_2 are expected to be deposited on gold at the anodic signal of the forward scan [82–84], which are *partially* stripped off in the reverse one. Note that, in this work, more positive potentials are avoided to prevent the deposition of PbO_2 on the glassy carbon surface. According to the stability of lead species at the working pH [82–84], peaks C1 and C2 correspond to the electroreduction of PbO_2 and Pb_3O_4, respectively. Regarding peak C3, in part this is due to lead underpotential deposition on gold as can be inferred from the inset in Figure 6.14. This is an interesting result considering the very small size of the particles and it will be further discussed in section 6.2.3.3. It can be observed that other faradaic processes take place at the potential region of C3 since the signal is much larger than the UPD one. Further investigation of C3 at a gold macroelectrode (Figure 6.15) points out that the magnitude of C3 decreases when reducing the upper potential limit and it is the same as the UPD signal when the lead oxide deposition does not take place (blue line in Figure 6.15). Thus, we can infer that C3 is related to both lead UPD on gold nanoparticles and the electroreduction of lead oxide species [65, 84]. Considering the cyclic voltammogram obtained for bare GCE (dotted line in Figure 6.14), lead

oxides are not expected to deposit on the glassy carbon surface in this potential range. The ratio of the reductive charge in the reverse scan to the anodic charge in the forward scan is around 0.9, which can be due to the partial dissolution of PbO_2 in basic solution [85] and also to the formation of soluble lead species in the forward scan that diffuse towards the bulk solution.

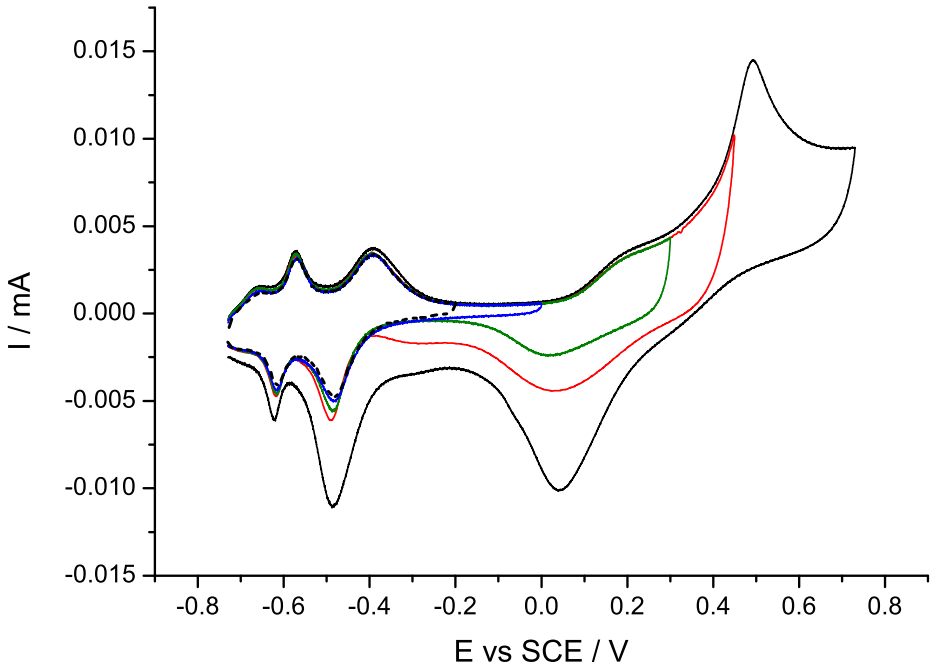


Figure 6.15: Deposition and stripping of PbO_2 and underpotential deposition (dashed line) on a gold macroelectrode at different upper limit oxidation potentials in 0.1 M NaOH in the presence of 1 mM $Pb(NO_3)_2$, 50 mVs^{-1}, 298 K.

Electroreduction of oxygen in 0.5 M sulfuric acid has been carried out on citrate capped Au-NPs/GCE after this "cleaning" procedure. Figure 6.16 shows the comparison of cyclic voltammetry of ORR on "uncleaned" (dotted line) and "cleaned"(solid line) Au-NPs/GCE in oxygen saturated 0.5 M sulfuric acid solution at 100 mVs^{-1}

and 298 K. As can be seen, there is a very significant enhancement of the ORR kinetics after the PbO_2 treatment of the modified electrodes that leads to a considerable decrease of the ORR overpotential of 90 mV. The experimental value of transfer coefficient $\alpha_{1,cleaned} = 0.57$ calculated from the slope of peak current (I_P) against square root of scan rate($\sqrt{\nu}$) (Figure 6.17) and Tafel plot (Figure 6.18) is quite noticeably larger than on bulk gold ($\alpha_{1,bulk} = 0.45$), which also indicates the "activation" of the reduction process after the cycling in alkaline lead solution. Note that the α value is given by $\frac{dE}{dlnI} = \frac{RT}{\alpha F}$, in accordance with IUPAC convention [86, 87]. The definition was selected to be experimentally based and does not imply any value of the number of electrons transferred.

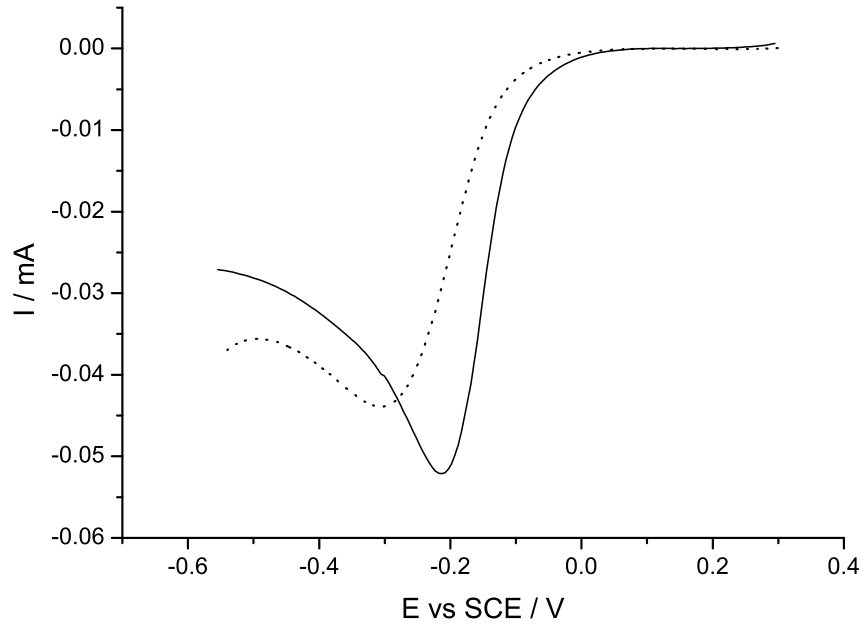


Figure 6.16: Comparison of cyclic voltammetry of ORR on "uncleaned" Au-NPs/GCE (dotted line) and cleaned Au-NPs/GCE (solid line) in oxygen saturated 0.5 M sulfuric acid solution, 100 mVs^{-1}, 298 K.

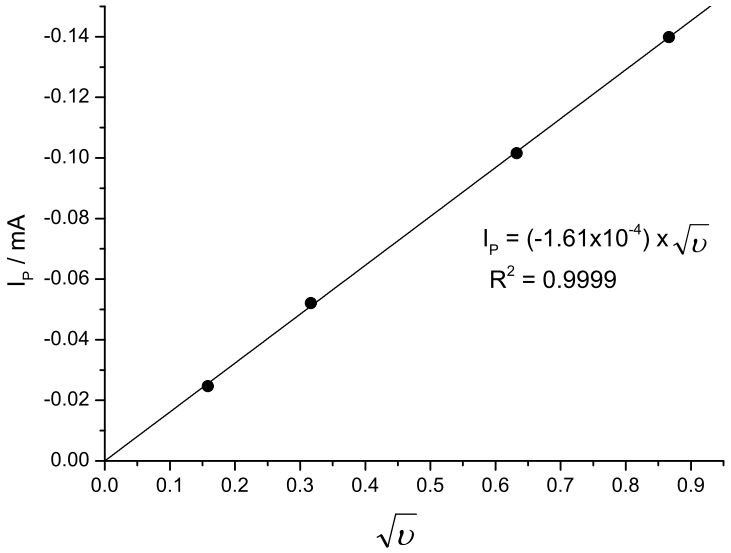


Figure 6.17: Correlation of the experimental peak current *versus* the square root of the scan rate.

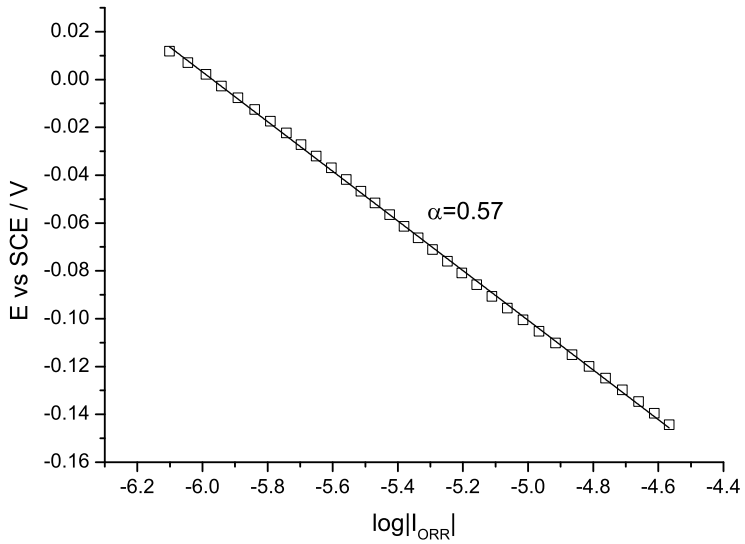


Figure 6.18: Tafel analysis of the voltammetry obtained with "cleaned" Au-NPs/GCE in oxygen saturated 0.5 M sulfuric acid solution at 298 K.

Considering the phenomena taking place during the cleaning process, several factors might be considered in order to explain the catalysis found on the "cleaned" nanoparticles. Thus, this might be related to the removal of the citrate layer but also to the presence of lead species on the nanoparticle surface after the deposition-stripping cycling. Indeed, Chen *et. al* [64] found traces of lead after applying a similar cleaning treatment to gold nanoparticles.

ORR Catalysis by Lead Underpotential Deposition

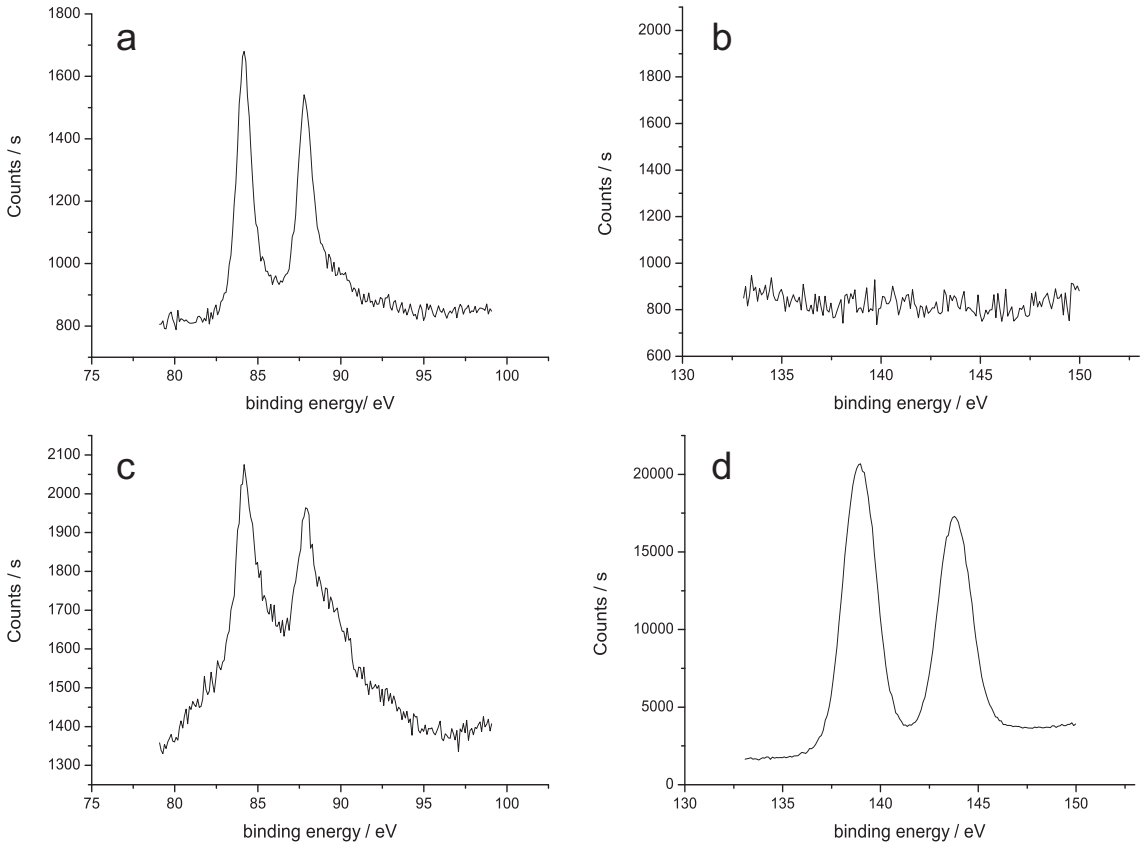


Figure 6.19: XPS spectra for Au 4f (a,c) and Pb 4f (b,d) of gold nanoparticle-modified glassy carbon electrode before (a,b) and after(c,d) the cleaning process.

The elemental composition of the nanoparticle-modified surface before and after cleaning was examined by X-ray photoelectron spectroscopy (XPS) and Figure 6.19 shows the signals corresponding to Au 4f (a,c) and Pb 4f (b,d) before (a,b) and after (c,d) cleaning. The binding energies of the doublet for Au $4f_{7/2}$ at 84.0 eV and Au $4f_{5/2}$ at 87.8 eV are characteristic for metallic gold [88, 89]. The binding energy for the Pb 4f doublet indicates the presence of lead oxide species after the cleaning procedure [90, 91].

XPS confirmed the presence of lead species on the electrode surface after the PbO_2 deposition/stripping step. The possible influence of Pb species on the ORR kinetics will now be considered. Figure 6.20 shows the cyclic voltammetry of bare GCE (dashed line) and Au-NPs/GCE after the cleaning process in nitrogen-saturated (solid line) and oxygen-saturated (dotted line) 0.5 M sulfuric acid solution. As can be observed in the inset, there appear two small peaks (C4 and C5) for Au-NPs/GCE in N_2-saturated solution in the ORR potential region. These can be assigned to the underpotential deposition of lead on the gold nanoparticle surface [92], with the Pb^{2+} made available through the dissolution of lead oxides in this acidic solution. Electrocatalysis of ORR by the presence of foreign metal ad-atoms on the surface of gold macroelectrodes, including Pb, has been reported in the literature [73, 92]. According to Adzic *et.al* [73], a gold surface covered by lead ad-atoms would be more suitable in terms of the adsorption of oxygen and ORR intermediates than a bare gold surface, resulting in enhanced ORR kinetics. Though underpotential deposition of ad-atoms may not be apparent at very small particles [93–96], the

results shown in Figure 6.14 and Figure 6.20 point out that lead UPD does happen on 5 nm gold nanoparticles and it can be responsible for the ORR catalysis.

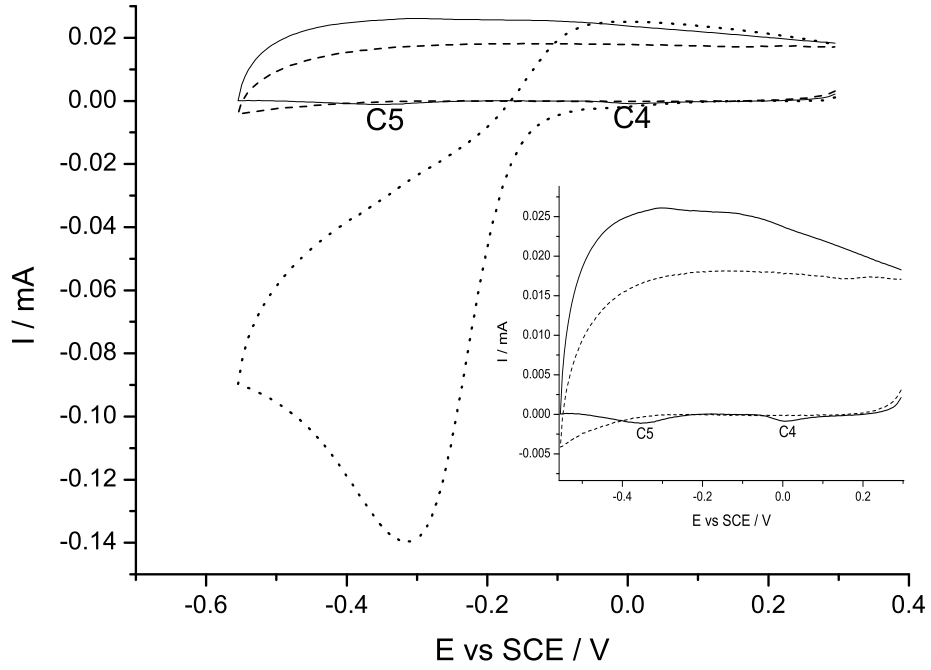


Figure 6.20: Cyclic voltammetry on bare GCE (dashed line), Au-NPs/GCE after the "cleaning" process (solid line) in nitrogen-saturated 0.5 M sulphuric acid solution and Au-NPs/GCE after the "cleaning" process (dotted line) in oxygen-saturated 0.5 M sulphuric acid solution, 750mVs^{-1}, 298 K.

The above question is further studied in Figure 6.21 that shows the comparison of the ORR cyclic voltammetry on "cleaned" Au-NPs/GCE (solid line), "uncleaned" Au-NPs/GCE (dotted line) and "uncleaned" Au-NPs/GCE in the presence of Pb^{2+} in O_2-saturated 0.5 M sulphuric acid solution. It can be inferred that, similar to what is observed on macroelectrodes, the presence of Pb^{2+} catalyses the electroreduction of oxygen on gold nanoparticles. Figure 6.22 shows the best fitting of ORR kinetics

on "uncleaned" Au-NPs/GCE in the presence of Pb^{2+} from 100 mVs^{-1} to 750 mVs^{-1} with the best fitting values being included in Table 6.7. A significant increase in the value of the transfer coefficient (α) is observed after the addition of Pb^{2+} to the solution, which can be rationalized in terms of the different absorptivity of the participating species with respect to bare gold and it leads to better performance for ORR.

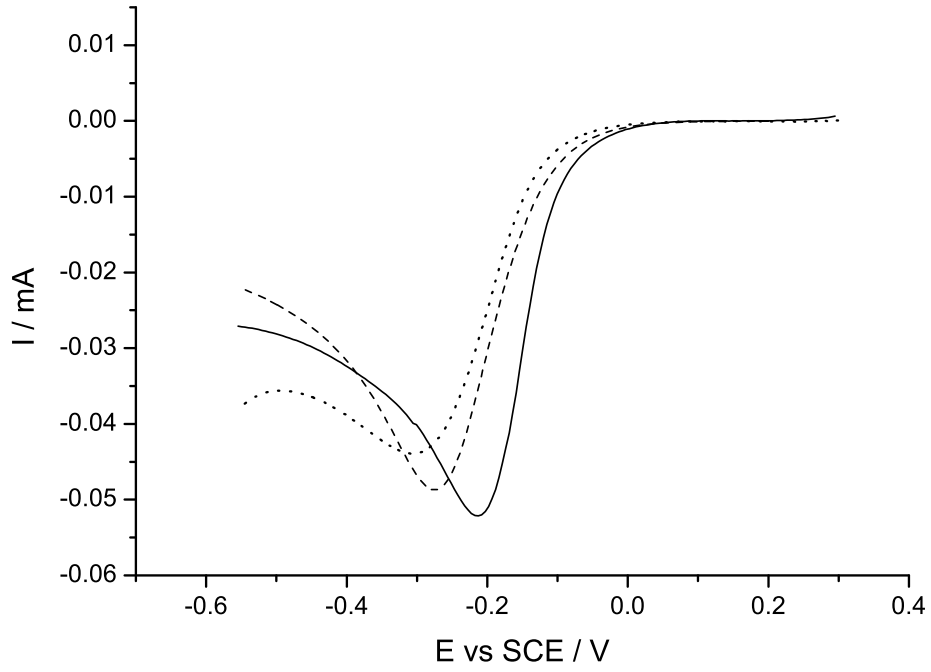


Figure 6.21: Oxygen reduction reaction in 0.5 M sulphuric acid solution on "uncleaned"(dotted line) and "cleaned" (solid line) Au-NPs/GCE at 100 mVs^{-1}, 298 K. Cyclic voltammetry for "uncleaned" Au-NPs/GCE(dashed line) in oxygen saturated 0.5 M sulfuric acid solution with the addition of Pb^{2+}, 100 mVs^{-1}, 298 K.

Figure 6.21 shows that the electrocatalysis observed on the "cleaned" nanoparticles is greater than on "uncleaned" NPs in the presence of Pb^{2+}. Several reasons

for this divergence can be envisaged. The cleaning effect of the PbO_2 treatment together with a greater availability of Pb^{2+} may lead to a more complete lead layer formed on the nanoparticle surface and, consequently, a stronger catalytic activity observed. Moreover, SEM images and EDX analyses after the PbO_2 treatment (Figure 6.12.d) show that a "shell" of lead oxides can remain on some gold nanoparticles after the cleaning. The (electro)chemical behaviour of this shell during oxygen electroreduction in sulfuric acid medium needs for further investigation.

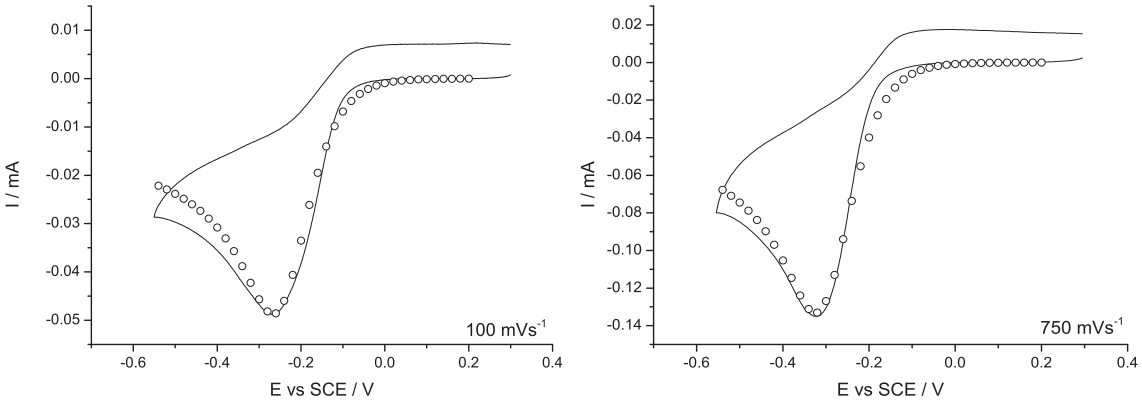


Figure 6.22: Comparison of experimental voltammograms on "uncleaned" Au-NPs/GCE in the presence of Pb^{2+} (solid line) and simulation (circle points) corresponding to the parameters obtained from the best fitting of the voltammetry in the range 100-750 mVs^{-1}.

6.2.3.3 Lead UPD on 5 nm Gold Nanoparticles

It is worth highlighting that the results presented in the previous sections point out that lead underpotential deposition (UPD) is operative on the citrate-capped 5-nm gold nanoparticles synthesized in this work. This behaviour is in itself of great interest since previous experimental results [94–96] and theoretical predictions [93] support the disappearance of UPD on very small particles. Thermodynamically

speaking, the adsorption of ad-atoms at edge sites is less favourable than at facets and therefore UPD is predicted to vanish as the nanoparticle size decreases and so the relative number of facet sites [93]. Some experimental evidence has been reported in this sense, including the deposition of thallium, lead and cadmium on silver nanoparticles, where the UPD peaks were found to disappear when the particle diameter is smaller than 50 nm [94–96].

In contrast with the above results, lead underpotential deposition on gold nanoparticles 5-nm in diameter has been observed in the present work both in strong alkaline (Figures 6.14 and 6.15) and strong acid (Figure 6.20) media. From the lead UPD charge obtained experimentally at Au NPs-modified electrode and the total number of particles determined from stripping in HCl solution, the charge density for lead UPD on gold nanoparticles can be calculated. With the caveats related to the uncertainties in the integration of the small UPD peaks recorded, a value of 390 $\pm$ 70 μC cm^{-2} is obtained, which lies in the range reported for gold single crystals (330 - 380 μC cm^{-2}) and polyorientated gold electrodes (420 μC cm^{-2}) [65].

6.2.4 Conclusions

The electrocatalytic activity of 5 nm citrate-capped gold nanoparticles (Au NPs) towards oxygen reduction reaction (ORR) in 0.5 M sulphuric acid solution has been investigated from the quantitative analysis of the cyclic voltammetry at nanoparticle-modified electrodes. Gold nanoparticles have been synthesized *via* the chemical reduction of gold(III) by sodium borohydride in the presence of citrate. Then, the

nanoparticles were deposited on glassy carbon electrodes by electrophoresis.

The ORR cyclic voltammetry on the Au NPs-modified electrodes in a wide range of scan rates was described satisfactorily with the two-electron, two-proton E_{rds}CEC mechanism proposed for gold macroelectrodes, with hydrogen peroxide as the final product. Quantitative analysis of the voltammograms indicates that the ORR kinetics on the citrate-capped Au NPs-modified electrodes is effectively the same as on bulk gold. On the other hand, a strong electrocatalytic activity towards ORR is observed in the presence of Pb^{2+} ions or when the nanoparticle-modified electrode is cycled in lead(II) alkaline solution prior to the ORR experiments.

Underpotential deposition (UPD) of lead on the nanoparticle surface is found to take place on such small particles and to be related with the ORR electrocatalysis. This evidence of lead UPD on 5 nm gold nanoparticles contrasts with the absence of adsorption of some other metals on silver nanoparticles smaller than 50 nm.

6.3 Strong Negative Nanocatalysis: Oxygen Reduction and Hydrogen Evolution at Very Small (2 nm) Gold Nanoparticles

6.3.1 Introduction

The oxygen reduction reaction (ORR) and hydrogen evolution reaction (HER) are two key processes in the energy future of mankind [13, 97–104]. Renewable and

clean energy technologies depend heavily on hydrogen evolution and/or oxygen reduction. In both cases understanding the catalysis associated with the hydrogen evolution reaction (HER) or oxygen reduction reaction (ORR) lies at the heart of designing better materials for these key electrode reactions. Accordingly, one of the current main challenges is the design of catalytic materials towards HER [97–101] for hydrogen production from electrochemical water-splitting (so reducing undesirable emissions) and towards ORR [13, 102–104] for the development of high performance hydrogen-oxygen fuel cells.

In the earlier two sections of this chapter, the electron transfer kinetics of the oxygen reduction reaction in 0.5 M sulfuric acid at electrodeposited "naked" gold nanoparticles sized from 17 nm to 40 nm and 5 nm citrate capped gold nanoparticles were investigated. In this section, following similar methodology to that presented before, here we consider the electrocatalytic activity of 2 nm citrate capped gold nanoparticles (Au-NPs) towards both the ORR and the HER. As indicated before, this has a great practical significance for the rational development of efficient electrocatalysts and it is also of fundamental interest given that such small particles lie at the frontier between isolated molecules and bulk materials and so between classical physics and quantum mechanics. The main steps followed for the characterization of the Au NP catalytic activity are summarized in Figure 6.23.

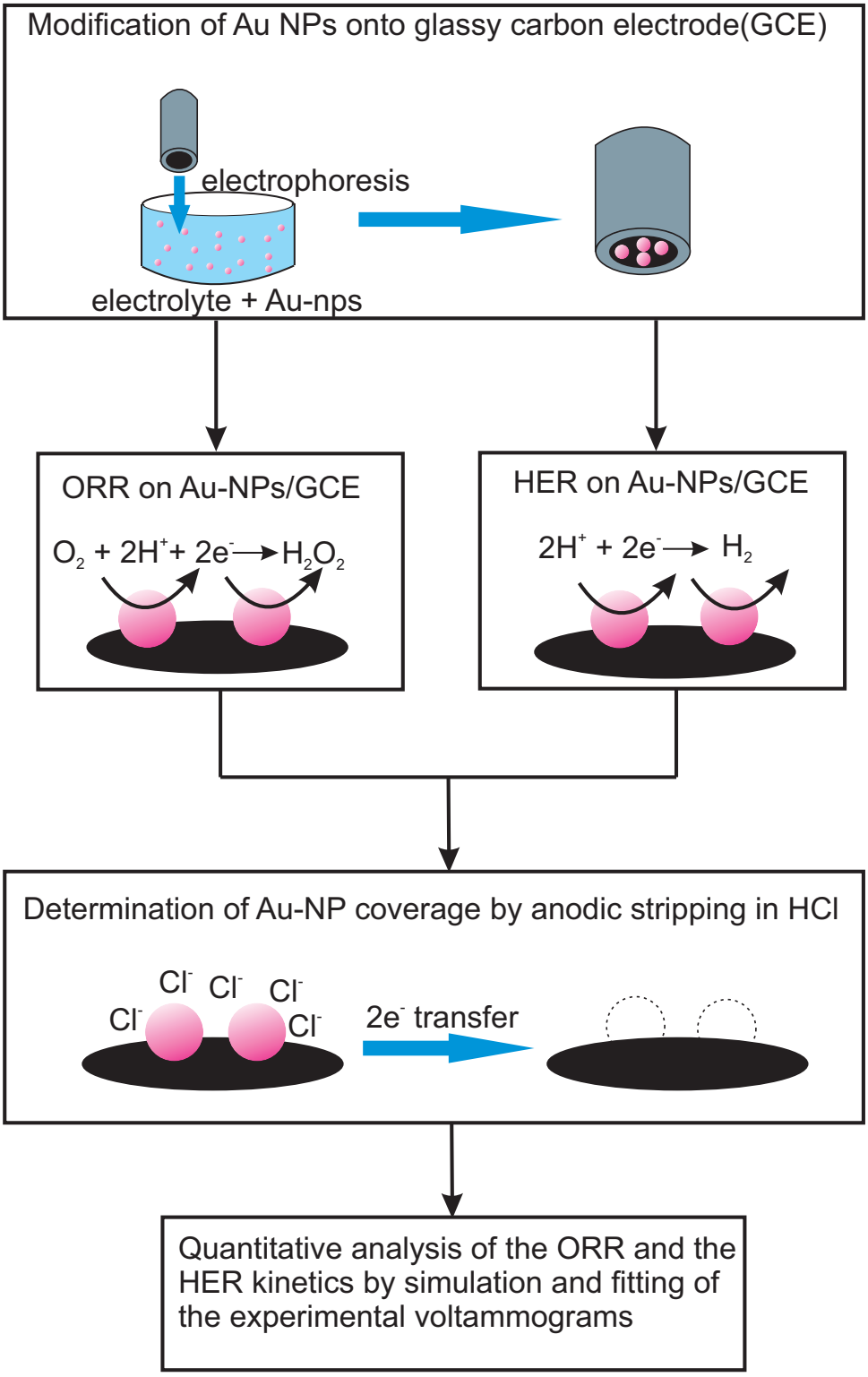


Figure 6.23: Strategy applied in this work for the quantitative kinetic studies of the ORR and HER kinetics on 2 nm Au-NPs/GCE.

6.3.2 Experimental Section

6.3.2.1 Chemical Reagents

Sulphuric acid (H_2SO_4, Fisher, >95%), hydrochloric acid (Sigma-Aldrich, >37%) and citrate-capped 1.9 nm gold nanoparticles (Nanopartz; Zeta potential = −30 mV) were all used without further purification. All the solutions were prepared using deionised water with resistivity of 18.2 MΩ cm (25 °C).

6.3.2.2 Instrumental

The instrumental information for electrochemistry measurements were the same as presented in the section 6.1.2.2.

Transmission electron microscopy (TEM) images were obtained on FEI TECNAI T20 (200 kV/LaB6-filament/EDX-Oxford-detector). Both facetting of individual and possible agglomeration of multiple nanoparticles can be identified with diffraction contrast. This was carried out by Dr. Kristina Tschulik and Dr. Christine Damm.

6.3.3 Results and Discussion

First, we discuss the details of the glassy carbon electrode (GCE) modification and the determination of the NP coverage, which are common to the studies of both the ORR and the HER reactions. TEM analysis (displayed in Figure.6.24.a) shows that the commecially purchased citrate capped gold nanoparticles are spherical in shape

and the diameter is 1.9 ± 0.8 nm. A GCE is chosen as substrate on which to examine nanoparticle catalytic behaviour given that GCE shows poor electrocatalytic ability towards ORR and HER such that it offers a clean potential window where the ORR and HER responses on Au NPs can be studied without significant interference of the substrate. To modify the GCE, it is immersed in a Au NP solution (0.38 μM gold nanoparticles in 0.1 M $NaClO_4$) where nanoparticles adsorb on the surface and modify the electrode. This approach favours the even distribution of the particles in contrast with drop-casting methods where particles were observed to concentrate in a small region of the GCE surface during the drying process, which can also promote particle aggregation [105]. This is important to assure accurate results given that the theoretical modeling employed here assumes that the NPs resemble an array of uniform and evenly-distributed nanoelectrodes [31, 60].

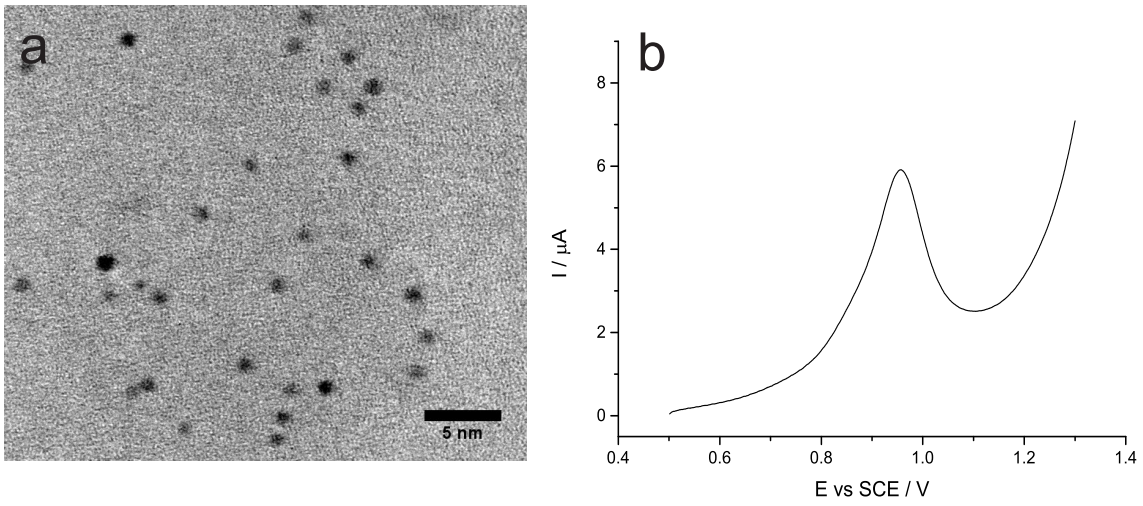


Figure 6.24: **(a)** TEM image of the citrate-capped gold nanoparticles investigated. **(b)** Anodic stripping of citrate capped gold nanoparticles from a modified glassy carbon electrode in 0.1 M HCl at 50 mVs^{-1}. $T = 298$ K.

The sticking of citrate-capped Au NPs onto GCE under open circuit conditions

have been found to be very slow leading to very low coverage (less than 1%, beyond the detection limit of anodic stripping coulometry in HCl, see below) even after long modification times [2]. Following the methodology employed successfully in a previous paper [2], the application of a positive potential for the electrode modification was examined in order to enhance the flux of the negatively-charged citrate-capped NPs towards the GCE and achieve higher coverage. An electrophoretic potential of +0.1 V (vs. SCE) was applied in order to prevent the nanoparticle electro-oxidation. All the experiments are carried out with fresh commercial nanoparticle solutions subject to 5 min sonication before each GCE modification in order to prevent NP aggregation and settling, which result in lower nanoparticle sticking.

Knowledge of nanoparticle coverage is the key factor allowing rigorous quantitative studies. First, the highest NP coverages which can be studied are set by the theoretical model where the nanoparticles are supposed to be of uniform size and evenly distributed on the GCE surface. For instance, a 15 % coverage means that *even if* the distribution of the particles was perfectly homogeneous the average interparticle distance would be less than 6 nm. The formation of aggregates and porous structures cannot be discarded under such conditions which is not accounted for in our simulations. Also, when modifying surfaces with nanosized materials the ultimate goal is to use as little of the (typically expensive noble-metal based) material as possible and to avoid agglomeration of the nanoparticles, so as to avoid losing positive nano-effects towards more bulk-like behavior. Thus, a homogeneous distribution of reasonably-spaced individual particles is envisaged for both practical

engineering aspects and theoretical analysis purposes. Secondly, Figure 6.25 shows the ORR voltammograms on bare GCE (solid line) and Au-NPs/GCE with 3 % (dashed line) and 7 % (dotted line) NP coverage in an oxygen-saturated 0.5 M sulfuric acid at 298 K and 750 mVs^{-1}. From the figure it can be inferred that there is a very significant contribution from the substrate to the ORR signal (that is, from ORR on bare GC regions) for 3 % coverage such that the electrochemical response is less informative about the ORR kinetics on Au NPs.

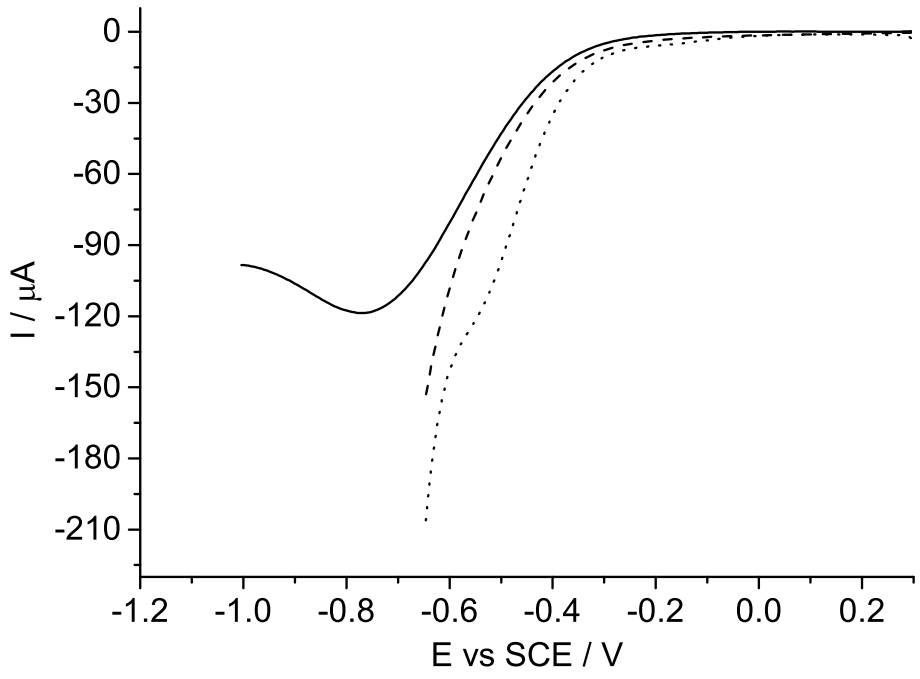


Figure 6.25: Experimental voltammograms for oxygen reduction reaction on a bare glassy carbon electrode (solid line), Au-NPs/GCE with 3 % (dashed line) and 7 % (dotted line) coverages at 298 K, 750 mVs^{-1}.

Considering all the above factors, a modification time of 60 min was found to be adequate given that it yields an appropriate coverage value of *ca.* 6 % - 8% such

that the recorded signal reflects quantitatively the kinetics on Au NPs while keeping the experimental time acceptably short.

The number of nanoparticles deposited on the glassy carbon electrode was estimated from the anodic stripping charge of the particles in 0.1 M hydrochloric acid by consecutive linear sweep voltammetries at 50 mVs^{-1}, which has been successfully employed in previous studies [1, 2, 31, 32]. Finot [106] and Kolics [107] reported that the electro-oxidation products of bulk gold in hydrochloric acid are the $AuCl_4^-$ and $AuCl_2^-$ complexes. More recently [34], this conclusion was extended to the case of gold nanoparticles such that the NP stripping involves 1.9 ± 0.1 electrons transferred *per* gold atom. Given that TEM images prove the nanoparticles to be of spherical shape, the number of nanoparticles (N) can be immediately related to the stripping charge (Q) provided that the average radius of the particles (r) is known:

$$N = Q \times \frac{M_{Au}}{1.9\, e\, \frac{4}{3}\pi r^3\, \rho_{Au}\, N_A} \tag{6.7}$$

where e is the elementary charge, ρ_{Au} the density of gold, M_{Au} its molar mass and N_A the Avogadro constant. Once number of nanoparticles is obtained, the NP coverage is defined as:

$$\Theta = 100 \times \frac{\pi r^2 N}{A} \tag{6.8}$$

Figure 6.24.b shows the anodic stripping voltammogram at a Au-NP/GCE in 0.1 M HCl at 298 K and 50 mVs^{-1}. A typical stripping peak of citrate-capped gold

nanoparticles appears at +0.96 V (*vs.* SCE) [34].

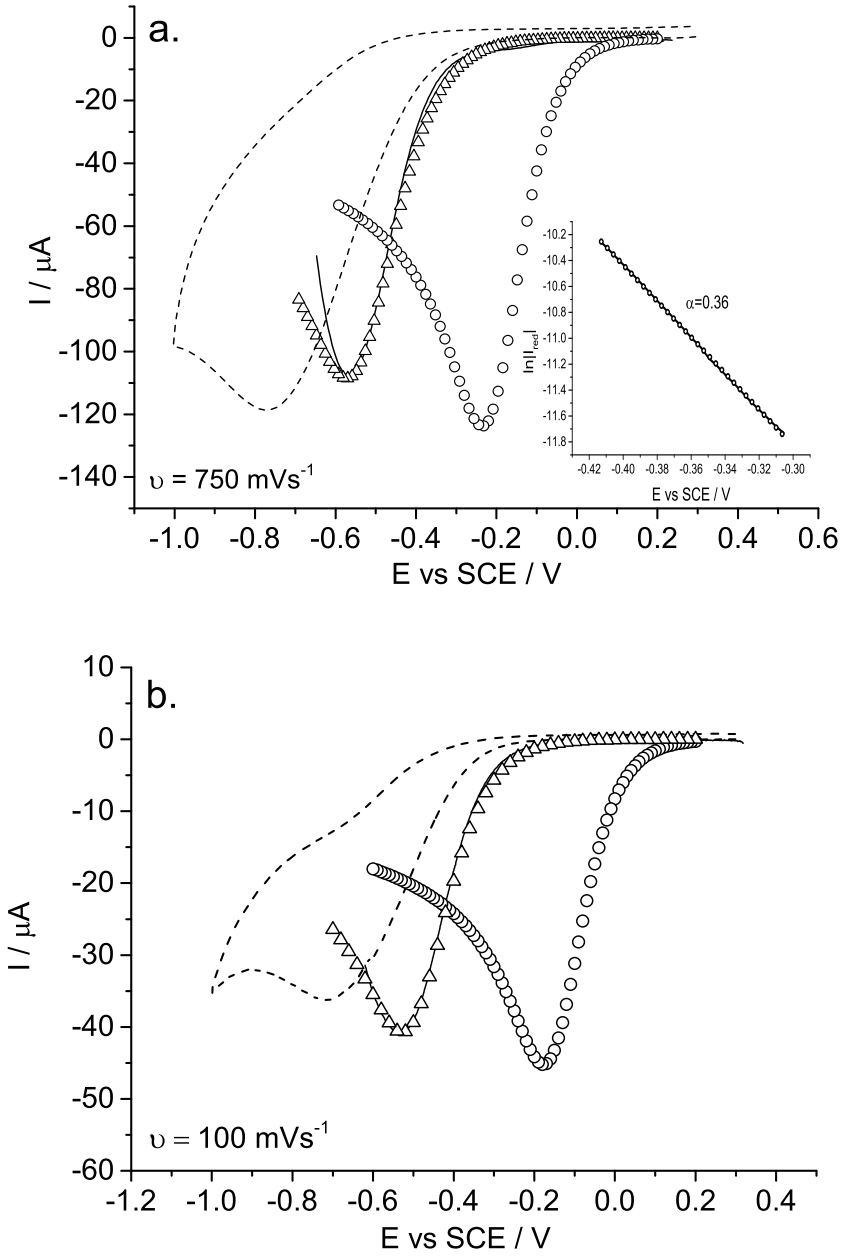


Figure 6.26: Comparison of experimental background-subtracted voltamogramms on bare glassy carbon electrode (dashed line), 1.9 nm Au-NP/GCE (solid line) and simulated voltammograms with the kinetics experimentally obtained for gold macro electrode (open circle) and for gold nanoparticles (open triangle) in oxygen saturated 0.5 M sulfuric acid at 750 and 100 mVs^{-1}. $T = 298$ K.

Next, we report the Au NP electrocatalytic activity towards ORR. All the elec-

trochemistry measurements of ORR on Au-NPs/GCE were carried out in oxygen saturated 0.5 M sulphuric acid at 298 K. Figure 6.26 shows the background-subtracted experimental voltammograms for ORR in an oxygen-saturated 0.5 M sulphuric acid solution ($T = 298$ K, a: $v = 750$ mVs^{-1}, b: $v = 100$ mVs^{-1}) on bare GCE (dashed line) and on Au-NP/GCE (solid line). The NP coverages of Au-NP/GCE are *ca.* 7 % based on the anodic stripping charge in HCl measured just after the ORR experiments. The cyclic voltammetry study was performed in the scan rate range 100 - 750 mVs^{-1}. The experimental voltammograms show that the electrocatalytic performance of the nanoparticle-modified electrode is higher than bare GCE. To determine how this performance compares with that of bulk gold in order to detect possible changes in the ORR kinetics as a result of nanoeffects, we make use of a simulation program developed in our group by Dr. Kristopher R. Ward, which enables the rigorous simulation of cyclic voltammetry experiments on nanoparticle-modified electrodes, taking into account the remarkable differences between the mass transport at a macroelectrode and at an array of particles acting as nanoelectrodes. This program models the modified-electrode surface as an array of uniform sized and evenly distributed spherical nanoelectrodes resting on a substrate [31, 60]. For the electron transfer kinetics at the NP surface, the Butler-Volmer formalism is employed [35] and the concentrations of the different species in solution are subject to mass transport by diffusion and the chemical transformations established by the reaction scheme (see Eq. 6.3-6.6). The resulting diffusive-kinetic differential equation system is solved by finite-difference methods for cyclic voltammetry conditions. The

fitting of the experimental voltammograms enables the quantitative characterization of the electrochemical kinetics at the nanoparticles taking into account the interplay between the NP diffusion domains.

Table 6.8: Electron transfer kinetics of the oxygen reduction and hydrogen evolution reactions at gold macroelectrodes and at 1.9 nm citrate-capped Au-NPs at 298 K in 0.5 M sulfuric acid solution. The values reported correspond to the best fit of the cyclic voltammograms obtained at different scan rates between 100 and 750 $\mathrm{mV\,s^{-1}}$.

	ORR		HER	
	Bulk Au	Au-NPs	Bulk Au	Au-NPs
α	0.45[1, 2]	0.37 ± 0.01	0.46± 0.01	0.53 ± 0.01
k_0 $(\mathrm{cm\,s^{-1}})$	0.3[1, 2]	$(1.6 \pm 0.3) \times 10^{-3}$	$(6.4\pm 0.6) \times 10^{-7}$	$(9.0 \pm 0.1) \times 10^{-8}$

By implementing the reaction mechanism given in Eq. 6.3 - 6.6 with the home-written simulation program, the cyclic voltammetry response expected if the ORR kinetics on the Au NPs was the same as on bulk gold was simulated (open circle in Figure 6.26). The coverage of Au NPs were ca. 7 %, these were determined from anodic stripping in HCl after each experiment. Thus, the ORR kinetic parameters obtained on bulk gold in previous studies [1] were employed (see Table 6.8), along with the NP coverage and the average NP size extracted from the TEM images (1.9 nm). By comparing the experimental (solid line) and simulated (open circle) results one can observe a clear increase of the overpotential (*ca.* −330 mV) and decrease of the peak current (10 %) when moving from bulk gold to Au NPs. This reveals the fact that the ORR kinetics slows down on 1.9 nm gold nanoparticles compared to bulk gold; a significant *negative* effect is observed.

The negative nanoeffect shown in Figure 6.26 is further proved by quantitative studies using Tafel analysis and fitting of the experimental voltammograms with the home-written simulation program. Thus, satisfactory fittings (open triangle) of the experimental curves from 100 mVs^{-1} (Figure 6.26.b) to 750 mVs^{-1} (Figure 6.26.a) are obtained with a transfer coefficient (α_1) of 0.37 $\pm$ 0.01 and a standard electrochemical rate constant of (1.6 $\pm$ 0.3) $\times$ 10^{-3} $cm\,s^{-1}$. Note that the former is in very good agreement with the transfer coefficient value evaluated from the Tafel plot (0.36) (inset in Figure 6.26.a).

As summarized in Table 6.8, the ORR kinetics on 1.9 nm Au NPs is significantly slower than on gold macroelectrodes. This also means that the 1.9 nm Au NPs are poorer catalysts for the ORR in this media than the larger particles (5-40 nm) previously investigated, where the ORR kinetics was found to be very similar to that at macroelectrodes [1, 2].

Next, the HER kinetics at gold nanoparticles are examined to see if negative catalysis also exists for that reaction. The kinetic behaviour at a gold macroelectrode is quantified using cyclic voltammograms obtained in nitrogen-saturated 0.5 M H_2SO_4 between 100 and 750 mVs^{-1} (solid line in Figures 6.27.a and 6.27.b). The electron transfer kinetics are quantified by Tafel analysis and fitting of experimental cyclic voltammograms from 100 mVs^{-1} to 750 mVs^{-1} with the commercial simulation software DigiSim. In order to apply DigiSim to quantify the electron transfer kinetics, the mechanism of HER need first to be considered. It is widely accepted as the following steps [97, 109]:

$$\mathrm{H}^+ + e^- \overset{k_{0,3},E^0_3,\alpha_3}{\longrightarrow} \mathrm{H_{ad}} \quad (slow) \tag{6.9}$$

$$\mathrm{H}_{ad} + \mathrm{H}^+ + e^- \longrightarrow \mathrm{H_2}\,(g) \quad (fast) \tag{6.10}$$

where, $k_{0,i}$ is the electron transfer rate constant, α_i the transfer coefficient and E^0_i the formal potential of step i.

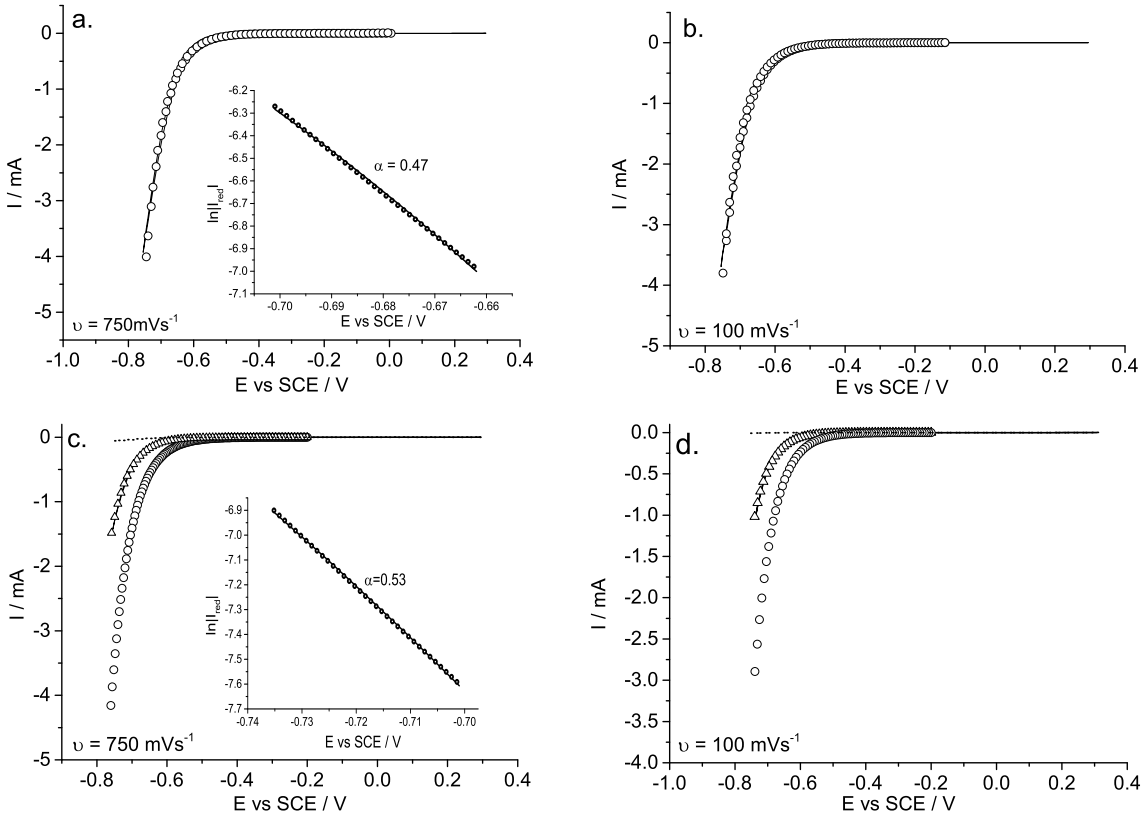


Figure 6.27: Experimental current-potential curves corresponding to the hydrogen evolution in nitrogen saturated 0.5 M sulfuric acid solution at 750 and 100 $\mathrm{mVs^{-1}}$ on a: **(a, b)** macro gold electrode (solid line); **(c, d)** citrate-capped 1.9 nm Au-NP/GCE (solid line) and bare GCE (dashed line). Simulated current-potential curves with the kinetics obtained experimentally for gold macro-electrodes (open circle) and for gold nanoparticles (open triangle). Diffusion coefficient of $\mathrm{H^+}$: 8.8×10^{-5} $\mathrm{cm^2 \cdot\ s^{-1}}$ [108]. Insets: Tafel analyses. $T = 298$ K.

The first step where protons are electro-reduced to adsorbed atomic hydrogen is thought to be rate determining [97]. Subsequently, adsorbed atomic hydrogen combines with a proton and is further reduced to molecular hydrogen.

As shown in Figures 6.27.a and 6.27.b, a satisfactory fitting of the experimental (solid line) and simulated (open circle) voltamograms are obtained in the whole range of scan rates with a standard electron transfer rate constant ($k_{0,3}$) of 6.4 $\times$ 10^{-7} cm s^{-1} and a transfer coefficient value of 0.46$\pm$ 0.01. The latter compares well with the α_3 value (0.47) obtained from the Tafel plot (inset in Figure 6.27.a) and the literature [97, 110].

Next, cyclic voltammetry experiments were performed with Au NP-modified electrodes. Figures 6.27.c (750 mVs^{-1}) and 6.27.d (100 mVs^{-1}) show the comparison of the HER experimental signals in nitrogen-saturated 0.5 M sulphuric acid solution at 298 K on Au-NP/GCE (solid line) and bare GCE (dashed line). According to the gold anodic stripping charge in HCl, the NP coverage is 7 % and 7.5 % for 750 mVs^{-1} and 100 mVs^{-1}, respectively. The voltammograms show in that the presence of Au NPs on the GCE surface catalyzes the HER reaction. However, when comparing the experimental signal (solid line) with the home-written simulations run with the kinetic parameters above-obtained for gold macroelectrodes (open circle) of the same coverage, a lower catalytic activity by the Au NPs with respect to bulk gold can be inferred.

In order to quantify these changes, the $k_{0,3}$ value and the transfer coefficient value were obtained from the fitting of the current-potential curves with the home-

written simulation program from 100 mVs^{-1} to 750 mVs^{-1}. The best-fit curves (open triangle) corresponds to the values $k_{0,3}$ =(9.0 ± 0.1) × 10^{-8} $cm\,s^{-1}$ and α_3 =0.53 ± 0.01, respectively. The latter fully agrees with the α_3 value obtained in the Tafel analysis (0.53, see inset in Figure 6.27.c) and $k_{0,3}$ at Au NPs is significantly smaller than the value obtained at gold macroelectrodes (see Table 6.8).

The above results clearly reveal a slowing down of the electrochemical kinetics of both ORR and HER on 1.9 nm citrate capped gold nanoparticles in strong acid media. In the case of ORR no kinetic changes on larger gold nanoparticles supported on a glassy-carbon electrode (5 nm and 40 nm) [1, 2]. This enables us to discard support-only effects. Also, mass transport effects can be disregarded given that the theoretical model describes it rigorously. Therefore, the behaviour reported here is particle size-related and it seems to be apparent only for NP diameters below 5 nm.

The above conclusion is compatible with other claims of a loss of activity of gold and platinum NPs towards oxygen reduction and carbon monoxide oxidation when the particles are smaller than 2-3 nm [111], which was rationalized in terms of the oxygen binding energy at low coordinate sites that are more abundant at small particles. Nevertheless, to pinpoint the origins behind this behaviour is not straightforward considering the interplay of a number of structural (facets, defects) and electronic (which can be significant for such small particles) effects associated with nanoparticulate materials [112]. The observation of the negative electrocatalytic effect for the HER at small nanoparticles is entirely novel.

6.3.4 Conclusions

In summary, for ORR, the standard electron transfer rate constant decreases from 0.3 $\mathrm{cm\,s^{-1}}$ [1] in the macro gold electrode to $(1.6 \pm 0.3) \times 10^{-3}$ $\mathrm{cm\,s^{-1}}$ on the 1.9 nm Au NPs while the transfer coefficient changes from 0.45 [1] in the macroscale to 0.37 ± 0.01 at the nanoparticles under study. The values obtained for 1.9 nm Au NPs are also smaller than those reported for larger glassy carbon-supported gold nanoparticles (5-40 nm), which reflects a clear slowing down of the ORR. A similar behaviour is manifested in HER with the standard electron transfer rate constant reducing from 6.4×10^{-7} $\mathrm{cm\,s^{-1}}$ at bulk gold to $(9.0 \pm 0.1) \times 10^{-8}$ $\mathrm{cm\,s^{-1}}$ on the Au NPs, and the transfer coefficient changing from 0.46 ± 0.01 to 0.53 ± 0.01 from the macro-scale to the nano-scale. Therefore, the results obtained clearly suggest negative electrocatalytic nanoeffects by the 1.9 nm citrate capped gold nanoparticles for both the oxygen reduction and hydrogen evolution reactions in sulphuric acid medium.

In this chapter, electron transfer kinetics of gold nanoparticles with different sizes for oxygen reduction reaction in 0.5 M sulphuric acid were studied applying the joint computation and experimental strategy developed in the previous chapter. No kinetic changes were obtained for gold nanoparticles with diameters from 5 nm to 40 nm compared to that on macro gold electrode for ORR in 0.5 M sulphuric acid solution. However, a strong catalytic effect has been displayed on 5 nm citrate capped Au-NPs for ORR with the presence of Pb(II). For citrate capped

gold nanoparticles of diameter 1.8 nm, there is a strong slowing down effect of the electron transfer kinetics for both the ORR and HER systems.

Bibliography

[1] Y. Wang, E. Laborda, K. R. Ward, K. Tschulik and R. G. Compton, *Nanoscale* .

[2] Y. Wang, E. Laborda, B. J. Plowman, K. Tschulik, K. R. Ward, R. G. Palgrave, C. Damm and R. G. Compton, *Physical Chemistry Chemical Physics* **16** (2014) 3200–3208.

[3] Y. Wang, E. Laborda, K. Tschulik, C. Damm, A. Molina and R. G. Compton, *Nanoscale* .

[4] M. T. M. Koper, *Nanoscale* **3** (2011) 2054 – 2073.

[5] S. Vaddiraju, I. Tomazos, D. J. Burgess, F. C. Jain and F. Papadimitrakopoulos, *Biosensors and Bioelectronics* **25** (2010) 1553 – 1565.

[6] F. W. Campbell and R. G. Compton, *Analytical and Bioanalytical Chemistry* **396** (2010) 241 – 259.

[7] R. J. Toh, H. Poh, Z. Sofer and M. Pumera, *Chemistry Asian Journal* **8** (2013) 1295 – 1300.

[8] D. Uzio and G. Berhault, *Catalysis Reviews* **52** (2010) 106 – 131.

[9] R. J. White, R. Luque, V. L. Budarin, J. H. Clark and D. J. Macquarrie, *Chemical Society Reviews* **38** (2009) 481 – 494.

[10] R. A. Van Santen, *Accounts of Chemical Research* **42** (2009) 57–66.

[11] S. Park, Y. Xie and M. J. Weaver, *Langmuir* **18** (2002) 5792 – 5798.

[12] M. Hepel, *Journal of the Electrochemical Society* **145** (1998) 124 – 134.

[13] M. S. El-Deab and T. Ohsaka, *Electrochemistry Communications* **4** (2002) 288 – 292.

[14] S. Yan, S. Zhang, Y. Lin and G. Liu, *Journal of Physical Chemistry C* **115** (2011) 6986 – 6993.

[15] D.-J. Guo and H.-L. Li, *Journal of Colloid and Interface Science* **286** (2005) 274 – 279.

[16] I. Streeter, G. G. Wildgoose, L. Shao and R. G. Compton, *Sensors and Actuators B: Chemical* **133** (2008) 462–466.

[17] M. C. Henstridge, E. J. Dickinson, M. Aslanoglu, C. Batchelor-McAuley and R. G. Compton, *Sensors and Actuators B: Chemical* **145** (2010) 417–427.

[18] M. J. Sims, N. V. Rees, E. J. Dickinson and R. G. Compton, *Sensors and Actuators B: Chemical* **144** (2010) 153–158.

[19] E. Sheridan, J. Hjelm and R. J. Forster, *Journal of Electroanalytical Chemistry* **608** (2007) 1 – 7.

[20] M. S. El-Deab, *Electrochimica Acta* **54** (2009) 3720 – 3725.

[21] H. Ma, B. Yin, S. Wang, Y. Jiao, W. Pan, S. Huang, S. Chen and F. Meng, *ChemPhysChem* **5** (2004) 68 – 75.

[22] M. S. El-Deab, T. Sotomura and T. Ohsaka, *Journal of the Electrochemical Society* **152** (2005) C730–C737.

[23] T. Hezard, K. Fajerwerg, D. Evrard, V. Collire, P. Behra and P. Gros, *Journal of Electroanalytical Chemistry* **664** (2012) 46 – 52.

[24] N. Sakai, Y. Fujiwara, M. Arai, K. Yu and T. Tatsuma, *Journal of Electroanalytical Chemistry* **628** (2009) 7 – 15.

[25] R. M. Penner, *Journal of Physical Chemistry B* **106** (2002) 3339–3353.

[26] W. Plieth, H. Dietz, A. Anders, G. Sandmann, A. Meixner, M. Weber and H. Kneppe, *Surface Science* **597** (2005) 119 – 126.

[27] T. Oyama, T. Okajima and T. Ohsaka, *Journal of the Electrochemical Society* **154** (2007) D322–D327.

[28] O. S. Ivanova and F. P. Zamborini, *Analytical Chemistry* **82** (2010) 5844–5850.

[29] D. V. Leff, P. C. Ohara, J. R. Heath and W. M. Gelbart, *Journal of Physical Chemistry* **99** (1995) 7036–7041.

[30] J. Overbeek, *Advances in Colloid and Interface Science* **15** (1982) 251 – 277.

[31] Y. Wang, K. R. Ward, E. Laborda, C. Salter, A. Crossley, R. M. J. Jacobs and R. G. Compton, *Small* **9** (2013) 478 – 486.

[32] Y. Wang, E. Laborda, C. Salter, A. Crossley and R. G. Compton, *Analyst* **137** (2012) 4693–4697.

[33] J. Hernndez, J. Solla-Gulln and E. Herrero, *Journal of Electroanalytical Chemistry* **574** (2004) 185 – 196.

[34] Y.-G. Zhou, N. V. Rees, J. Pillay, R. Tshikhudo, S. Vilakazi and R. G. Compton, *Chemical Communications* **48** (2012) 224–226.

[35] R. G. Compton and C. E. Banks, *Understanding voltammetry, 2^{nd} edition* (Imperial College Press, 2011).

[36] G. Sandmann, H. Dietz and W. Plieth, *Journal of Electroanalytical Chemistry* **491** (2000) 78 – 86.

[37] H. Angerstein-Kozlowska, B. Conway, A. Hamelin and L. Stoicoviciu, *Electrochimica Acta* **31** (1986) 1051–1061.

[38] J. Petlicki and T. G. M. van de Ven, *Journal of the Chemical Society, Faraday Transactions* **94** (1998) 2763–2767.

[39] J. Diviek and B. Kastening, *Journal of Electroanalytical Chemistry and Interfacial Electrochemistry* **65** (1975) 603 – 621.

[40] D. Meisel and G. Czapski, *Journal of Physical Chemistry* **79** (1975) 1503–1509.

[41] J. H. Baxendale, M. D. Ward and P. Wardman, *Transactions of the Faraday Society* **67** (1971) 2532–2537.

[42] J. Chevalet, F. Rouelle, L. Gierst and J. Lambert, *Journal of Electroanalytical Chemistry and Interfacial Electrochemistry* **39** (1972) 201 – 216.

[43] W. H. Koppenol, D. M. Stanbury and P. L. Bounds, *Free Radical Biology and Medicine* **49** (2010) 317 – 322.

[44] B. Blizanac, P. Ross and N. Markovic, *Electrochimica Acta* **52** (2007) 2264 – 2271.

[45] V. Andoralov, M. Tarasevich and O. Tripachev, *Russian Journal of Electrochemistry* **47** (2011) 1327–1336.

[46] P. Quaino, N. B. Luque, R. Nazmutdinov, E. Santos and W. Schmickler, *Angewandte Chemie International Edition* **51** (2012) 12997–13000.

[47] O. Antoine, Y. Bultel and R. Durand, *Journal of Electroanalytical Chemistry* **499** (2001) 85 – 94.

[48] O. Tripachev, V. Bogdanovskaya, M. Tarasevich and V. Andoralov, *Journal of Electroanalytical Chemistry* **683** (2012) 21 – 24.

[49] R. W. Zurilla, R. K. Sen and E. Yeager, *Journal of the Electrochemical Society* **125** (1978) 1103–1109.

[50] V. Viswanathan, H. A. Hansen, J. Rossmeisl and J. K. Nrskov, *ACS Catalysis* **2** (2012) 1654–1660.

[51] N. Ohta, K. Nomura and I. Yagi, *Journal of Physical Chemistry C* **116** (2012) 14390–14400.

[52] R. Adic, S. Strbac and N. Anastasijevic, *Materials Chemistry and Physics* **22** (1989) 349 – 375.

[53] C. M. Sanchez-Sanchez and A. J. Bard, *Analytical Chemistry* **81** (2009) 8094–8100.

[54] E. Yeager, *Electrochimica Acta* **29** (1984) 1527 – 1537.

[55] D. Shoup and A. Szabo, *Journal of Electroanalytical Chemistry and Interfacial Electrochemistry* **140** (1982) 237 – 245.

[56] D. Morales-Acosta, D. L. De La Fuente, L. Arriaga, G. V. Gutiérrez and F. R. Varela, *International Journal of Electrochemical Science* **6** (2011) 1835–1854.

[57] R. Weast, *Handbook of Chemistry and Physics, 55th* (CRC Press, 1974).

[58] Y. Wang, E. Laborda, A. Crossley and R. G. Compton, *Physical Chemistry Chemical Physics* **15** (2013) 3133–3136.

[59] J. C. Hoogvliet, M. Dijksma, B. Kamp and W. P. van Bennekom, *Analytical Chemistry* **72** (2000) 2016–2021, pMID: 10815959.

[60] K. R. Ward, N. S. Lawrence, R. S. Hartshorne and R. G. Compton, *Journal of Physical Chemistry C* **115** (2011) 11204–11215.

[61] D. T. Sawyer, A. Sobkowiak and J. L. Roberts, *Electrochemistry for Chemists*, volume 170 (Wiley New York, 1995).

[62] M. Chen and D. W. Goodman, *Accounts of Chemical Research* **39** (2006) 739–746.

[63] B. Hvolbæk, T. V. Janssens, B. S. Clausen, H. Falsig, C. H. Christensen and J. K. Nørskov, *Nano Today* **2** (2007) 14–18.

[64] Y. Chen, A. W. Hassel and A. Erbe, *Electrocatalysis* **2** (2011) 106–113.

[65] J. Hernandez, J. Solla-Gullon and E. Herrero, *Journal of Electroanalytical Chemistry* **574** (2004) 185–196.

[66] N. R. Jana, L. Gearheart and C. J. Murphy, *Langmuir* **17** (2001) 6782–6786.

[67] N. R. Jana, L. Gearheart and C. J. Murphy, *Journal of Physical Chemistry B* **105** (2001) 4065–4067.

[68] C. J. Murphy and N. R. Jana, *Advanced Materials* **14** (2002) 80.

[69] T. K. Sau and C. J. Murphy, *Journal of the American Chemical Society* **126** (2004) 8648–8649.

[70] M. Oyama, *Analytical sciences* **26** (2010) 1–12.

[71] Y. Cui, C. Yang, W. Zeng, M. Oyama, W. Pu and J. Zhang, *Analytical Sciences* **23** (2007) 1421–1425.

[72] L. M. Fischer, M. Tenje, A. R. Heiskanen, N. Masuda, J. Castillo, A. Bentien, J. Émneus, M. H. Jakobsen and A. Boisen, *Microelectronic Engineering* **86** (2009) 1282–1285.

[73] R. Adžić, A. Tripković and N. Marković, *Journal of Electroanalytical Chemistry* **114** (1980) 37–51.

[74] H. Angerstein-Kozlowska, B. Conway, A. Hamelin and L. Stoicoviciu, *Journal of Electroanalytical Chemistry* **228** (1987) 429–453.

[75] M. A. Schneeweiss, D. M. Kolb, D. Liu and D. Mandler, *Canadian Journal of Chemistry* **75** (1997) 1703–1709.

[76] D. Kolb, *Electrochimica Acta* **45** (2000) 2387–2402.

[77] X. Liu, M. Atwater, J. Wang and Q. Huo, *Colloids and Surfaces B: Biointerfaces* **58** (2007) 3–7.

[78] V. Amendola and M. Meneghetti, *Journal of Physical Chemistry C* **113** (2009) 4277–4285.

[79] A. Kolics, A. E. Thomas and A. Wieckowski, *Journal of the Chemical Society, Faraday Transactions* **92** (1996) 3727–3736.

[80] M. A. Diaz, G. H. Kelsall and N. J. Welham, *Journal of Electroanalytical Chemistry* **361** (1993) 25–38.

[81] J. Divišek and B. Kastening, *Journal of Electroanalytical Chemistry* **65** (1975) 603 – 621.

[82] B. Hwang, R. Santhanam and Y. Chang, *Electroanalysis* **14** (2002) 363–367.

[83] M. E. Hyde, R. M. Jacobs and R. G. Compton, *Journal of Physical Chemistry B* **108** (2004) 6381–6390.

[84] P. Delahay, M. Pourbaix and P. Van Rysselberghe, *Journal of the Electrochemical Society* **98** (1951) 57–64.

[85] D. Velayutham and M. Noel, *Electrochimica Acta* **36** (1991) 2031–2035.

[86] R. Guidelli, R. G. Compton, J. M. Feliu, E. Gileadi, J. Lipkowski, W. Schmickler and S. Trasatti, *Pure and Applied Chemistry* **86** (2014) 245–258.

[87] R. Guidelli, R. G. Compton, J. M. Feliu, E. Gileadi, J. Lipkowski, W. Schmickler and S. Trasatti, *Pure and Applied Chemistry* **86** (2014) 259–262.

[88] M. Brust, M. Walker, D. Bethell, D. J. Schiffrin and R. Whyman, *Journal of the Chemical Society, Chemical Communications* 801–802.

[89] P. Zhang and T. Sham, *Physical Review Letters* **90** (2003) 245502.

[90] J. M. Thomas and M. J. Tricker, *Journal of the Chemical Society, Faraday Transactions 2* **71** (1975) 329–336.

[91] P. W. Wang and L. Zhang, *Journal of non-crystalline solids* **194** (1996) 129–134.

[92] M. Alvarez-Rizatti and K. Jttner, *Journal of Electroanalytical Chemistry and Interfacial Electrochemistry* **144** (1983) 351 – 363.

[93] O. Oviedo, M. Mariscal and E. Leiva, *Electrochimica Acta* **55** (2010) 8244–8251.

[94] F. W. Campbell, Y.-G. Zhou and R. G. Compton, *New Journal of Chemistry* **34** (2010) 187–189.

[95] F. W. Campbell and R. G. Compton, *International Journal of Electrochemical Science* **5** (2010) 407–413.

[96] Y. Zhou, N. V. Rees and R. G. Compton, *ChemPhysChem* **511** (2011) 183–186.

[97] O. Pecina and W. Schmickler, *Chemical Physics* **228** (1998) 265–277.

[98] W. Sheng, H. A. Gasteiger and Y. Shao-Horn, *Journal of the Electrochemical Society* **157** (2010) B1529–B1536.

[99] R. Michalsky, Y.-J. Zhang and A. A. Peterson, *ACS Catalysis* **4** (2014) 1274–1278.

[100] W. Sheng, M. Myint, J. G. Chen and Y. Yan, *Energy & Environmental Science* **6** (2013) 1509–1512.

[101] P. Millet, N. Mbemba, S. Grigoriev, V. Fateev, A. Aukauloo and C. Etiévant, *International Journal of Hydrogen Energy* **36** (2011) 4134–4142.

[102] C. Galeano, J. C. Meier, V. Peinecke, H. Bongard, I. Katsounaros, A. A. Topalov, A. Lu, K. J. J. Mayrhofer and F. Schüth, *Journal of the American Chemical Society* **134** (2012) 20457–20465.

[103] B. K. Jena and C. R. Raj, *Langmuir* **23** (2007) 4064–4070.

[104] B. Wang, *Journal of Power Sources* **152** (2005) 1–15.

[105] C. C. M. Neumann, C. Batchelor-McAuley, K. Tschulik, H. S. Toh, P. Shumbula, J. Pillay, R. Tshikhudo and R. G. Compton, *ChemElectroChem* **1** (2014) 87–89.

[106] M. O. Finot, G. D. Braybrook and M. T. McDermott, *Journal of Electroanalytical Chemistry* **466** (1999) 234–241.

[107] A. Kolics, A. E. Thomas and A. Wieckowski, *Journal of the Chemical Society, Faraday Transactions* **92** (1996) 3727–3736.

[108] L. S. Ly, C. Batchelor-McAuley, K. Tschulik, E. Kätelhön and R. G. Compton, *Journal of Physical Chemistry C* .

[109] G. Brug, M. Sluyters-Rehbach, J. Sluyters and A. Hemelin, *Journal of Electroanalytical Chemistry and Interfacial Electrochemistry* **181** (1984) 245–266.

[110] J. M. Kahk, N. V. Rees, J. Pillay, R. Tshikhudo, S. Vilakazi and R. G. Compton, *Nano Today* **7** (2012) 174–179.

[111] B. E. Hayden, *Accounts of Chemical Research* **46** (2013) 1858–1866.

[112] A. S. Bandarenka and M. T. M. Koper, *Journal of Catalysis* **308** (2013) 11–24.

Conclusions

Nanoeffects arising from the different behaviour between nanomaterials and bulk materials was of particular focus in the preceding chapters. Rigorous studies were carried out to investigate the electrochemical behaviour of gold nanoparticles in different systems. In particular, it was sought to develop rigorous approaches to the identification of changed electron transfer kinetics. The followings have been achieved:

- Electrochemical characterization method: A fast, simple and effective approach was successfully developed to quantify the surface coverage of gold nanoparticle modified glassy carbon electrodes. Underpotential deposition of lead was employed to determine the surface area of the gold nanoparticles while the amount of gold deposited on the glassy carbon electrode was quantified from anodic stripping of gold in 0.1 M hydrochloric acid. Based on these results, the average size and number of gold nanoparticles was calculated. The morphology of the nanoparticle surface was also analyzed from the "fingerprint" in lead deposition/stripping experiments. The results were in

satisfactory agreement with those obtained *via* scanning electron microscopy (SEM). This methodology underpins the approaches taken in the rest of the thesis.

- Identification of "authentic" electrocatalysis: An electrochemical approach consisting of comparison between simulation and experimental results was developed for the detection of nanoeffects. The electrochemical behaviour for gold nanoparticle modified glassy carbon electrodes was modelled considering different electron transfer kinetics on gold nanoparticles and the supporting substrate. This enabled the evaluation of kinetic changes of electrode processes associated with the use of nanosized materials and therefore the investigation of possible electrocatalytic nanoeffects. In the electro-oxidation of nitrite, any electrocatalytic nanoeffect was discounted because there was no kinetic changes found between gold nanoparticles and a macro gold electrode. However, the authentic enhancement of the electron transfer kinetics of the electrooxidation of L-ascorbate by nano-gold was confirmed.

- Quantification of electron transfer kinetics for the oxygen reduction reaction on different sizes of gold nanoparticles: Based on the findings for electro-oxidation of nitrite and L-ascorbic acid, the validated strategy was further developed to quantify the electron transfer kinetics of oxygen reduction reaction (ORR) for different sizes of gold nanoparticles in 0.5 M sulphuric acid. The results indicated that similar electrochemical behaviour was observed between macro

gold materials and gold nanoparticles of sizes from 5 nm to 40 nm. However, a significant enhancement of electron transfer kinetics was achieved for ORR on 5 nm citrate capped gold nanoparticles with Pb(II) in the solution. For the studies of the ORR and the hydrogen evolution reaction (HER) carried out on ultra-small citrate capped gold nanoparticles (2nm), a strong negative effect was obtained.

In conclusion, a joint computational and experimental approach was successfully employed in this thesis to rigorously investigate electrocatalytic nanoeffects shown by gold nanoparticles. Overall the work reported in this thesis has identified cases of authentic nanoelectrocatalysis, both positive and negative. The methodology developed has generic value.